

Stall Cell Characteristics

An experimental investigation of the airfoil influence

Francis De Voogt

Technische Universiteit Delft

Stall Cell Characteristics

An experimental investigation of the airfoil influence

by

F. De Voogt

in partial fulfillment of the requirements for the degree of

Master of Science
in Aerospace Engineering

at the Delft University of Technology,

Supervisors: Prof. B. Ganapathisubramani University of Southampton
Prof. B. van Oudheusden TU Delft

Preface

This report presents the analysis of experimental wind tunnel experiments performed on a stalling NACA 0012 wing. This work is the culmination of nine months of research into the subject of stall cells. When I arrived in Southampton I had three papers to read and no clue what I was going to do for nine months. When the time came to get started with the actual testing, I had to learn experimental testing on the go. Finally after all the data was acquired I was left with a haystack and the looking for the needle could start. Every inch of the path I have taken brought me new challenges. I have enjoyed overcoming each and every one of them to reach this final destination.

This work would not have been possible without the guidance of Bharathram Ganapathisubramani. Bharath was always ready to offer his knowledge and experience to help me forward.

Furthermore I would like to thank Bas van Oudheusden for supporting my decision to investigate stall cells at the University of Southampton and guiding me through the process of combining the expectations of two universities.

Next I would like to thank all the people abroad and at home. Friends and colleagues from all over the world who have supported me and have shared wonderful times with me.

Lastly I would like to thank my parents, who have always had trust in my capabilities and encouraged me to follow my dreams.

Contents

Preface	iii
1 Introduction	1
2 Review on Stall Cell Investigations	3
2.1 Two Dimensional Stall	3
2.2 Stall Cell Characteristics	7
2.2.1 Stall Cell Requirements	7
2.2.2 Stall Cell Mechanisms	9
2.2.3 Stall Cell Behaviour	11
2.2.4 Stall Cell Unknowns	14
2.3 Experimental Research Methods	15
2.3.1 Oil Flow Visualisation	16
2.3.2 Tufts	16
2.3.3 Pressure Taps	17
2.3.4 Particle Image Velocimetry	17
2.3.5 Force Gauge	19
2.4 Computational Research	19
2.5 Summary of Stall Cell Investigations	20
3 Methodology and Experimental Setup	23
3.1 Methodology	23
3.1.1 Research Objective	23
3.1.2 Research Strategy	24
3.2 Experimental Setup	25
3.2.1 Wind Tunnel	25
3.2.2 Wing	25
3.2.3 Hot Wire Anemometry	26
3.2.4 Tufts	27
3.2.5 Force Balance	27
3.2.6 Stereoscopic Particle Image Velocimetry	27
3.2.7 Surface Oil Flow Visualisation	29
4 Data Processing and Corrections	31
4.1 Blockage Correction	31
4.2 Hot Wire Anemometry	31
4.3 Force Measurements	32
4.3.1 Hysteresis Correction	33
4.3.2 Pitching Moment Correction	33
4.3.3 Flap Misalignment Correction	35
4.3.4 Force Measurement Uncertainty	38
4.4 Tufts	39
4.5 Stereoscopic Particle Image Velocimetry	40
4.5.1 Conventional Vortex Detection	41
4.5.2 Vortex Identification By Correlation	44
4.5.3 Optimisation Validation	47

5	Results	51
5.1	Identification of Airfoil Shape Influence on Stall Cell Formation	51
5.1.1	Full Wing Tufts	51
5.1.2	Wind Tunnel Turbulence Intensity	58
5.1.3	Preliminary Conclusions	61
5.2	Single Stall Cell Investigation	62
5.2.1	Single Stall Cell Tufts	62
5.2.2	Force Measurements	66
5.2.3	Stereoscopic Particle Image Velocimetry	73
6	Conclusions and Recommendations	81
6.1	Conclusions	81
6.2	Recommendations	82
A	Conversion Tables	83
B	Surface Oil Flow Visualisation	85
	Bibliography	87

Nomenclature

Acronym	Description
<i>2D3C</i>	2 Dimensional 3 Component
<i>AR</i>	Aspect Ratio
<i>CFD</i>	Computational Fluid Dynamics
<i>(D)DES</i>	(Delayed) Detached Eddy Simulation
<i>DNS</i>	Direct Numerical Simulation
<i>FOV</i>	Field Of View
<i>HWA</i>	Hot Wire Anemometry
<i>LE</i>	Leading Edge
<i>LES</i>	Large Eddy Simulation
<i>LSB</i>	Laminar Separation Bubble
<i>NS</i>	Navier Stokes
<i>(S)OFV</i>	(Surface) Oil Flow Visualization
<i>(S)PIV</i>	(Stereoscopic) Particle Image Velocimetry
<i>(U)RANS</i>	(Unsteady) Reynolds Averaged Navier Stokes
<i>SA</i>	Spalart Allmaras
<i>SC</i>	Stall Cell
<i>TE</i>	Trailing Edge
<i>TI</i>	Turbulence Intensity
<i>TM</i>	Turbulence Model
<i>UV</i>	Ultra Violet

Symbol	Description	Unit
a	Overheat Ratio	–
c	Chord	m
C_D	Drag Coefficient	–
C_L	Lift Coefficient	–
C_M	Moment Coefficient	–
C_P	Pressure Coefficient	–
E	Electrical Potential	V
L	Lift	N
M	Pitching Moment	Nm
Re	Reynolds Number	–
T_w	Wire Working Temperature	C°
T_0	Fluid Temperature	C°
R_w	Hot Wire Resistance	Ω
R_0	Cold Wire Resistance	Ω
u	Velocity	$\frac{m}{s}$
U_∞	Freestream Velocity	$\frac{m}{s}$
α_0	Temperature Coefficient of Resistance	$\frac{1}{C^\circ}$
α	Angle of Attack	$^\circ$
β	Flap Angle	$^\circ$
δ	Flat Plate Turbulent Boundary Layer Thickness	m
θ	Wall Normal Angle	$^\circ$
ρ	Density	$\frac{kg}{m^3}$



Introduction

Aerodynamic applications optimise the design for the nominal operational conditions. The constraints for these optimisations are dictated by external influences or off-nominal performance requirements. Airplanes at high lift conditions must maintain a margin of angle of attack to prevent detrimental stall consequences in case of an upwash caused by a vertical gust. Small drones do not have similar flight envelopes as airplanes and are required to be optimised over a wide range of flight conditions. These drones are mostly designed with fixed pitch propellers and limited battery life, extending the duration of flight requires efficient propulsion over a range of throttle settings. At high throttle with low freestream velocity, the propeller rotational velocity increases relative to the inflow velocity and thereby increases the effective angle of attack. If stall is to be avoided in these situations to improve safety or efficiency this often requires the final design to be tested in wind tunnels. At the moment stall is not understood well enough to predict the behaviour at an early stage in the design and thereby causes the need for iterative design processes. A better understanding of the stall behaviour at low Reynolds numbers could improve first order estimates in design process and speed up the initial design in addition to creating improved designs.

One of the first notable research efforts into stall was performed by McCullough and Gault (1951). They investigated stall for a variety of airfoils, it was found that different airfoil shapes exhibit different stall behaviour. This research resulted in the classification of three types of stall: thin airfoil stall, leading edge stall and trailing edge stall. Stall type identification by means of these three categories is still important to this day. All three of these categories are deemed to be two dimensional phenomena, i.e. with no variation along the span of the wing. Moss and Murdin (1968) found that it is possible to have three dimensional stall effects. These three dimensional stall features have been investigated ever since and are referred to as stall cells.

Stall cells have been found to be characteristic for wings that exhibit trailing edge stall in a moderate Reynolds number range. This implies that the majority of aerodynamic applications with wings are subject to the formation of stall cells. Therefore it is crucial to achieve a good understanding of stall cells. Barlow et al. (1999) investigated the characteristic length scale and Manolesos et al. (2014) focused on identifying the characteristic vortex topology of stall cells. More recently Dell'Orso and Amitay (2018) used surface oil flow visualisation to identify different flow phases over a wide angle of attack and Reynolds number range. These flow phases included attached flow, different stall cell configurations and multiple phases in between attached and separated flow. Arranging these flow phases in an angle of attack and Reynolds number diagram allowed for the identification of the requirements for stall cell formation. From previous research the best practice for investigating stall cells can be determined. The first step is using a wing with trailing edge stall. The next step is to vary both the angle of attack and Reynolds number to obtain the required combination of these two parameters for stall cell formation. However one of the biggest problems is that the published results do not allow for a direct comparison. Results that have been published are in different angle of attack or Reynolds number ranges, and use different airfoils. It is thus necessary to identify the influence of the airfoil shape in order to allow for comparisons of previously published research.

In this report the problem of different stall cell requirements for different airfoil shapes will be addressed by using a NACA 0012 wing with a movable flap. The NACA 0012 profile can be compared to a NACA 0015 profile

used by Dell'Orso and Amitay (2018) to obtain a preliminary estimate of the influence of the airfoil thickness on the stall cell formation criteria. Additionally moving the flap angle will be considered equivalent to changing the camber of the airfoil. This then allows to obtain experimental results for a constant airfoil thickness and varying camber. This methodology results the investigation of the airfoil influence by using the thickness and camber as the defining parameters. Which leads to the following research objective.

The research objective is to contribute to the understanding of the requirements for the formation of stall cells by investigating the airfoil influence on the minimum required angle of attack and Reynolds number to form stall cells.

In this report multiple flow phase diagrams will be shown, with a focus on stall cell formation criteria. This data will serve to compare the influence of the airfoil on the changing requirements for stall cell formation. The obtained data will show how the different stall cell requirements for different airfoils in published research articles can be explained. These varying results cannot simply be explained by the thickness and the camber of an airfoil, it will be shown how two different Reynolds number regimes lead to different results for the same airfoil. Additionally the importance of the lift coefficient in predicting stall cell formation is indicated. Finally some results regarding the stall cell behaviour are discussed.

The report starts with a literature review in chapter 2, in chapter 3 the methodology of the experimental investigation and the relevant setup are described. The data processing techniques and the corrections that are applied to the experimental data are discussed in chapter 4. This is followed by chapter 5 in which the results are presented and related to the research objective and previous literature. Finally in chapter 6 the conclusions of the research and recommendations for future work are formulated.

2

Review on Stall Cell Investigations

Conceptual designs of aerodynamic applications often require several iterations. Each iteration is required to be fast and accurate. With a low level of detail fast results can be obtained through potential flow methods, such as still often used in wind turbine design, such as mentioned by Bartl et al. (2018). However achieving accurate results with a low level of detail can not be realised. One of the biggest shortcomings is the lack of potential flow to capture viscosity dominated features such as stall.

2.1. Two Dimensional Stall

The viscosity of air creates a boundary layer when a flow encounters an object. At the surface the flow viscosity slows down the flow to a stand still. When moving away from the surface the momentum of the flow dominates and the flow becomes inviscid. The boundary layer is defined as the flow between the surface and the inviscid flow, shown by the dotted line in fig. 2.1. The influence of the viscosity is strongest near the the surface and gradually decreases when moving away from the surface. This causes the velocity gradient to be largest near the surface in wall normal direction and gradually decreases towards zero at the edge of the boundary layer.

When an airflow encounters an object it is forced to move around this object. The curvature of the flow causes changing pressure along the flow direction. The change in pressure along the flow is indicated by the pressure gradient. When the pressure is increasing in the flow direction this is called an adverse pressure gradient. In the boundary layer the momentum of the flow is low. An adverse pressure gradient can affect the boundary layer, thereby reducing the wall normal velocity gradient near the wall. When the wall normal velocity gradient becomes negative, there is an area of reversed flow near the surface. This area of flow reversal indicates the separation of the laminar boundary layer. It is possible that the separation induces the formation of a turbulent boundary layer which reattaches further downstream. The area in between the initial separation of the laminar boundary layer and the reattachment of the turbulent boundary layer is the Laminar Separation Bubble (LSB), shown in fig. 2.1.

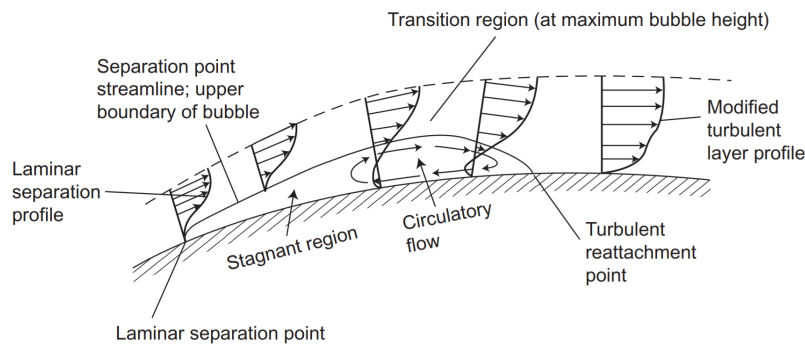


Figure 2.1: Formation of a laminar separation bubble, figure from Houghton et al. (2013)

The turbulent boundary layer will have a higher velocity gradient near the surface compared to the initial laminar boundary layer. This makes it less prone to separation. However all airfoils still have a limit beyond which the flow separates from the airfoil. This limit is often expressed in terms of angle of attack. When increasing the angle of attack of an airfoil the pressure difference between the minimum pressure near the leading edge and the freestream pressure near the trailing edge increases. Therefore a larger pressure recovery takes place over a short distance, giving rise to a higher adverse pressure gradient. Every airfoil operates on the same principle to generate lift and thus has an adverse pressure gradient. However the behaviour of the boundary layer and LSB is different for different types of airfoils. The stall behaviour of different airfoils has been divided into three different types of stall by McCullough and Gault (1951). To this day the same classification is still used.

The LSB is usually caused by a strong adverse pressure gradient, this is encountered right after the minimum pressure peak near the leading edge. When the angle of attack of an airfoil increases further, the minimum pressure peak becomes sharper and moves closer to the leading edge. For airfoils with a small thickness the LSB will be near the leading edge at small angles of attack, this is shown by state A in fig. 2.2. When the angle of attack is increased further, the LSB grows due to the reattachment point moving closer towards the trailing edge. When the LSB spans the entire chord, maximum lift is obtained such as shown by state C. Increasing the angle of attack any further will cause the LSB to burst and create a separated flow region over the entire chord length on the suction side. This type of stall is characteristic for airfoils with a small thickness which is below approximately 9% of the chord length, therefore it is called thin airfoil stall.

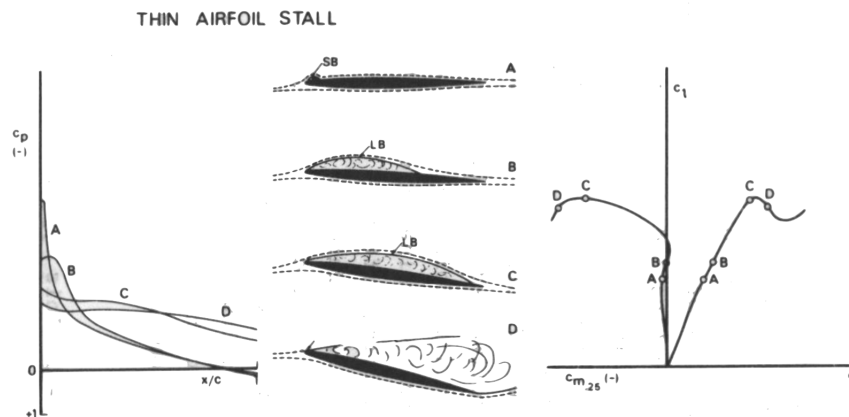


Figure 2.2: Thin airfoil stall [43]

Airfoils which are slightly thicker start out similar at lower angles of attack. They also form a LSB, however for slightly thicker airfoils the LSB starts further along the chord such as shown by state B in fig. 2.3. When the angle of attack is increased, the LSB progressively moves closer to the leading edge while keeping its size nearly constant. This is shown in state C. When the LSB has reached the leading edge any further increase in the angle of attack can yield a curvature which is too high for the flow to follow. With the turbulent boundary layer failing to reattach as a consequence. This will cause the flow to separate over the entire chord length. As stall initiates near the leading edge, this type of stall is called leading edge stall. Leading edge stall causes a large loss of lift and occurs very sudden. This illustrates how small differences in airfoil geometry can cause large differences in flow behaviour. Leading edge stall is characteristic for airfoils with a moderate thickness of approximately 9 to 15% of the chord length.

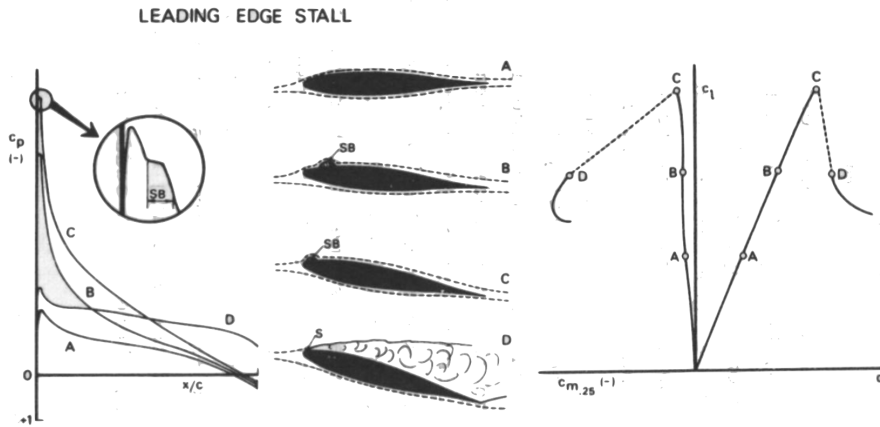


Figure 2.3: Leading edge stall [43]

Relatively thick airfoils, with a thickness of approximately 15% of the chord length or more, exhibit different stalling behaviour. The difference follows from the more gradual curvature induced by the thickness of the airfoil near the leading edge. The gradual curvature results in a lower pressure peak and a more gradual pressure recovery over the rest of the chord. A more gradual pressure recovery in turn results in a lower adverse pressure gradient. The lower adverse pressure gradient allows for a more efficient transition from a laminar to a turbulent boundary layer, such as described by Gopalarathnam et al. (2003). After the boundary layer transition the adverse pressure gradient is still present for the remainder of the chord length. Over this length the adverse pressure gradient can reduce the wall normal velocity gradient of the boundary layer. The boundary layer thus progressively slows down towards the trailing edge. When the angle of attack is increased the adverse pressure gradient increases too. The adverse pressure gradient can be strong enough such that it induces flow reversal. The flow reversal will start at the trailing edge where the boundary layer wall normal velocity gradient is the lowest. Further increasing the angle of attack will thus move the separation point further upstream due to the increased adverse pressure gradient. As the separation starts at the trailing edge, this type of stall correspondingly is called trailing edge stall.

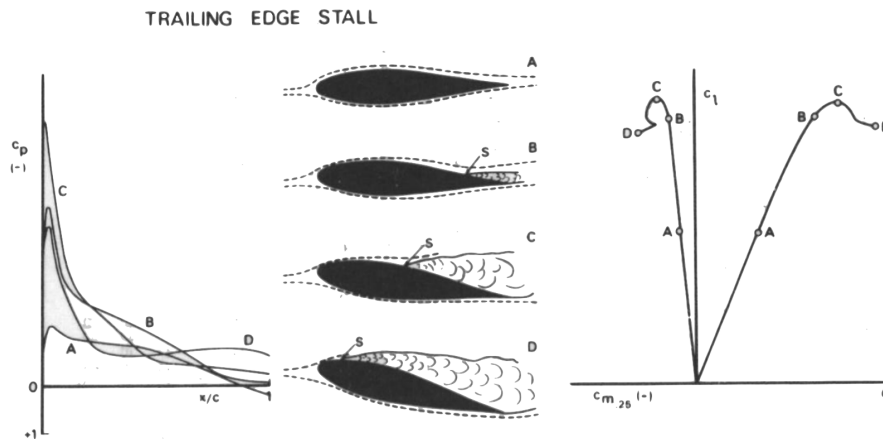


Figure 2.4: Trailing edge stall [43]

The early experiments performed by McCullough and Gault (1951) were performed by using different wings in a two dimensional configuration. This is done by using a wing with a constant cross section across the span. This wing is placed in between two walls or end plates in the wind tunnel. The walls do not introduce a streamwise or spanwise variation in the flow if the boundary layer on the wall is neglected. The pressure difference acting on the wall due to the flow inside the tunnel, compared to the outside, is supported by the

wind tunnel structure. Therefore the flow inside the test section does not experience a difference compared to a unconstrained free flow. The walls effectively provide an aerodynamic mirror image of the flow and the pressure inside the wind tunnel. With a wall on either side of the wing, the two dimensional wing can be seen as representative for an infinite wing.

The experiments performed by McCullough and Gault relied on the assumption of a 2D configuration to be representative for an infinite wing. In order to observe the stall behaviour of the different wings, the following experimental techniques were used: a force balance, tufts, pressure taps and Surface Oil Flow Visualisation (SOFV). The tufts and the pressure taps provide the first indications of stall. Tufts are small pieces of string attached to the wing surface that align with the local flow. When these tufts start to show unsteady behaviour and become oriented in the upstream direction, flow reversal is present at the wing surface. The pressure taps are tiny holes in the wing surface that allow measurement of the local static pressure. When flow reversal occurs the static pressure in the separated region near the surface stays approximately constant. This is shown clearly in fig. 2.5 where the separation point can be seen to move closer to the leading edge as the angle of attack increases. The behaviour shown in fig. 2.5 is thus indicative of trailing edge stall. The SOFV uses a liquid substance with high visibility particles which gets dragged along with the flow at the surface. The liquid substance evaporates while the wind tunnel is running which results in a pattern of particles indicative of the flow behaviour. The pattern provides a high resolution image of the surface flow behaviour and allows for the identification of the LSB and separation point. Finally the force balance measures the forces that the wing experiences. These forces can then be normalised to force coefficients using the wing span, based on the assumption that the two dimensional configuration is representative for an infinite wing. This assumption is important as the force coefficients that are obtained from a two dimensional wing are assumed to be the average value for that wing cross section regardless of the wing span. The performance coefficients resulting from two dimensional flow experiments are essential to most preliminary aerodynamic designs.

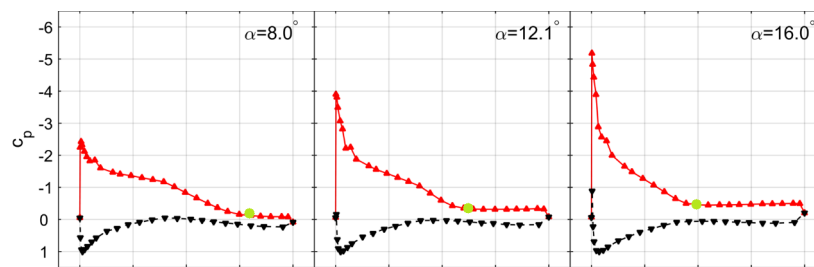


Figure 2.5: Pressure coefficient behaviour for flow separation, separation point indicated by the green dot [36]

In the report by McCullough and Gault (1951) no comments were made regarding the wing orientation. It is however mentioned that the wings have a five foot chord length and that the wind tunnel has a seven by ten foot cross section. Under the two dimensional assumption there is no difference between mounting a wing vertical or horizontal, i.e. a long or a short wing span. This means that the wing could have had an aspect ratio of 1.4 or 2.

Many years later Moss and Murdin (1968) performed experiments on a NACA 0012 wing. The wing was also used in a two dimensional configuration. Using SOFV the pattern that emerged when the wing was stalled did not correspond to the two dimensional stall behaviour such as was described by McCullough and Gault (1951). The separation line was found to be curved and terminated by two spiral nodes near the trailing edge, such as shown in fig. 2.6. The spanwise variation in flow behaviour shows that a two dimensional configuration does not always yield two dimensional flow. This is an important indication that performance coefficients obtained from a two dimensional configuration are not always representative for an infinite wing.

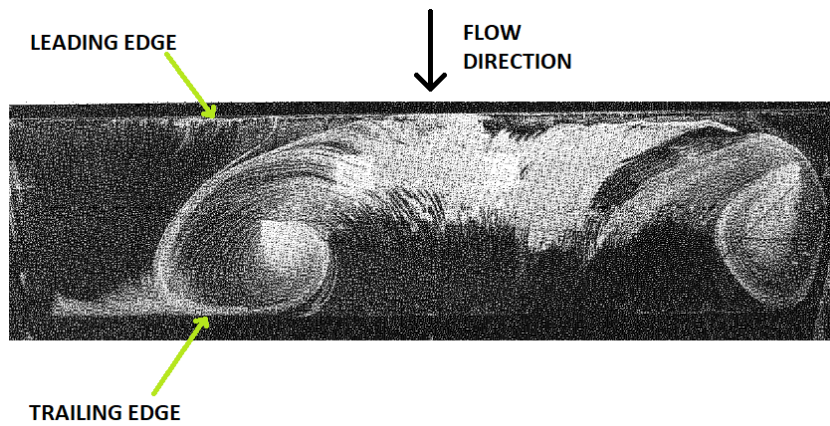


Figure 2.6: Stall cell observation with SOFV on a NACA 0012 wing by Moss and Murdin [32]

This was one of the first observations of the type of stall behaviour which later will be referred to as stall cells. Some further observations made by Moss and Murdin (1968) lead them to conclude that this behaviour is an aerodynamic feature of specific wings at specific conditions in a two dimensional configuration. This initial observation has sparked investigations over the following decades with the goal to uncover some of the characteristics of these stall cells.

2.2. Stall Cell Characteristics

The occurrence of stall cells represents three dimensional behaviour on two dimensional configurations. As stall is generally avoided and difficult to investigate, this subject has been left relatively untouched over several decades. With new experimental and computational techniques this topic has gained renewed interest from the research community. The new research brings to light more questions regarding the stall cells. In this section first the most prominent requirements for stall cells will be described. This is followed by a simplified explanation of the most plausible stall cell mechanisms. After that a summary of the known behaviour of stall cells up till now is given. Finally some of the questions surrounding stall cells are touched upon.

2.2.1. Stall Cell Requirements

The first and most important requirement for stall cells is an angle of attack which is large enough to induce stall. The formation of stall cells occurs over a range of angles of attack of approximately one or two degrees and stall cells have been reported to be present for a range of approximately five degrees, this is illustrated by published results from Yon and Katz (1998) and Dell'Orso et al. (2016). Initially there is little flow separation near the trailing edge at approximately maximum lift coefficient, possibly with recirculation regions near the endplates such as shown by Dell'Orso et al. (2016). Increasing the angle of attack beyond maximum lift will induce the three dimensional effects by creating a curved or discontinuous separation line illustrated by Oil Flow Visualization (OFV) from Dell'Orso and Amitay (2018). When the angle of attack is increased further, stall cells will form. This is shown by the sequence of OFV images on the right hand side of fig. 2.7.

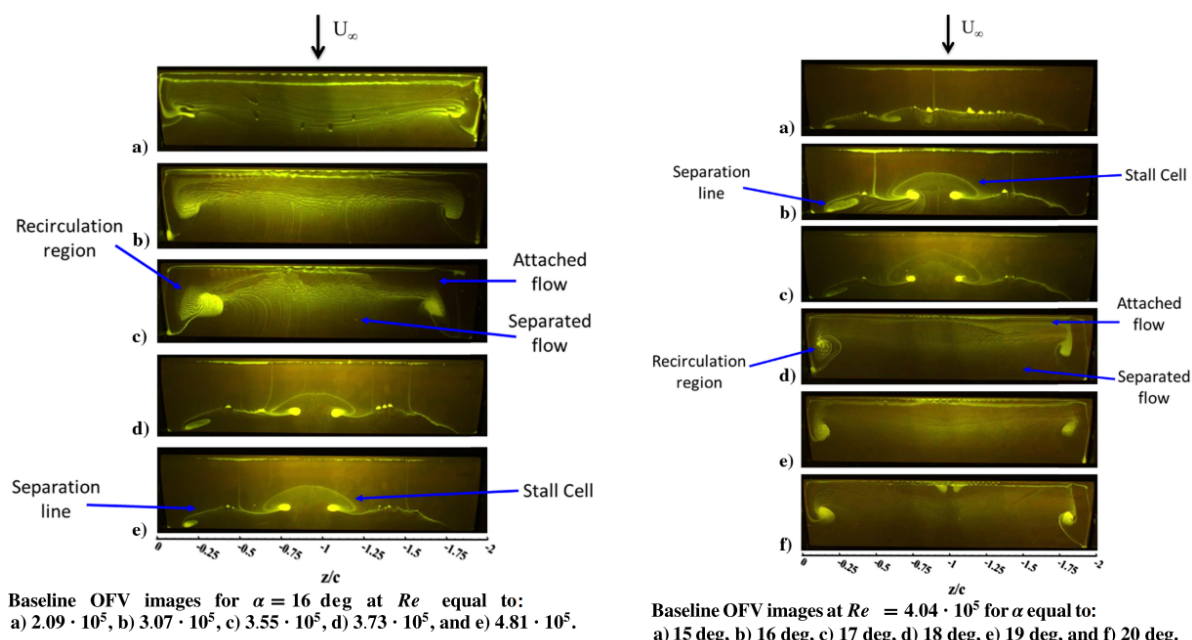


Figure 2.7: Reynolds number and angle of attack requirements for stall cells, figure from Dell'Orso et al. (2016)

A second requirement for the occurrence of stall cells is the appropriate Reynolds number. A minimum Reynolds number is required for the stall cell formation at a constant angle of attack, as is shown by the OFV images on the left hand side of fig. 2.7. From research performed by Schewe (2001) it has been shown that there is also a maximum Reynolds number beyond which the stall cells will disappear again. It is well known that the Reynolds number affects stall behaviour. Whereas usually the Reynolds number influence results in gradual changes to the performance of a wing, the creation of stall cells by varying the Reynolds number can be sudden and with detrimental effects to the performance of the wing, as discussed by Schewe (2001) and Dell'Orso and Amitay (2018).

As discussed in section 2.1 there are three general types of stall. Stall cells have been shown to be typical for wings which exhibit trailing edge stall. Furthermore it was shown by Broeren and Bragg (2001) that it is possible to obtain stall cells on wings which have a combination of trailing edge and leading edge stall. It can be noted that although stall cells have mostly been observed in a two dimensional configuration, they are also present on finite or swept wings with any form of trailing edge stall, these observations have been documented by Winkelmann and Barlow (1980), Kamenetskiy et al. (2014) and Flynn et al. (2001).

These requirements have recently been investigated by Dell'Orso and Amitay (2018). A parametric investigation mapped the influence of the Reynolds number and angle of attack on a two dimensional NACA 0015 wing (AR of 4) with trailing edge stall. The experiment used both Stereoscopic Particle Image Velocimetry (SPIV) and OFV to define multiple flow scenarios on the wing and map them in a comprehensive flow phase diagram such as shown in fig. 2.8. The figure shows how there exists a minimum Reynolds number and a minimum angle of attack. Furthermore it can be seen that the minimum Reynolds number increases as the angle of attack increases.

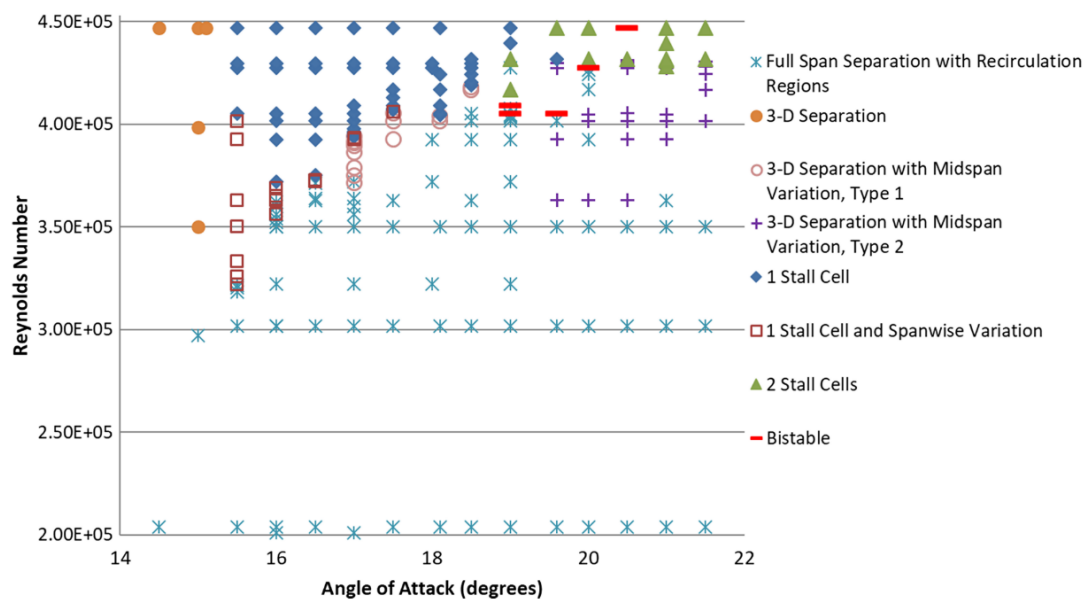


Figure 2.8: Flow phase diagram for a NACA 0015 wing, figure from Dell'Orso and Amitay (2018)

2.2.2. Stall Cell Mechanisms

Although it is known that trailing edge stall is required for the formation of stall cells, the mechanism for the creation of stall cells is far from understood. Prior to the formation of stall cells some form of flow separation is already present. This flow separation is in line with the proposed creation mechanism for stall cells by Weihs and Katz (1983). The proposed theory is based on two counter rotating vortices running parallel to the trailing edge. One of which originates from the shear layer of the separated flow. The second vortex comes from the flow which reaches the trailing edge at the pressure side of the airfoil and leaks to the suction side of the airfoil where low pressure separated flow is present. The instability of these vortices such as described by Crow (1970) then might lead to the creation of stall cells, such as shown by fig. 2.9. Some research articles, such as Yon and Katz (1998), Elimelech et al. (2012), Dell'Orso et al. (2016) and others, indicate that this is the most plausible theory for stall cell creation.

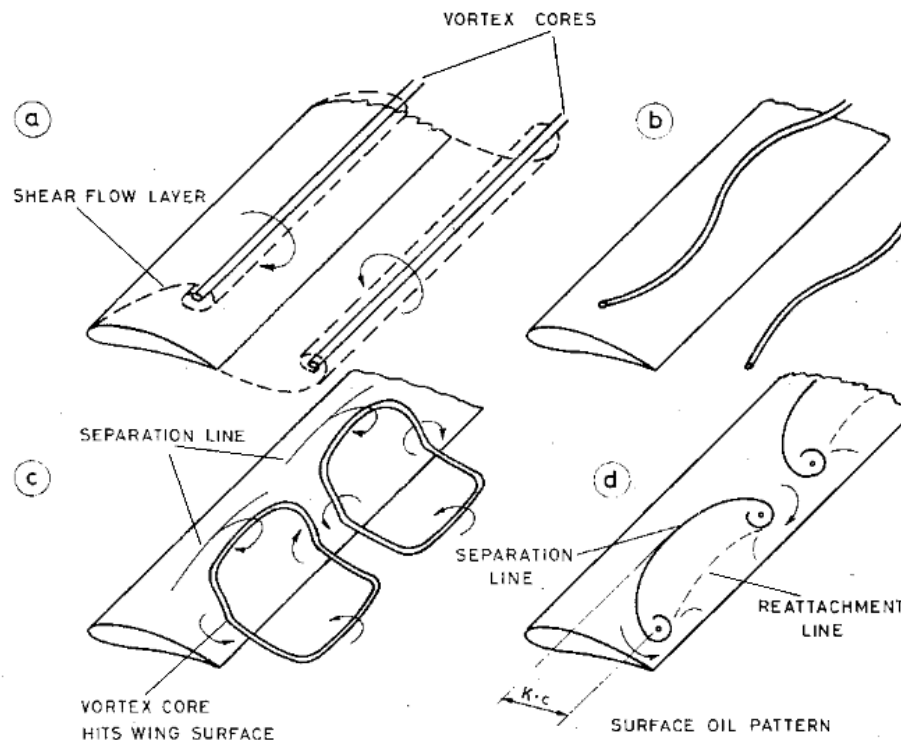


Figure 2.9: A proposed stall cell creation mechanism by Weihs and Katz (1983) based on the Crow (1970) instability, figure from Weihs and Katz (1983)

The sudden formation of stall cells makes it very difficult to investigate this theory further experimentally. Therefore most of the recent research has been focused on understanding the flow mechanisms involved in stall cells after the initial creation. Just as for the creation mechanism there have been early speculations on the flow mechanisms that maintain a stall cell. Experimental proof of some of these proposed theories has been mostly indirect and inconclusive. The most conclusive results to date have been given by Manolesos and Voutsinas (2014). In this research both experimental and computational methods have been used to quantify the flow field velocities. The results have a good correspondence and capture a complete stall cell. From these results it has been shown that three characteristic vortex types are involved in stall cells, which are shown schematically in fig. 2.10.

The first is the separation line vortex which originates from the shear layer caused by the flow reversal in the separated flow region (A in fig. 2.10). The separation line vortex core runs in the direction parallel to the trailing edge and has an orientation that induces an upwash at the leading edge.

The second vortex is the trailing edge line vortex, this vortex originates at the trailing edge where the pressure side flow meets the low pressure separated flow on suction side of the airfoil (B in fig. 2.10). From this it thus follows that this vortex core also has a direction which is along the trailing edge similar to the separation line vortex. The rotation of this vortex is opposite to the separation line vortex and induces a downwash at the leading edge.

The third vortex type is the vortex coming from the spiral nodes. Each stall cell has two spiral nodes, one at each end of the separation line and has thus also two spiral node vortices (C in fig. 2.10). Much confusion over how these vortices behave has existed in the past, but Manolesos and Voutsinas (2014) provided results that strongly indicate a specific behaviour. It was observed that these vortices rise up from the airfoil surface, perpendicular to the surface. After this they quickly bend inwards towards the centre of the stall cell and then trail downstream. These findings are in line with some of the earlier predictions by Yon and Katz (1998) that the spiral node vortices should trail downstream. These predictions were based on the orientation of the spiral node vortices. They have an opposite orientation, such that both induce an upwash near the center of the stall cell and a downwash outside the stall cell when they trail downstream. This effect has been measured by Yon

and Katz (1998). As these vortices are the most characteristic for stall cells, they will be referred to as stall cell vortices throughout the remainder of the report.

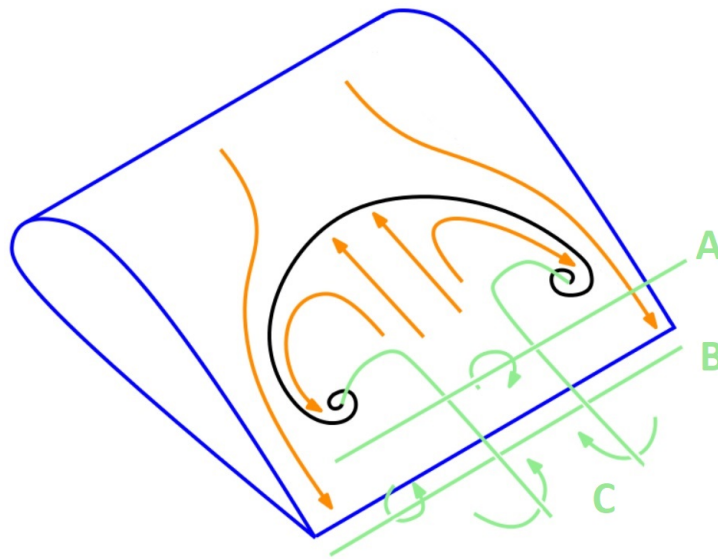


Figure 2.10: Stall cell vortices shown in green and the flow direction shown in orange

2.2.3. Stall Cell Behaviour

Gregory and O'Reilly (1970) applied boundary layer suction on the walls of the wind tunnel. Without suction it was initially found that the stall cells can be found at the mid span or split into two halves. Each half of the stall cell was attached to the wall, with the wall providing its mirror image. When suction of the wall boundary layer was applied, stall near the wall was prevented. However, this did not prevent the formation of a stall cell at the mid span location. These observations lead to the assumption that the stall cells are not a wall effect.

The most recognisable behaviour of stall cells is the amount of stall cells that are present on a wing. After Gregory and O'Reilly (1970) this was also shown by the investigation performed by Gregory et al. (1971). It has been shown that either half or full stall cells exist. Gregory et al. (1971) used a wing with removable fins. This allowed to adjust the aspect ratio that is experienced by the flow over the wing. The aspect ratio was initially 3.14 on the full span wing, this led to the formation of one big stall cell near the mid span location. Some areas of attached flow still remained besides the stall cell near the walls. When the aspect ratio was divided with fins in sections of 0.93, 1.28 and 0.93 it was found that the sections of 0.93 stalled and created half a stall cell. When the section with aspect ratio 1.28 stalled it created a full but asymmetrical stall cell. This indication for the influence of the aspect ratio was further investigated by Winkelman and Barlow (1980). With a variable aspect ratio wing it was observed that increasing the aspect ratio increases the amount of stall cells on the wing. A linear trend was observed where increasing the aspect ratio also increases the amount of stall cells on the wing. This linear trend can be refined into a linearly increasing step curve, an example of this is shown in fig. 2.11. Stall cells tend to exist as a whole or a half but no intermediate values.

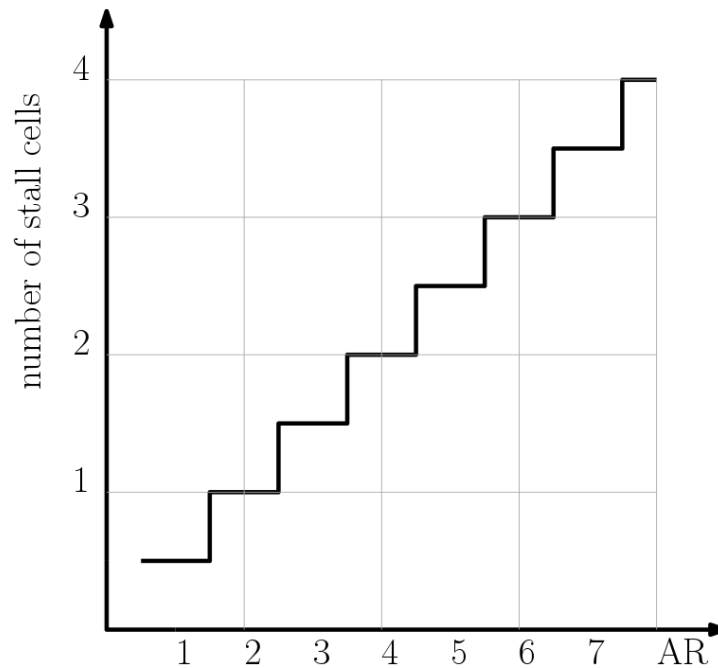


Figure 2.11: Approximate trend for stall cell formation as a function of the aspect ratio

Yon and Katz (1998) also used a variable aspect ratio wing to confirm the linear trend and show the chord related spanwise scale of stall cells. A full stall cell has an approximate width in spanwise direction of two chord lengths. This length scale is an approximation, the exact influence of the airfoil or Reynolds number is not yet understood. Yon and Katz (1998) also mentioned that increasing the aspect ratio gradually will result in the stall cells growing to a preferred width and a further increase of aspect ratio will increase the width of the attached flow region between the stall cells. An experiment by Schewe (2001) visualised this effect with surface oil flow such as shown in fig. 2.12. In this figure it can also be seen how, for the specific airfoil used, the width of the stall cells is lower than two times the chord, but still consistent for different aspect ratios and Reynolds numbers. This could be an indication that the scaling of the stall cells depends on the airfoil.

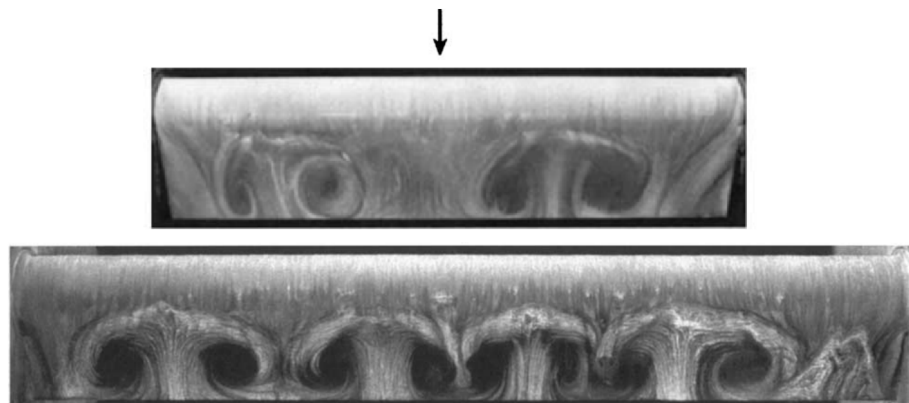
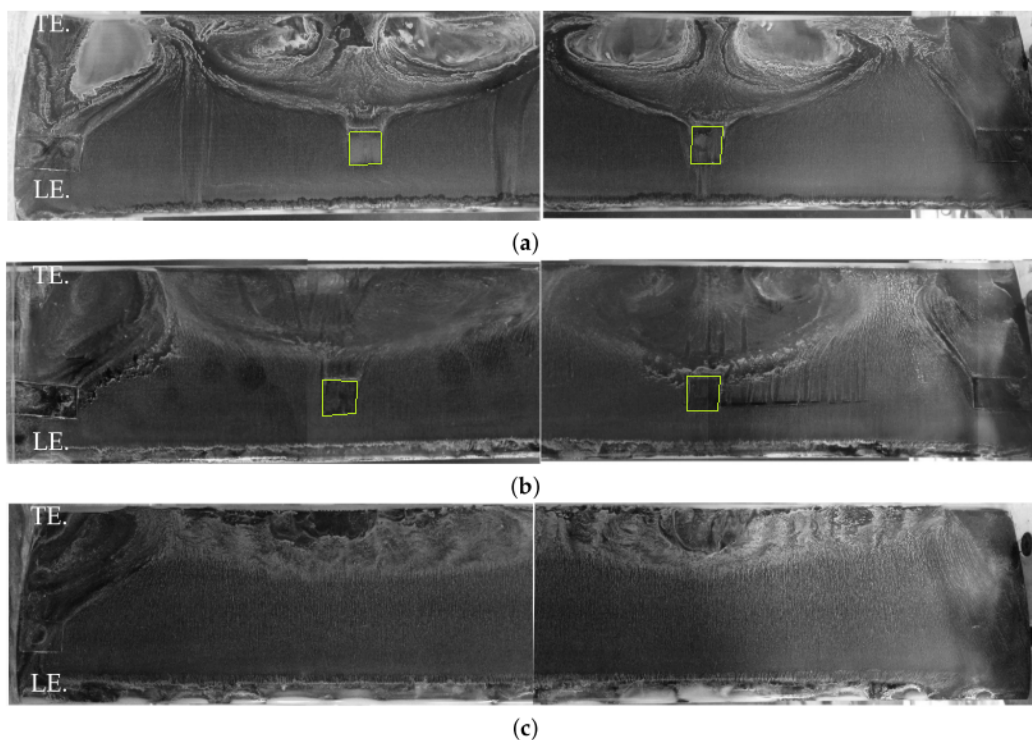


Figure 2.12: Top: aspect ratio 4 ($Re = 1.2 \cdot 10^6$), bottom: aspect ratio 6 ($Re = 0.74 \cdot 10^6$), figure from Schewe (2001)

More recent research indicates that although the aspect ratio is the driving factor in the amount of stall cells that are created, the angle of attack can also have an influence. Winkelman and Barlow (1980) already mentioned that two stall cells can merge into one stall cell when the angle of attack is progressively increased. An opposite effect was observed in the investigation of Dell'Orso et al. (2016). The influence of the angle of attack can also be found in the methods to predict the amount of stall cells on a wing presented by Weihs and Katz (1983) and

Gross et al. (2015). These methods capture the important parameters and provide approximate results. However no comprehensive validation regarding the stall cell behaviour at increasing angles of attack is present yet.

A final important observation of stall cell behaviour is the steady behaviour, or the lack of it. Some of the earlier stall cell observations, among which Gregory and O'Reilly (1970), Yon and Katz (1998) and Flynn et al. (2001), reported unsteady behaviour of the stall cells. The unsteady behaviour is described as jostling, where the stall cell moves in a seemingly random manner back and forth in spanwise direction. These observations also describe the behaviour of stall cells that randomly appear or disappear, and split or merge. Contrary to these observations stall cells have also been reported to be stable by Broeren and Bragg (2001) and Elimelech et al. (2012). It has been reasoned by Manolesos et al. (2014) and Manolesos and Voutsinas (2014) that the possible contributors to the unsteady behaviour are a high Reynolds number and a high turbulence intensity, although this has not been proven yet. Analytical work by Rodríguez and Theofilis (2010) and Rodríguez and Theofilis (2011), and experimental work by Elimelech et al. (2012) and Weihs and Katz (1983) has shown that stall cells are a consequence of three dimensional spanwise instabilities. This spanwise instability requirement is also reflected in the creation mechanism suggested by Weihs and Katz (1983), where a disturbance can cause the separation and trailing edge line vortices to deform. In order to stabilise stall cells for experimental observations they have been forced with a three dimensional disturbance in spanwise direction. This has been done by means of a plasma actuator in Esfahani et al. (2018) or a small piece of zig zag tape used by Manolesos et al. (2014) and Dell'Orso et al. (2016). This three dimensional disturbance will then create a stable stall cell downstream of the disturbance. Furthermore it has been shown that even the smallest disturbances can create this effect. A disturbance as small as a piece of tape to cover a hole can be enough to trigger the stall cells, as shown in fig. 2.13 from research performed by Sarlak et al. (2018).



The effect of disturbances on the stall cell patterns at $\alpha = 12^\circ$. Flow is passing from bottom (LE) to top (TE). (a) $Re = 160,000$ and $\alpha = 12^\circ$: screw holes covered by tape; (b) $Re = 100,000$ and $\alpha = 12^\circ$: screw holes covered by tape; (c) $Re = 100,000$ and $\alpha = 12^\circ$: screw holes covered by filler.

Figure 2.13: The influence of a piece of tape on stall cell formation, figure from Sarlak et al. (2018)

The influence of the zig zag tape on the stall cells has been investigated by Manolesos et al. (2014), Manolesos and Voutsinas (2014) and Dell'Orso et al. (2016) to confirm that no macroscopic changes to the stall cells occur due to the zig zag tape triggering. This research has shown that the zig zag tape only has a minor influence, such

as shown in fig. 2.14. The angle of attack at which stall cells initially appear has been found to be approximately one degree lower at a constant Reynolds number.

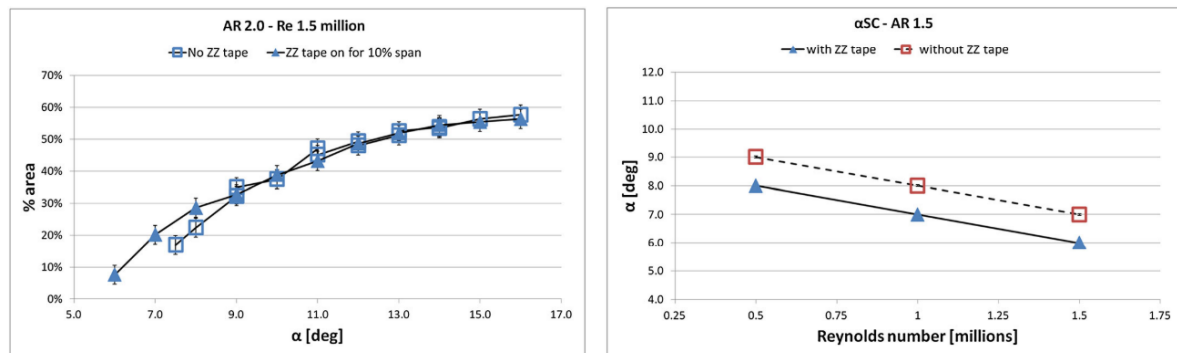


Figure 2.14: The influence of zig zag tape on the stall cells and the Reynolds number influence. Left: the relative area of the stall cell compared to the wing surface area as a function of the angle of attack. Right: the angle of attack at which stall cells first form for different Reynolds numbers, figure from Manolesos and Voutsinas (2014)

2.2.4. Stall Cell Unknowns

The ongoing research into stall cells has identified certain parameters that have an influence on stall cells such as the aspect ratio, the angle of attack and the Reynolds number. Still it is not known what the exact influence of each of these parameters is, more data is required to be able to gain insight in the combined workings of these parameters. This has been indicated by the contradicting observations regarding the Reynolds number or angle of attack influence on stall cell formation that have been reported. Traditionally an increase in the Reynolds number will delay stall to larger angles of attack for thin airfoils such as described by Pettersson and Rizzi (2008). An opposite effect has been reported by Manolesos and Voutsinas (2014), as shown on the right hand side graph of fig. 2.14. Which however is inconsistent with the research reported by Dell'Orso and Amitay (2018), shown in fig. 2.8. The Reynolds number effect as described by Manolesos and Voutsinas (2014) could still be an explanation for the observations of a detrimental stall effect on thick wing performance with increasing Reynolds number, such as described by Li et al. (2017).

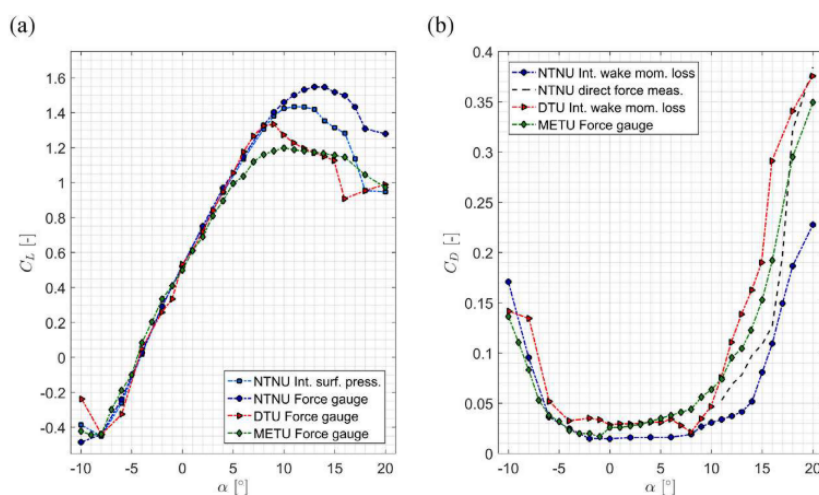
The steady or unsteady behaviour of the stall cells has been observed and reported, but has not yet been investigated. Manolesos et al. (2014) reasoned that it could be both the Reynolds number and the turbulence intensity. However, research that has spanned a large Reynolds number range performed by Dell'Orso et al. (2016) doesn't mention unsteady behaviour. This leaves the turbulence intensity to be tested as the main contributor to unsteady behavior.

Another big gap in the stall cell knowledge is the influence of the airfoil shape on stall cell formation. The research that has been performed by different researchers considers different airfoil shapes. As most of the research has a different setup or different goal, the previously performed research does not allow for a comparison. Small differences in airfoil shapes sometimes lead to big changes in characteristics. For example research performed on a NACA 0009 wing by Elimelech et al. (2012) reports stall cells at Reynolds numbers of several ten thousand, whereas observations on NACA 0012 or NACA 0015 wings require Reynolds numbers an order of magnitude larger for stall cell formation shown by Gregory and O'Reilly (1970) and Dell'Orso and Amitay (2018) respectively. The influence of camber has even less data that is suited for comparison. The shape of the airfoil can also be the determining factor in the length scale of the stall cells. Yon and Katz (1998) and Dell'Orso et al. (2016) both report two stall cells on NACA 0015 wings of AR 6 and 4 respectively, whereas fig. 2.12 shows 4 stall cells on a FX-77-W270 wing with AR 6.

In the search for understanding the mechanisms of stall cells, the consequences on the performance of the wing have been mostly neglected. Only recently the first experiments with some quantitative results have been published, with either direct or indirect measurements published by Bartl et al. (2018), Esfahani et al. (2018) and Sarlak et al. (2018). Esfahani et al. (2018) used pressure taps near the centerline of a wing to convert the static pressure into a sectional lift coefficient. The influence of the stall cell geometry on the pressure taps location is hereby not taken into account, which therefore results in merely a sectional lift coefficient which does not relate

to the full wing performance. Sarlak et al. (2018) used a wing with a force gauge and pressure taps, this allowed for a comparison of a sectional lift coefficient with the lift coefficient of the entire wing. This comparison showed how the lift polar from the sectional performance does not correspond to the average performance of the wing. In this research the lift polar from pressure integration underestimated the wing performance. As the wing performance is an average of the sectional lift coefficient over the span, it can be suspected that the pressure taps were located inside a stall cell. Which also implies that the lift performance between stall cells will outperform the average lift coefficient curve of the wing.

Bartl et al. (2018) provides a comparison of multiple tests performed on a wing with the same airfoil shape. The tests are performed at different facilities and the wings have different aspect ratios. Furthermore different methods are used for obtaining force coefficients. Wake momentum and surface pressure integration are compared to force gauge measurements. It is shown how there are large differences between the results, especially in the stalled region as shown in fig. 2.15, some of which are unlikely to be caused by different measurement methods or turbulence intensity levels. Leaving three dimensional stall effects to be the most likely contributor to the different performance observed, as a consequence of taking local measurements and using wings with a different AR. However no conclusive explanation can be given for the big differences in near stall force coefficients.



Comparison of the lift and drag coefficients of three different experimental data-sets measured at NTNU, DTU and METU at $Re = 1.0 \times 10^5$.

Figure 2.15: Experimental force coefficient results obtained for a 2D NREL S826 wing, figure from Bartl et al. (2018)

2.3. Experimental Research Methods

The characteristics described in section 2.2 have all been obtained through experimental investigation. In this section some of the relevant experimental techniques that have been used will be shortly characterised with their specific applications to and influence on stall cells.

Many observations of stall cells have already been mentioned with their corresponding implications. Most of these experiments are summarised in table 2.1 to provide an overview of the most relevant previous work that can be found in literature. The table includes the data which can be found in the respective literature, which are listed in a chronological order. The table shows how mostly different airfoils have been used with AR's ranging from 3 to 6, which indicates that most stall cell observation will have 1 to 3 stall cells on a wing at a time. The table serves to give an overview as it does not include all relevant parameters such as the angle of attack or the turbulence intensity.

Author	Airfoil	Reynolds (10^6)	Aspect Ratio	# Stall Cells
Moss & Murdin [32]	NACA 0012	1.68	3.75	1
Gregory & O'Reilly [14]	NACA 0012	2.88	3.6	1.5
Winkelmann & Barlow [45]	Clark-Y (14%)	0.385	3, 6, 9	1, 2, 3
Yon & Katz [46]	NACA 0015	0.62	4, 5.5 (± 0.5)	2, 2.5
Broeren & Bragg [5]	NACA 2414	0.3	2.8	1.5
Schewe [40]	FX-77-W270	1.2, 0.74	4, 6	2, 4
Elimelech et al. [10]	NACA 0009	0.018	2.5, 5	2, 4
Manolesos et al. [28]	NTUA t18	1 (± 0.5)	2	1
Dell'Orso et al. [9]	NACA 0015	0.36 - 0.48	4	1-2
Ragni & Ferreira [36]	NACA 64-418	1	4.8	1
Dell'Orso & Amitay [8]	NACA 0015	0.395, 0.428	4	1, 2
Sarlak et al. [39]	NREL S826	0.1, 0.16, 0.2	5	2.5
Esfahani et al. [11]	Boeing VR-7	0.5	3	2

Table 2.1: Summary of experimental stall cell observations in literature

2.3.1. Oil Flow Visualisation

Early experiments, such as performed by Moss and Murdin (1968) relied on established qualitative surface flow visualisation for stall cell identification. This can be achieved by SOFV. Proper application of SOFV can produce high resolution visual images of the surface flow by using tiny particles with high visibility.

Careful interpretation of the oil flow images is as important as applying the oil and acquiring the images. The use of SOFV usually serves to identify the existence of stall cells and to determine the geometry with a high accuracy in a steady state. The geometrical data then serves to position quantitative measurements at locations of interest.

There are drawbacks too. The method relies on experience to apply the oil in a correct manner and to make the right interpretations. Additionally, with the possible unsteady behaviour of stall cells this can be problematic as the oil cannot settle and dry in a fixed position anymore. The resulting image will be a smudge that does not represent any of the aerodynamic flow structures.

2.3.2. Tufts

To overcome the problem of unsteady flow behaviour, a dynamic measuring method is needed. When the focus is still on qualitative flow visualisation, then the easiest solution is using tufts. These are small pieces of yarn or thread that are fixed with one end to the surface of the tested object.

In the research of stall cells tufts have been used in a similar fashion as SOFV to identify the flow structures near the surface of the wing. The added ability of identifying unsteadiness comes at the cost of losing the spatial resolution of SOFV. Tufts are mostly a qualitative measurement method, but have been used to obtain some quantitative data regarding the separation line such as shown in fig. 2.16.

The main drawback of using tufts for flow visualisation is the risk of the tufts disturbing the flow and thereby altering the flow structures. As mentioned earlier stall cell formation can be triggered by small disturbances. It remains to be investigated to what extent the tufts influence the formation of stall cells compared to a undisturbed configuration.

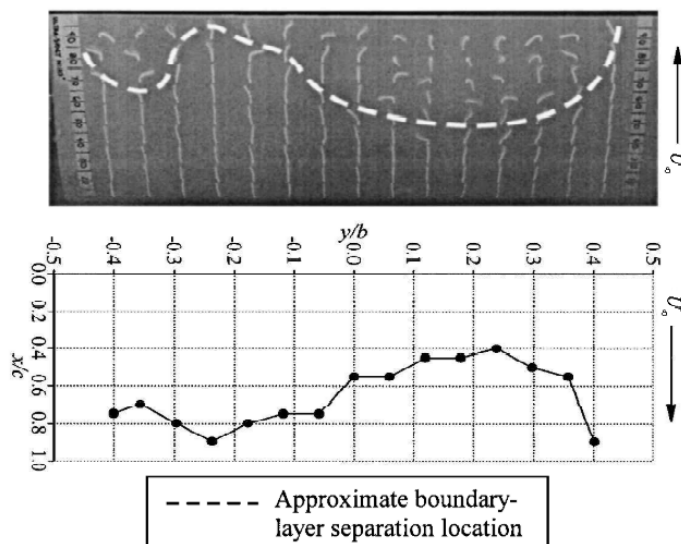


Figure 2.16: Tuft flow visualisation with separation line information obtained from tufts [5]

2.3.3. Pressure Taps

The measurement techniques mentioned above focus on visualising the flow. Both SOFV and tufts only have a very limited capability of providing quantitative data. A common method for obtaining quantitative flow information is using pressure taps.

For the installation of the pressure taps it is common practice to have sequential holes along the chord inclined at an angle with respect to the local flow direction, to avoid the disturbance of an upstream orifice influencing the downstream pressure measurements. As stall cells are a three dimensional flow structure, they have varying pressure distributions in spanwise direction. The pressure tap positioning and inclination angle thus have to be taken into account when observing stall cells.

Practically it is preferred to have short tubes between the taps and the transducer such that it is possible to capture the fluctuations in the pressure. When this is not possible, the transducer can be placed further away, taking into account that pressure fluctuations will be underestimated. The pressure transducer is then connected to a data acquisition system that samples the analogue pressure transducer output to obtain a discrete digital output that can be stored and used for post processing.

2.3.4. Particle Image Velocimetry

When quantitative data about the flow velocity is required mostly Hot Wire Anemometry (HWA) or Particle Image Velocimetry (PIV) are used. Both have been used and described extensively in literature. HWA is known for good accuracy and high sampling frequencies. The drawback is that HWA is limited to measuring velocity magnitudes perpendicular to the probe hot wire. HWA has a wire so small in length (<5 mm) that the measurement can be deemed a point measurement relative to objects two orders of magnitude larger. PIV allows to obtain a velocity field with a similar resolution. Additionally the use of Stereoscopic PIV (SPIV) results in a 2D velocity field for which the three Cartesian velocity components are known.

When dealing with three dimensional unsteady flows, the third velocity component can provide necessary information to accurately portray the flow behaviour. Stereoscopic PIV (SPIV) has the preference of the research community when considering stall cells. SPIV can be performed with either parallel cameras or cameras with an angle in between them, both configurations are shown in fig. 2.17.

The parallel camera setup also known as the translation setup has the advantage of being simplistic, but comes at the cost of a limited camera separation. When the separation of the cameras is too far apart, the combined Field Of View (FOV) has less overlap of the two separate FOVs. Which implies that the overlap area is at the edge of the single camera FOVs. Thereby making it more prone to having distortion from the camera lenses or camera vignetting. The problem with small camera separation is that it reduces the capability to capture the third velocity component which is the out of plane (laser sheet) component.

This problem is solved by the Scheimpflug configuration in which the lens is tilted with respect to the camera. The Scheimpflug configuration aims to have the image plane, lens plane and the object plane all intersect at a single point. This allows for a large camera separation without the distortion, thereby capturing the out of plane component better.

A final benefit of the Scheimpflug configuration is that it allows for two different configurations, the first is such as described above and shown in fig. 2.17 with two cameras on one side of the laser sheet. A second configuration is very similar but has one camera on each side of the laser sheet with the object plane still being aligned with the laser sheet.

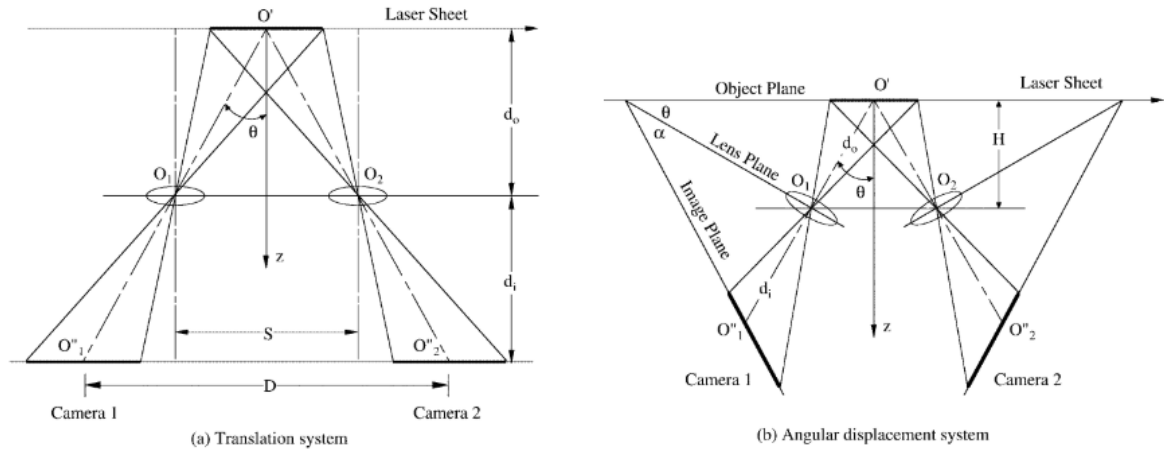


Figure 2.17: SPIV setup: a) parallel cameras, b) Scheimpflug arrangement [34]

The post processing of the raw images compromises a whole field of computational methods in itself. Traditionally when using planar PIV the out of plane motion of particles will cause an error to be introduced in the in plane velocity components, this is shown in fig. 2.18 by the red camera. The orange particle moves in two dimensions, but is only captured in one dimension. The resulting observed velocity vector by the red camera is also drawn in red and is an overestimation of the true velocity component parallel to the laser sheet. The blue camera on the other hand is oriented such that the particle moves straight towards the camera, in this case the camera does not perceive any change in the position of the particle. It are these errors that are employed by SPIV to obtain the magnitude of the third velocity component. The differential error obtained by using two cameras provides the necessary information for the relevant computation in combination with the known information of the setup and the calibration.

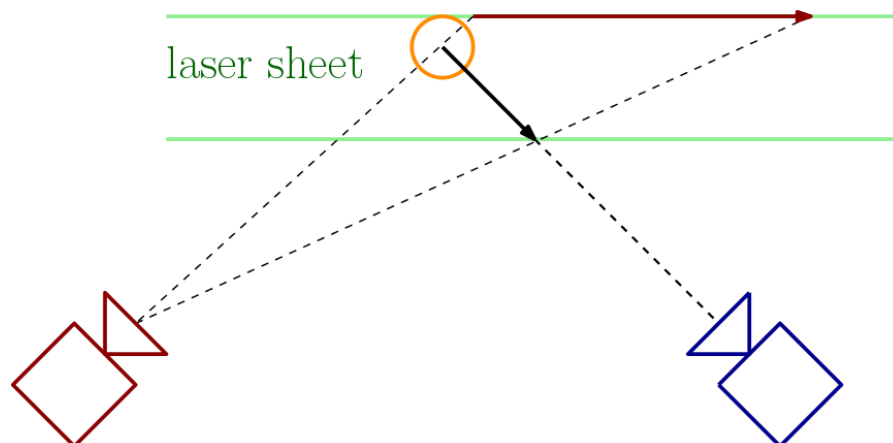


Figure 2.18: Out of plane error and SPIV out of plane component determination

As mentioned earlier the resulting velocity field consists of three velocity components in a two dimensional

plane. For unsteady turbulent flows it is important to capture all three velocity components, this allows for identification of vortical structures such as shown by Manolesos and Voutsinas (2014). Furthermore when the three dimensional velocity fluctuations are captured the Reynolds stresses can be calculated which in turn aids in the computational modeling of stall cells.

2.3.5. Force Gauge

Most of the research on stall cells has been focused on understanding the flow mechanisms and the behaviour of the stall cells. For that reason the focus has been on flow visualisation and quantifying the velocity field to obtain information about vortical structures. The latest experiments start to show an interest in measuring the forces on a wing in relation to the stall cells. Integral forces are converted to coefficients that should represent two dimensional performance. Although these coefficients are of great importance to design applications, representative coefficients are more difficult to obtain when stall cells play a role, such as was demonstrated by fig. 2.15.

For stall cell force measurements it is important to know the influence of the measurement apparatus on the flow. When using an external force gauge, this will provide the mounting points for the model. The mounting points often are protruding elements in the flow. The influence of these disturbances have to be taken into account in terms of altering the flow behaviour and the resulting forces. It is also possible to use internal force gauges, that are mounted inside the model. These will not disturb the flow. It is then possible to arrange the mounting of the model differently compared to the external force gauges, such that there are no protruding elements in the flow.

2.4. Computational Research

One of the factors preventing the advancement of knowledge about stall cells is that turbulence cannot be captured accurately by simplified Navier-Stokes simulations relying on turbulence modelling. This is demonstrated by the wide variety of turbulence models that are used in Computational Fluid Dynamics (CFD) these days. Therefore most observations of stall cells have come from experimental results, although as mentioned previously Manolesos et al. (2014) used computational methods to confirm experimental observations.

The field of Computational Fluid Dynamics (CFD) is focused on solving the Navier Stokes (NS) equations or a simplified version of them to obtain quantitative data of the flow field under observation. The most popular method for applications and relatively fast calculations is solving Reynolds Averaged Navier Stokes (RANS) equations. For this method the instantaneous flow is split in a time averaged part and a fluctuating part where it is attempted to solve the time averaged part of the flow. The simplifications introduces a closure problem of the equations as it creates Reynolds stresses that represent the effects of the fluctuating part of the flow. These Reynolds stresses are modelled with turbulence models. When it is known that some unsteady events take place in the flow under observation, time stepping can be introduced for the RANS equations. This results in the Unsteady RANS (URANS) approach. In research a more accurate method known as Large Eddy Simulation (LES) is used progressively more. This method solves the NS equations without averaging them, instead the flow is divided into different scales. The large scales are resolved if the grid resolution is high enough. The scales which cannot be solved due to the grid resolution being too low are called subgrid scales and are modelled. The grid requirements for useful application of LES are high and thereby also induce high computational costs. To bring down the computational cost a method which combines LES and RANS can be used. This method is called Detached Eddy Simulation (DES). DES attempts to solve as much of the flow as possible through the LES method, however the areas near the wall are solved by a RANS approach. This reduces the high grid resolution requirements with respect to that of LES. The DES method can also be forced to delay the switch from RANS to LES, in that case Delayed DES (DDES) is used. Lastly it can be mentioned that Direct Numerical Simulation (DNS) is the most accurate method by not employing turbulence models. The smallest Kolmogorov scales need to be resolved, thereby imposing high grid resolution and high computational power requirements.

In table 2.2 a summary is given of stall cell investigations in computational research. It can be seen that URANS and DDES are the most popular solver methods. This implies that the use of RANS and turbulence models at the wall are most common practice. The turbulence models used are mostly the one equation Spalart Allmaras (SA) model and the two equation $k-\omega$ SST model, described by Spalart and Allmaras (1992) and Menter (1994). Furthermore nearly half of the authors chose the NACA 0012 airfoil for their investigation. This airfoil often serves as a test case and benchmark at the same time due to its popularity in computational research.

Author	Airfoil	Re (10^6)	AR	# SCs	Formulation	TM
Bertagnolio et al. [4]	RISØ-B1-18	1.6	2.56	2	URANS, DES	$k-\omega$ SST
Zarutskaya & Arieli [47]	NACA 0012	4.6	8	5	RANS	SA, $k-\omega$ SST
Gross & Fasel [19]	NACA 64 ₃ -618	0.0642	0.2	1	DNS [16, 17]	
Kamenetskiy et al. [21]	NACA 0012	5	1	1	RANS	SA, $k-\omega$ SST
Manolesos et al. [29]	NTUA t18	1	1	0.5	URANS	SA
Manni et al. [25]	NACA 0012	1	10	2,4,6	URANS, DDES	$k-\omega$ SST
Prytz et al. [35]	NREL S826	0.05 - 1		1	RANS, DDES	$k-\epsilon$
Kaufmann et al. [22]	DSA-9A	0.9	6.2	4	URANS	$k-\omega$ SST
Liu & Nishino [24]	NACA 0012	1	2.5,4,6.4	2,3,4	RANS	$k-\omega$ SST

Table 2.2: Summary of CFD stall cell investigations in literature

Recent research by Manni et al. (2016) investigated stall cells on a high aspect ratio wing to avoid any interference caused by periodic boundary conditions. The wing had a NACA 0012 profile and was investigated with both URANS and DDES. The URANS calculations were performed with different grid resolutions and clearly show a big influence on the results, shown in fig. 2.19. This is one of the shortcomings of CFD. It is impossible to know when the results of a simulation are representative for what is attempted to be simulated. CFD can thus fulfil a supporting role to experimental observations. As it is difficult to obtain quantitative information of the full flow field of a stall cell experimentally, CFD can provide this information. However experimental results will be required to validate the CFD results. In most of the investigations mentioned in table 2.2 no validation with experimental results has been performed. Therefore the results shown in the articles cannot discuss effects of stall cells, but only the effect of the numerical CFD settings on the results.



Figure 2.19: Wall shear stress stall cell observations for URANS and DDES with different grid resolutions, figure from Manni et al. (2016)

2.5. Summary of Stall Cell Investigations

McCullough and Gault (1951) investigated different types of stall and classified them as thin airfoil, leading edge and trailing edge stall. The distinction between these three types is still used today and all three are accepted as predominantly two dimensional events. Moss and Murdin (1968) observed curved separation lines terminated by spiral nodes in the surface streaklines, whereas two dimensional stall was expected. Conditions for the formation of stall cells have been investigated ever since. Broeren and Bragg (2001) showed that stall cells can appear on airfoils which exhibit trailing edge stall or a combination of leading edge and trailing edge stall. Though it can be seen as obvious that an angle of attack at which stall occurs is required, it does not play a singular role. Multiple research articles have shown that the angle of attack at which stall cells appear is also dependent on the Reynolds number, even though there is no consensus on the influence. The actual creation of stall cells happens suddenly and is difficult to capture experimentally, however theories exist that suggest a Crow (1970) type instability might be the cause. Most of the recent experimental research has been focused on understanding the flow mechanisms in a sustained stall cell. Manolesos and Voutsinas (2014) used a combination of experimental and computational research to identify three key vortex structures in the stall cell. Two are parallel to the wing span and perpendicular to the free stream: the trailing edge line vortex and the separation line vortex. The third vortex type is the vortex coming off the spiral nodes and is called the stall cell vortex. Each stall cell has two stall cell vortices, they rise up from the spiral nodes, bend towards the stall cell center and then trail downstream. Once they trail downstream both of them induce an upwash near the center of the stall cell and a downwash outside of the stall cell. Early experiments already indicated that stall cells can exist on finite and swept wings also. Winkelman and Barlow (1980) showed that increasing the aspect ratio of a wing leads to an increase in the number of stall cells on the wing. This has led to speculation of a chord related length scale for stall cells, but again, no conclusive theory exists explain this or to predict the

amount of stall cells. Both the airfoil shape and the Reynolds number have been shown to have an influence but have not yet been investigated simultaneously. Stall cells have been observed to be steady or unsteady by different investigations. Both the Reynolds number and the turbulence intensity have been speculated to play a role in this, however experiments covering a wide range of Reynolds numbers performed by Dell'Orso and Amitay (2018) make no note of unsteady stall cells. In the case of unsteady stall cells, they have been stabilised with small spanwise disturbances that create a stall cell downstream of the disturbance. Recent experiments attempt to discover more about stall cells by obtaining quantitative data. Despite the advanced experimental measurement techniques, this has proven to still be very difficult. Identification of stall cells is traditionally done by means of SOFV or tufts, quantification of the flow field is obtained through pressure taps, force gauges or SPIV. To aid in the detailed quantification of the flow field CFD has shown to be a very capable tool. Most of the CFD research has been making use of URANS and DDES with SA and $k - \omega$ SST turbulence models. With all the available tools there are still many questions to be answered among which airfoil profile influence on the stall cell characteristics, or the Reynolds number effect on the required angle of attack for stall cell creation. Combinations of these parameters lead to different observations for which yet no explanations exist. The wide variety of airfoils used in previous research provide no useful basis for comparison and causes uncertainty regarding the influence of the airfoil shape. Currently there is a need for methodological research into the influence of the airfoil shape on stall cells to help unify previous research.

3

Methodology and Experimental Setup

3.1. Methodology

In chapter 2 the most relevant literature has been discussed. The literature provides an overview of the most relevant research that has been done and how it contributes to the knowledge of stall cells. At the same time it shows that stall cells are not yet fully understood. Ideas for research can be derived from hiatus in publications which leads to the research objective, discussed in section 3.1.1. In section 3.1.2 it is discussed how the research objective can be achieved with the available resources.

3.1.1. Research Objective

For the research discussed in this report the main resources have been a NACA 0012 wing with movable flap, a wind tunnel and a range of common experimental aerodynamic measurement techniques. Each resource has its own limitations such as will be discussed further into the report. Some exploratory experiments have been conducted first. These experiments were intended to give an overview of the flow behaviour of the stalling wing that has been used in this investigation.

From literature it has been shown that the two most important parameters for stall cell behaviour are the Reynolds number and the angle of attack. Different experimental investigations have used different airfoils and treated stall cells as independent of the airfoil shape. The research into the minimum required angle of attack and Reynolds number for stall cell formation has shown that the airfoil shape cannot be ignored. Results published by Manolesos and Voutsinas (2014) and Dell'Orso and Amitay (2018) both discuss the angle of attack and Reynolds number requirements with contradicting results regarding the trend. The results are shown in fig. 3.1 and can be seen to not even be in a similar range. This indicates that there is at least one factor which is being overlooked in this analysis.

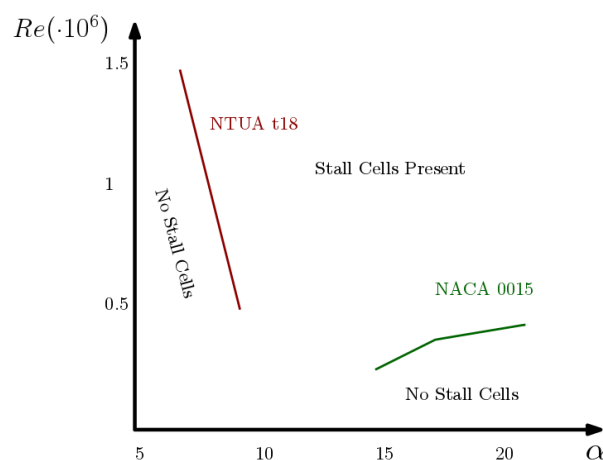


Figure 3.1: Superimposed results of Manolesos and Voutsinas and Dell'Orso and Amitay for stall cell requirements [8, 26]

Manolesos and Voutsinas (2014) used an NTUA airfoil, a cambered airfoil with a thickness of 18% . Dell'Orso and Amitay (2018) used the symmetrical NACA 0015 with 15% thickness. The NACA 0012 wing with movable flap that is available allows for the investigation of the effect of the profile thickness by comparing with the NACA 0015 results. Additionally the movable flap can be used to investigate the effect of camber on the stall cell characteristics. This leads to the following research objective.

The research objective is to contribute to the understanding of the requirements for the formation of stall cells by investigating the airfoil shape influence on the minimum required angle of attack and Reynolds number to form stall cells.

The research objective can be broken down in research questions to create smaller achievable goals that contribute to the understanding of the stall cell requirements. The research questions are described below.

Research Questions: What is the required combination of angle of attack and Reynolds number for stall cell formation for a NACA 0012 wing with different flap angles?

- What is the required combination of angle of attack and Reynolds number for stall cell formation of a NACA 0012 wing?
- How do the NACA 0012 results obtained compare to NACA 0015 results from literature?
- How does the required combination of angle of attack and Reynolds number for stall cell formation of a NACA 0012 wing change for different flap angles?

3.1.2. Research Strategy

Manolesos et al. (2014) performed a preliminary investigation with tufts to identify the required combination for the angle of attack and the Reynolds number. Only a limited amount of combinations were considered leading to a linear trend in a Reynolds number range of 0.5 to $1.5 \cdot 10^6$. Dell'Orso and Amitay (2018) used SOFV for many combinations of angle of attack and Reynolds number, leading to a flow phase diagram. The flow phase diagram from Dell'Orso and Amitay is in a Reynolds number range of 0.2 to $0.5 \cdot 10^6$. For the preliminary experiments that have been performed it has been attempted to use tufts to obtain a flow phase diagram such as shown in fig. 2.8.

For the first experiments the full wing with an AR of 5.2 has been used to create a flow phase diagram similar to Dell'Orso and Amitay (2018). The wing has been installed in the wind tunnel spanning from the ceiling to the floor in a 2D configuration. Next the wing was covered with tufts and a camera mounted outside of the wind tunnel. Two initial observations were the main goal. First identifying how the NACA 0012 wing stall behaviour is in comparison to the NACA 0015 wing used by Dell'Orso and Amitay. A similar AR and Reynolds number range have been used to isolate the influence of the airfoil shape. Next the influence of the flap angle was investigated, in order to relate this change to a change in camber.

Each different angle of attack, flap angle and Re setting has then been recorded for approximately 20 seconds to ensure that the recording is representative for the flow scenario. The recordings are consequently reviewed and processed into images. This then has lead to the creation of three flow phase diagrams, one for each flap angle. The flap angles that are used are zero, five and ten degrees. These angles have been chosen such that the difference is noticeable in the data without creating a large discontinuity in the camber. The angle of attack covered a wide range starting right before stall to well beyond stall, resulting in a range of 11.4° to 18.5° . The Reynolds number had a lower limit dominated by wind tunnel velocity readings. The upper limit was determined by the maximum holding torque of the stepper motors of the wing, such that the wing can be kept at a stable angle of attack. These limits resulted in a range of $1.0 \cdot 10^5$ to $5.1 \cdot 10^5$.

During testing with the tufts unsteady behaviour of the stall cells had been noticed. Manolesos and Voutsinas (2014) mentioned that this might be caused by the Reynolds number or the turbulence intensity. As the Reynolds number has been varied it leaves the turbulence intensity to be investigated to evaluate the influence of both the Reynolds number and turbulence intensity combined. In order to map the turbulence intensity a traversing beam has been build to hold the hot wire probe such that measurements can be taken over a wide area in the test section. The traversing structure had been constructed to have the hot wire probe at the location

of the leading edge of the NACA 0012 wing when it is installed. For the turbulence intensity measurements a hot wire has been operated in constant temperature mode. The fluid temperature has been written down from the read out of the wind tunnel sensor. The measurements of the hot wire anemometry have then been processed to obtain the turbulence intensity within the test section.

After the initial experiments it has been decided that the flow phase diagrams obtained with tufts need higher resolution in terms of angle of attack and Reynolds number. Additionally the high aspect ratio wing has been covered already. Therefore the half wing with an aspect ratio of 2.6 can be used. This allows for a closer comparison with the data from Manolesos et al. and additionally it leads to a more controlled stall cell. The reduction of the aspect ratio reduces the amount of possible flow scenarios. In order to obtain data which is still representative for a 2D configuration an endplate has been constructed. The endplate will be shown to not fully replicate a 2D scenario.

The lift coefficient has been obtained for all tuft measurements to combine this data with the flow phase diagrams. The combination of the flow phase identification with quantitative data has not been performed before within a parametric study of this size. The large scale investigation provided more detailed information about flow behaviour that occurs over only small Reynolds number or angle of attack ranges, and how these relate to the lift coefficient.

For the half wing it also has been decided to obtain quantitative information about the stall cells by investigating the characteristic stall cell vortices. The use of SPIV allowed to locate these stall cell vortices in the wake. The stall cell vortices are present in a highly turbulent wake, in order to capture them the laser sheet for SPIV has been put right at the trailing edge. By analysing each individual instantaneous result it has been made possible to investigate the unsteadiness of the stall cell.

3.2. Experimental Setup

The methods that have been used for the experiments have been described in short. In this section the information regarding the setup applicable to the experiments that have been performed are described with the relevant specifications.

3.2.1. Wind Tunnel

All of the experiments described in this report have been conducted in the 7x5 wind tunnel of the University of Southampton. This is a return wind tunnel with a closed test section and operates at atmospheric static pressure. The test section has a predominantly rectangular shape with chamfered corners, such as shown in fig. 3.2. The height of the test section is 1.6 m and the width is 2.1 m. The wind tunnel has a maximum velocity of 50 m/s, with an accuracy of ± 0.02 m/s. The velocity is calculated from the pressure measurements of two pitot tubes at the beginning of the test section. Furthermore at the beginning of the test section a temperature sensor is present close to the wall.

3.2.2. Wing

A carbon fibre wing with a NACA 0012 profile is available specifically for the 7x5 wind tunnel. The wing has a span of 1.57 m and a chord length of 0.3 m, which gives an aspect ratio of approximately 5.2. It is also possible to use only half of the wing span, leading to an aspect ratio of approximately 2.6. For experiments that will be performed in this report it is required to have two dimensional behaviour for the half span wing. Therefore an endplate has been constructed to mimic the behaviour of a wing connected to a wall. Furthermore, the wing is equipped with a plain flap which has a chord of 0.1 m, or equivalently 0.33 chord.

The wing is electronically controlled by two stepper motors to set the angle of attack and the flap angle. The stepper motors can be set to an angle with an accuracy of 0.1 degree.

The operational limit of the wing is determined to be 25 m/s in terms of freestream velocity. At this free stream velocity the wing starts to show vibrations during stall. It was also noticed that this condition is near the limit of the holding torque of the stepper motors.

Finally it can be noted that the wing is installed in a vertical position. For experiments conducted on the full wing a distinction will be made between half of the span near either the ceiling or the floor of the wind tunnel.

These half span ranges will be referred to as the top and bottom half respectively. For experiments conducted on half the aspect ratio, only the top half of the wing is used.

3.2.3. Hot Wire Anemometry

For the measurements conducted with hot wire anemometry, probes were constructed with 5 μm diameter tungsten wire. The probe is inserted in a probe holder which is clamped in a small airfoil shaped support. This small support is connected to a large wing shaped beam with a thick metal rod. The probe extends approximately 20 cm upstream of the small support, which in turn extends approximately 15 cm upstream of the large wing shaped beam. The probe is thus approximately 35 cm upstream of the large wing shaped beam, this minimises the upstream influence of the beam on the measurements while keeping the support as stiff as possible.

The large wing shaped beam spans the height of the wind tunnel cross section and can move left and right. The probe holder and its support can move up and down along the large wing shaped beam. This allows the hot wire probe to be positioned almost anywhere in a cross sectional plane of the wind tunnel, fig. 3.2 shows this setup.

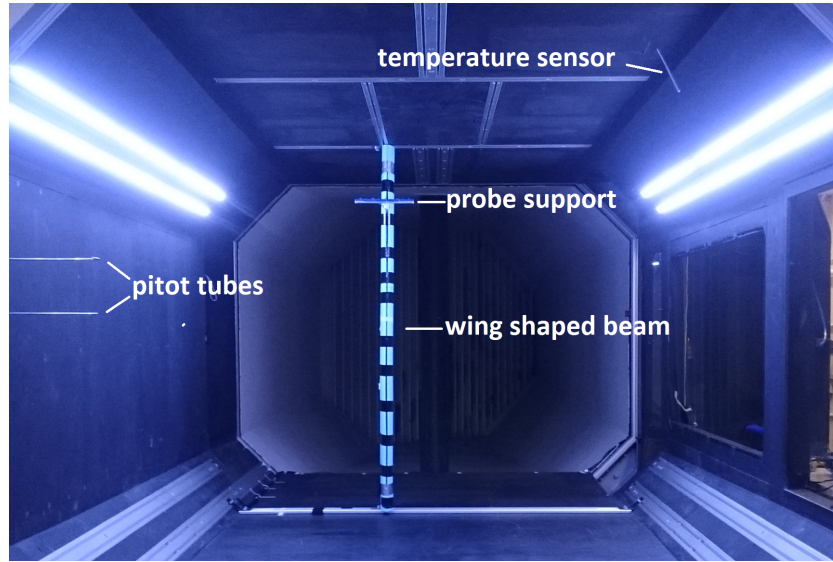


Figure 3.2: Hot wire anemometry setup in the wind tunnel

The hot wire is operated in a constant temperature mode which is controlled by a Wheatstone bridge. The overheat ratio is an indication for the resolution that is achieved in terms of resistance of the probe wire and can be calculated according to eq. (3.1).

$$a = \alpha_0(T_w - T_0) = \frac{R_w - R_0}{R_0} \quad (3.1)$$

Where α_0 represents the temperature coefficient of resistance ($0.36 \cdot 10^{-3} [1/^\circ\text{C}]$ for tungsten), T_w the wire working temperature, T_0 the fluid temperature (15°C), R_w the hot wire resistance, R_0 the cold wire resistance. The overheat ratio is selected to be 0.72, leading to an operating temperature of 215°C .

A Dantec multichannel CTA 54N82 is used to control the hot wire operating temperature. This system uses binary switches to set the overheat ratio, a manufacturer supplied spreadsheet takes the test setup as an input and outputs the required switch positions for the desired set up. The Dantec system outputs an analogue signal which is sampled with a National Instruments NI DAQ 6251 at 10 kHz for 120 seconds, and sent to a receiving computer.

3.2.4. Tufts

The attached end of the tuft should resemble a friction free ball joint as close as possible. This will allow the tuft to have the most freedom to move. Additionally this will be aided by having flexible tufts that can bend easily. The goal is for the tufts to bend and move in the directions of the flow as easily as possible. Furthermore the pieces are required to be small enough to show large scale flow structures. Finally with the goal of visualising unsteady behaviour, the tufts should have a minimal inertia and thus weight.

When tufts are selected, the wind tunnel can be turned on and flow structures will be shown by the tufts following the flow. The resulting position or motion of the tufts is then photographed or recorded. To aid in image acquisition it is preferred to have a high contrast between the tested object and tuft color.

With some trial and error the optimal wool tuft size for a specific object and flow case can be found. In the case for the wing tested a tuft spacing of approximately 5 cm is used in both spanwise and chordwise direction. The lengths of the tufts are cut such that tufts cannot get entangled with neighbouring tufts.

3.2.5. Force Balance

A force gauge exists in many different forms, for wind tunnel application a distinction can be made between internal and external force gauges. Internal force gauges have the benefit of being mounted inside the model that is tested to prevent any protruding elements disturbing the flow. An external force balance allows for a multitude of applications but often requires attachment points inside the test section to be mounted on the model itself. The influence of these protruding force balance struts can be measured separately but not the interaction between the model and the force balance struts. Most of the modern force gauges are electronic and are build out of strain gauges. These strain gauges are specifically positioned and calibrated resulting in an output signal that is converted to forces.

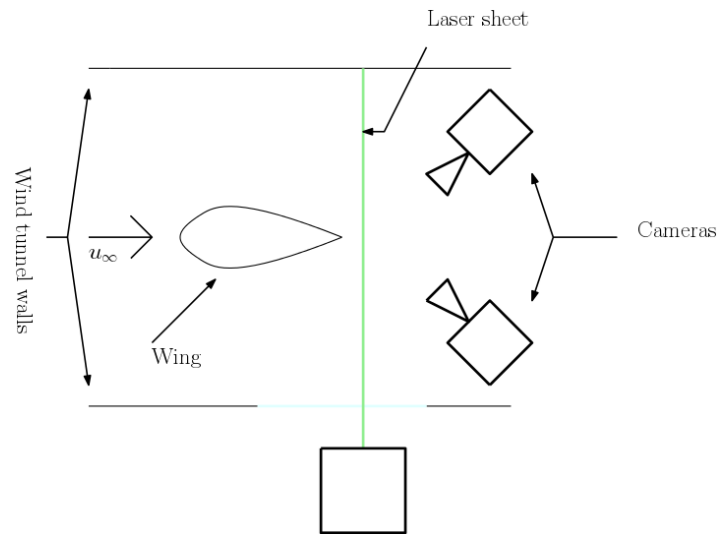
The force balance that is used to acquire the forces and moments is a six axis force and torque transducer. The model used is a ATI Industrial Automation Delta IP65. This system is mounted in between the wind tunnel support structure and the wing. The force and torque transducer comes with the relevant calibration matrix from the factory. Prior to testing this calibration has been checked for the force directions corresponding to lift and drag during testing and found to be compliant with manufacturer specifications. During the testing the force measurements are calibrated by performing zero runs when required. The resolution for the transducer is also given by the manufacturer. For forces the resolution is 1/32 N and for the pitching moment 1/528 Nm.

3.2.6. Stereoscopic Particle Image Velocimetry

The SPIV setup used a Litron Lasers Bernoulli 200-15 laser, this is a Nd:YAG laser emitting light at 532 nm. The laser has been operated at full power resulting in 200 mJ pulses. The laser was located outside the wind tunnel, a cylindrical lens attached directly on the laser created a laser sheet. The laser sheet was shot through the side window of the wind tunnel, perpendicular to the freestream flow and 0.5 cm behind the trailing edge for the wing and flap at zero degrees. The result is shown in fig. 3.3. The required smoke is generated by a Magnum 1200 fog generator. The average particle size of this machine is approximately 1 μm .



(a) Picture of the laser sheet for SPIV



(b) Schematic top view of the SPIV setup

Figure 3.3: SPIV setup

Imaging is done with two 29 MP CCD cameras of the type Imager LX from LaVision. The cameras are positioned downstream of the wing such as shown by fig. 3.4b. The lenses used for the cameras are two 100 mm lenses mounted on a Scheimpflug adapter. One of the cameras is operated in forward scatter and has the aperture of the lens set to $f/5.6$. The other camera operates in back scatter and needs a larger aperture to capture enough light to give a similar result to the forward scatter camera, therefore the aperture for the second camera is set to $f/2.8$.

Calibration, image acquisition and processing of the raw images is done with DaVis. The calibration is performed with a 3D calibration plate at approximately the middle of the Field Of View (FOV), shown by fig. 3.4a. The calibration plate is touching the trailing edge with the wing at zero degree angle of attack. The calibration is extrapolated by DaVis to extend to the full FOV. For the image acquisition the laser pulse separation was set to $20 \mu\text{s}$. At a freestream velocity of 20 m/s this results in streamwise particle movement of approximately 0.4 mm, which is well below the laser sheet thickness of approximately 3 mm. Before the processing of the particle images an average image is subtracted from the individual images to reduce some of the background and reflections. These resulting particle image pairs are then processed to obtain velocity vector fields. An interrogation window of 64×64 pixels with 75% overlap and double pass was found to give the best result in terms of noise reduction versus resolution. The result are vector fields with a resolution of 408 by 289 vectors, this implies a resolution of approximately 1.9 mm ($0.63\% x/c$) in the object plane.

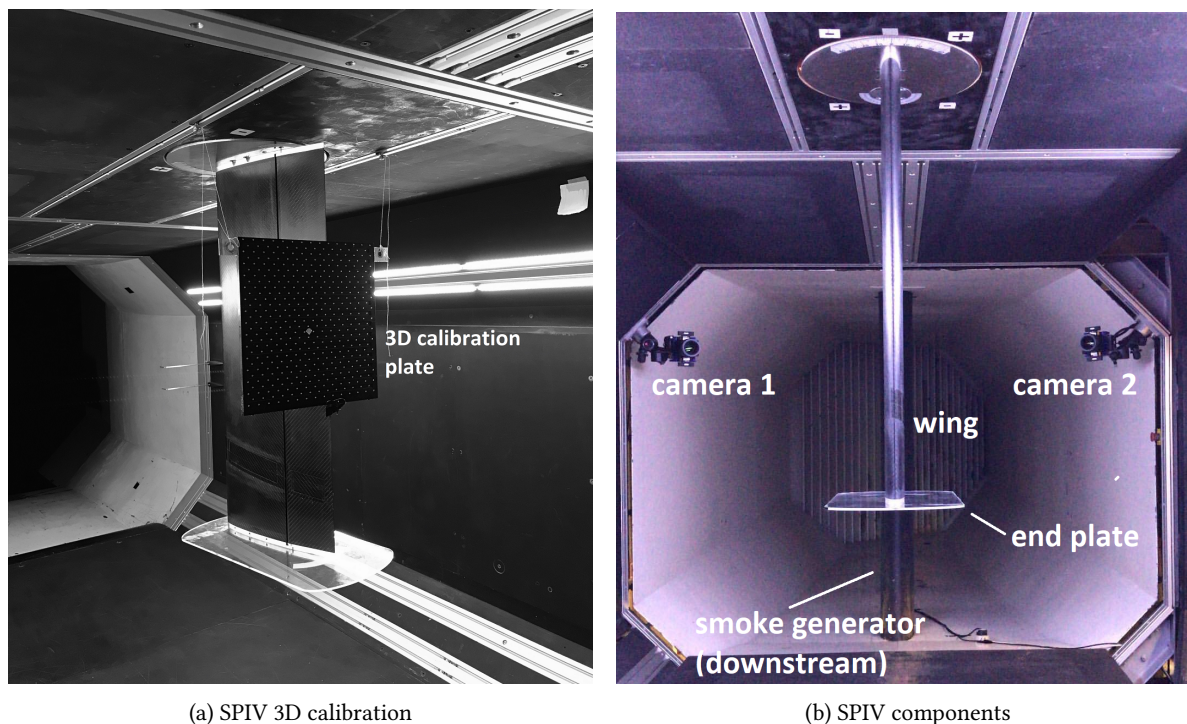


Figure 3.4: SIV setup

3.2.7. Surface Oil Flow Visualisation

Multiple methods for flow visualisation exist, the use of tufts such as described before is one of them. As tufts introduce a small disturbance into the flow, they might influence the the flow itself. Surface oil flow visualisation is an alternative method to show the flow behaviour at the object surface. The oil effectively replaces the object surface. In order to achieve optimal results the viscosity and the volatility of the oil need to be tailored to the application.

For the experiments performed in this report with SOFV a premixed container of an unknown petroleum derivative and fluorescent chalk has been used. A LED UV floodlight is used to enhance the visibility of the resulting patterns. During the experiments different methods for applying the mixture have been tested. These include: sparsely sprayed on, thickly sprayed on and applied with a paint brush. From the different methods it was observed that the thickly sprayed on coating performed the best. One of the reasons for the thickly applied coating performing best is the high volatility of the substance used. It has been observed that a large part of the mixture on the wing dries within approximately the same time it takes the wind tunnel to reach the desired velocity. The low viscosity in combination with a low freestream velocity and a vertical wing setup leads to a relatively high influence of gravity compared to the flow behaviour. Therefore a high wind tunnel velocity was chosen, namely 20 m/s.

The SOFV mixture that has been used thus has a volatility which is too high and a viscosity which is too low. This resulted in flow patterns that are more difficult to interpret and show a bias caused by gravity. Due to the bad quality of the results they are not taken into account in the analysis. An example of the results is shown in appendix B.

4

Data Processing and Corrections

When the experiments have been performed and data has been acquired it needs to be reduced to useful information. In some cases, prior to the data reduction, corrections need to be applied to the data in order to have data that is representative for the test conditions. In this chapter the processing of the data for each experimental method where it is required is discussed.

4.1. Blockage Correction

The first correction to be considered is due to blockage effects. These corrections are applicable when an object is placed in a wind tunnel and thereby changes the effective freestream velocity. The freestream velocity is measured upstream of the object under investigation. In free air the freestream velocity would be measured correctly. Due to the fixed cross section of the wind tunnel the law of continuity requires the velocity at the tested object to be higher due to the reduced cross sectional area as a result of the tested object obstructing the flow. Furthermore the wake of the object also causes a similar blockage effect, discussed in more detail in Barlow et al. (1999).

The wind tunnel has a cross sectional area of 3.36 m^2 at the test section. The wing has a span of 0.78 m (AR 2.6) and a chord of 0.3 m , with the flap 0.1 m of the chord. When the flap has a deflection of 10° and the wing is at an angle of attack of 20° , this leads to a maximum frontal area of 0.09 m^2 for the wing. The solid blockage can then be found to be 2.8%. For the experiments presented in this report the influence of the solid blockage effects is small and therefore neglected.

The wake blockage mainly has an influence on the drag by not allowing the wake to fully expand as in free air. This causes the measured drag in the wind tunnel to be lower than the true value in free air. The drag values are not used in the analysis and thus no corrections are required.

4.2. Hot Wire Anemometry

A well established method to measure velocity fluctuations in the flow is with hot wire anemometry. In this report results are presented that have been acquired with constant temperature anemometry. This method measures the cooling capacity of the flow to determine the velocity of the flow. Therefore it follows that this method is also sensitive to temperature changes that are not induced by changes in the flow velocity. Furthermore the use of a hot wire anemometer requires the construction of a calibration curve to convert measured voltage into the corresponding flow velocity.

For each velocity that is measured also the temperature is noted. The wind tunnel used for the experiments is a closed circuit wind tunnel which runs partially outdoors and partially indoors. At low velocities the outdoor temperature is low enough to cool the airflow going through the wind tunnel. At high velocities the heat added to the flow by the fan is larger than the cooling by the outdoors section, causing the temperature of the airflow to increase.

The calibration follows from measuring the output voltage for different freestream velocities as registered by the wind tunnel pitot tubes. For each velocity that is measured the mean output voltage is used. Before a

calibration can be constructed the mean output voltage has to be corrected for the changing temperature. This correction can be applied according to the formula given by Bruun (1995), which is shown in eq. (4.1). In eq. (4.1) E represents the voltage, T_w is the operational temperature of the hot wire, T_d is the desired temperature for calibration and T_a is the ambient temperature inside the wind tunnel at which the measurement was performed. From the equation it can already be seen that with a high operating temperature for the wire the resulting corrections are small. For each measurement the ambient temperature changes, corrections are generally less than 1%. An exception occurs when the air in the wind tunnel has been stagnant for a long time and has reached a high temperature in the test section, leading to a correction of approximately 2%.

$$E_{corrected}^2 = E_{measured}^2 \left[\frac{T_w - T_d}{T_w - T_a} \right] \quad (4.1)$$

$$E_{corrected}^2 = A + Bu^n \quad (4.2)$$

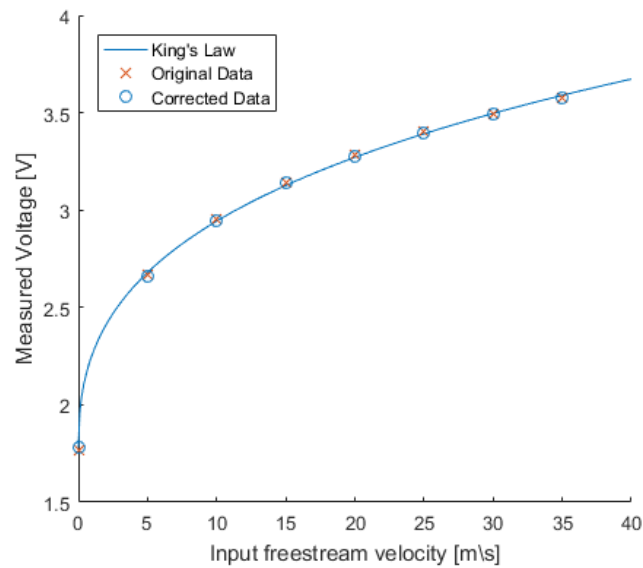


Figure 4.1: Hot wire anemometry King's law calibration

The resulting corrected data is shown in fig. 4.1. A curve can then be fitted to the data according to King's law, such as shown by eq. (4.2). The King's law relates the input velocity u with the measured output voltage E . In the equation A , B and n are coefficients to be determined by the curve fit. In fig. 4.1 this curve fit for King's law can also be observed, for the data used the values for the A , B and n coefficients are 3.17, 1.93 and 0.46 respectively.

A calibration as such is constructed for every top and bottom position in the wind tunnel, this allows to assess potential differences in calibration. The measurement locations in between can then use a calibration which is an interpolation of the calibrations on the same spanwise position. The data from a measurement is collected over a period of two minutes and can have a slight linear trend to it which is not caused by the flow but likely by the Dantec control system. This trend is removed from the data with the MATLAB detrend function, while maintaining the average and the fluctuations. This allows for the calculation of the Turbulence Intensity (TI) according to the formula shown by eq. (4.3).

$$TI = \frac{\text{rms}(u')}{\bar{u}} \quad (4.3)$$

4.3. Force Measurements

In this section hysteresis effects between separate runs, pitching moment induced angle of attack corrections and calibration inaccuracies are discussed. The corrections are discussed in the order in which they are applied.

4.3.1. Hysteresis Correction

As has been explained in the literature review, the stall cell vortices encourage stall cells to sustain once they are created. When a stall cell is triggered in a certain configuration it tends to stay in that configuration. It also has been mentioned how stall cells can be triggered by small disturbances. A small random disturbance can thus trigger a specific stall cell configuration and this will thus effect the performance of the wing and will persist throughout the remainder of the angle of attack sweep. This effect is in a sense similar to the standard understanding of stall hysteresis. In this text the hysteresis correction refers to the tendency of the stall cell configuration to remain similar to the configuration such as triggered initially.

Acquiring force coefficients for a specific flap angle and velocity has been done in two runs. A first run goes from 0 to 20 in steps of 1° for the angle of attack, a second run goes from 0.5 to 20.5 in steps of 1° . The software used for the control of the wing allows micro steps for calibration but only allows integer angle of attack steps for the different measurements, leading to the two separate runs that have been performed. In fig. 4.2 the blue curve indicates the original data before any modification. The linear region shows good agreement between the two runs. Beyond stall it can be seen that the original data has some zig zag behaviour to it. This is explained by having two separate runs that might experience different flow behaviour due to the initial 0.5° offset and a slightly different stall cell configuration that is triggered initially. This flow behaviour will then persist throughout the rest of the angle of attack sweep. fig. 4.2 shows that this behaviour has a small influence, however at lower freestream velocities the hysteresis effect is larger. This effect is corrected by using a moving average of two data points, an example result of this is shown in fig. 4.2 by the red curve. For all the force and moment coefficients this correction is applied.

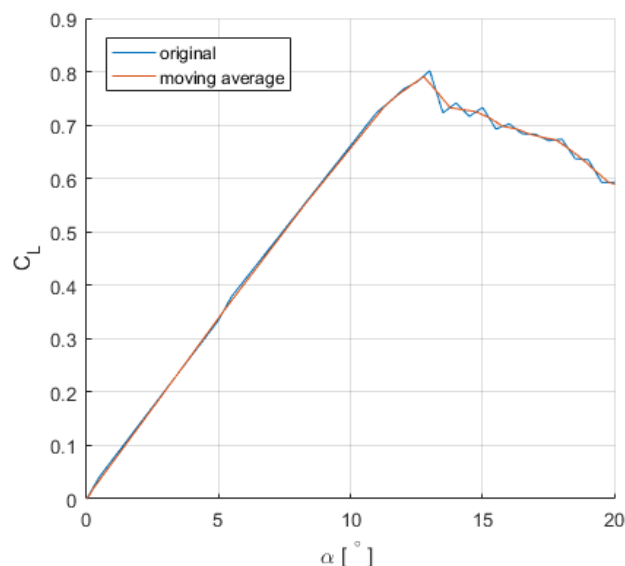


Figure 4.2: Moving average of two points for freestream velocity 20 m/s and flap angle 0°

4.3.2. Pitching Moment Correction

During the testing the wing had to be repeatedly recalibrated after the holding torque had been released from the wing. When the holding torque was reapplied this was also checked by applying a pitching moment manually. During these checks it was noticed that the actual wing angle deviates slightly from the angle of attack that had been set, due to some play in the setup and the stepper motor providing insufficient torque.

This angle of attack deviation is inherent to the setup as it was installed and was therefore not given more attention at the time of testing. During testing it was noted that applying a pitching moment to the wing in a fixed position could cause a deviation of 1° in the direction of the pitching moment. The required moment for larger deviations than 1° increased drastically.

These observations showed that the pitching moment applied to the wing around the pitching axis directly causes a deviation in the angle of attack, up to 1° . The force measurements acquired include this pitching

moment. In order to link the moment force to the displacement of the wing, the response of the full system needs to be known. Since the exact relation between the pitching moment and the angle of attack deviation is not known, it is approximated based on the observations made during testing. The approximation is considered valid due to the small range of pitching moments measured.

A deviation of 1° angle of attack due to the pitching moment is deemed to be realistic during testing as caused by the aerodynamic forces. The maximum pitching moment of all flow cases that have been tested is approximately 2.5 Nm and the minimum is approximately -1.5 Nm. The maximum pitching moment is experienced at maximum lift, maximum velocity with the flap angle equal to zero. For this flow case the centre of pressure is most forward towards the leading edge, with the pitching axis being positioned behind the quarter chord point thereby resulting in a large pitch up moment. Right after maximum lift when stall occurs the centre of pressure shifts towards the trailing edge and causes a negative pitching moment, this is also shown in fig. 4.5. When the flap angle is increased, so is the pressure difference between the suction and pressure side of the wing. The change in airfoil geometry causes the pressure difference near the flap to increase. Since this region of increased lift is behind the pitching axis this induces a pitch down moment.

The correction that is applied has a maximum deflection of 1° in either direction. The required moment to achieve this deviation is chosen to be 2 Nm. It is likely that in reality the deviation caused by the pitching moment is less than what is assumed for the correction. This implies that the real deviation can be smaller than the one that will follow from these corrections. The corrections to the angle of attack are done according to the curve presented in fig. 4.3.

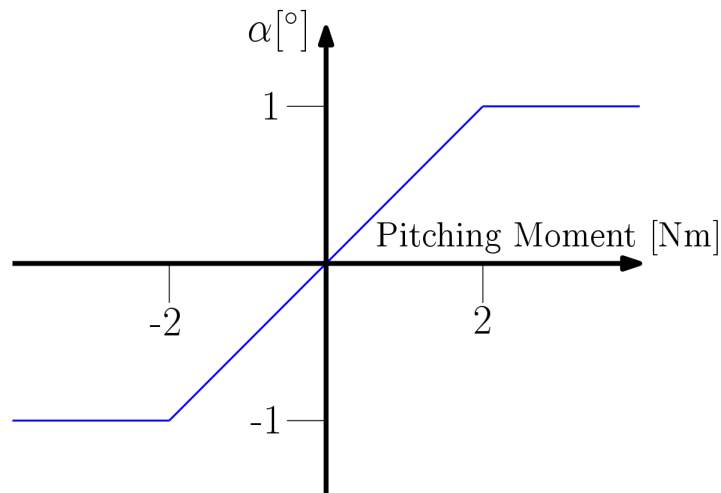


Figure 4.3: Angle of attack deviation for measured pitching moment

For each combination of parameters tested the moment is known and thus the angle of attack deviation follows from the curve in fig. 4.3. An example of the resulting correction to the angle of attack is shown in fig. 4.4. This case is selected because it has the highest freestream velocity that has been used. The flap angle is less relevant as for different flap angles the value of the moment changes, but the range of moments for an angle of attack sweep still is approximately 2.5 Nm between the minimum and maximum pitching moment at 25 m/s.

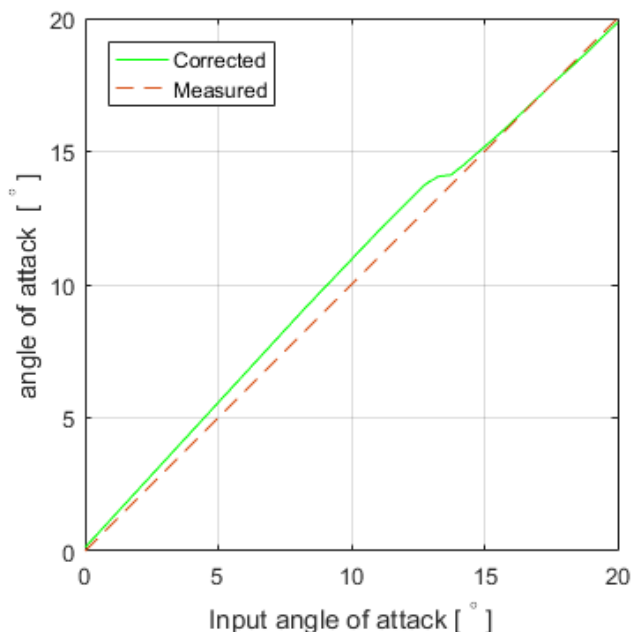


Figure 4.4: Pitching moment corrected angle of attack for freestream velocity 25 m/s and flap angle 0°

For case shown in fig. 4.4 the maximum angle of attack deviation at any given angle of attack is 1° . This is because of the limit deviation for either positive or negative moments. It is possible to have a deviation which is larger than 1° between two consecutive angles of attack around stall where the pitching moment suddenly switches from highly positive to highly negative. However as mentioned earlier, the maximum pitching moment range is approximately 2.5 Nm, leading to a maximum deviation of approximately 1.25° between consecutive angles of attack.

It can thus be reasoned that there are two ranges of angles of attack that are most influenced by the corrections. The first is where a high absolute pitching moment is measured, leading to a large angle of attack correction. The second is the angle of attack range where the pitching moment changes abruptly, leading to large corrections between consecutive angles of attack.

Finally it follows that the described deviation for the angle of attack is applicable to all the measurements done as the wing has always been controlled by the stepper motors. All the half wing data in this report has been corrected for the pitching moment induced angle of attack deviation.

4.3.3. Flap Misalignment Correction

During the calibration of the wing, the flap was manually aligned with a visual marker and measured to be at approximately 0° deflection with respect to the wing chord. Then the wind tunnel was run at 20 m/s and the lift coefficient for angles of attack close to zero were monitored to find the required setting for the angle of attack to have zero lift. This process has been performed in the same way consistently throughout all the experiments. However the method did not take into account small misalignments of the flap. These became apparent in the data from the experiments where it can be observed that although the lift is zero at angle of attack zero, the moment is not zero, as is shown in fig. 4.5.

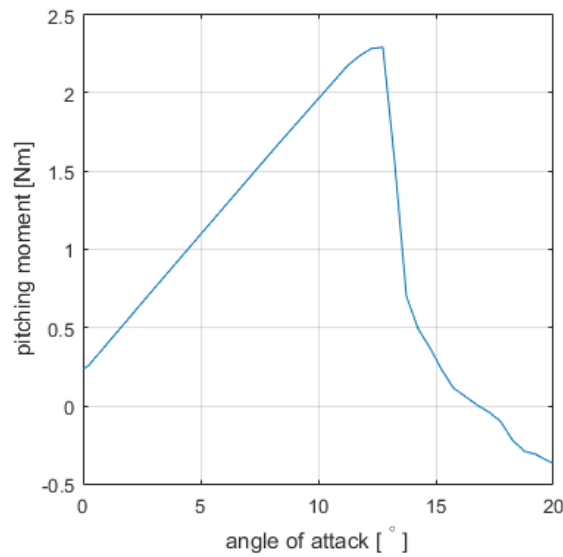


Figure 4.5: Measured pitching moment for freestream velocity 25 m/s and flap angle 0°

A positive pitching moment indicates that a positive angle of attack is set. With the lift measured to be zero it can be reasoned that the deflection of the angle of attack and flap angle are both present and cancel each other out in terms of resulting lift.

With a linearisation of this problem a first order approximation can be found for the angle of attack and flap angle difference. Which within the approximation can also give the resulting change to the lift and moment. For a linear problem with two unknowns, two equations are required. The first equation will require the lift coefficient to be zero at zero angle of attack. The second equation will require the moment coefficient to be zero at zero angle of attack.

It is known that both the flap angle and the angle of attack have an influence on the lift coefficient. Since data has been acquired for a range of angles of attack and flap angles, it is possible to make a first order approximation to model this influence. The required gradients of the lift coefficient are obtained from the data which has been corrected for the pitching moment. For different flap angles the lift coefficient data for 20 m/s is chosen to be in line with the calibration procedure. Since the deviation for the angles is small the gradients are obtained in the linear region near angle of attack zero, an indicative graph is shown in fig. 4.6. For the angle of attack influence on the lift coefficient this is a good approximation due to the linear region. For the flap angle influence on the lift coefficient it is a more crude approximation. In reality an increase in flap angle will also decrease the stall angle, this effect is not taken into account in this correction.

For the lift coefficient the reasoning is that a shift in angle of attack will change the lift at zero angle of attack to a non zero value. The flap angle can then compensate this lift change in opposite direction. With the gradients for the lift coefficient known the following equation can be obtained. Where α represents the angle of attack and β represents the flap angle.

$$0 = \Delta C_L = d\alpha \frac{dC_L}{d\alpha} + d\beta \frac{dC_L}{d\beta} \quad (4.4)$$

With $\frac{dC_L}{d\alpha} = 0.0646$ for constant flap angle, and $\frac{dC_L}{d\beta} = 0.0462$ for constant angle of attack, this leads to the following relation.

$$d\beta = -1,40 \cdot d\alpha \quad (4.5)$$

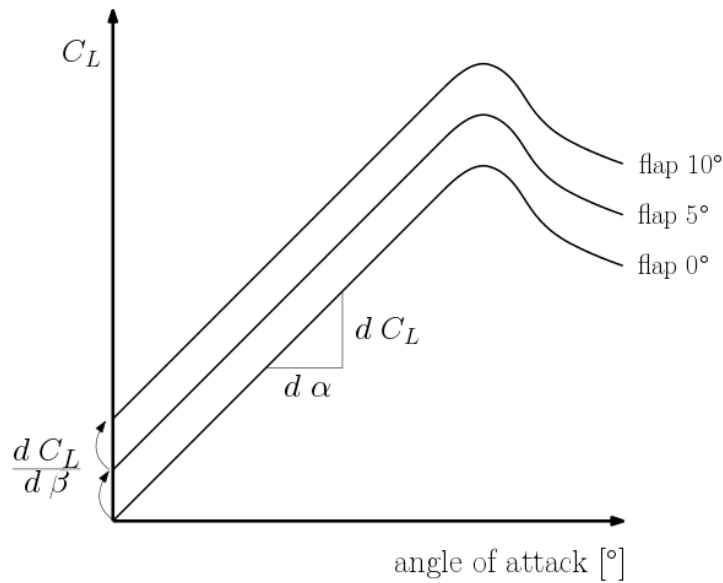


Figure 4.6: Lift coefficient gradients for misalignment correction

The second equation follows the same approach as used for the first equation, but now with respect to the pitching moment, in which case the angle of attack and flap angle deviation complement each other instead of counteracting each other. A decrease in angle of attack gives a lower moment coefficient and an increase in flap angle also lowers the moment coefficient, as shown in fig. 4.7. Again it is required that the moment coefficient is zero at angle of attack zero with flap angle zero ($-C_{M0}$). With the gradients of the moment coefficient and the moment coefficient deviation at angle of attack zero known the following equation can be created.

$$-C_{M0} = \Delta C_M = d\alpha \frac{dC_M}{d\alpha} + d\beta \frac{dC_M}{d\beta} \tag{4.6}$$

With $-C_{M0} = -0.006$, $\frac{dC_M}{d\alpha} = 0.0062$ and $\frac{dC_M}{d\beta} = -0.0036$. Further filling in the relation shown in eq. (4.5), the equation can be solved for $d\alpha$ and $d\beta$. The required angle of attack correction is a reduction of 0.53° , with eq. (4.5) this gives a flap angle increase of 0.74° .

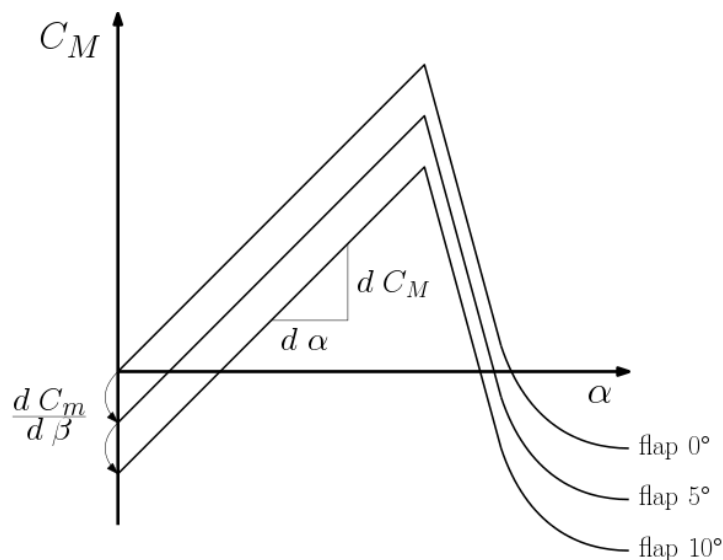


Figure 4.7: Moment coefficient gradients for misalignment correction

As can be expected these corrections are quite small. The corrections for the misalignment are applied after the pitching moment corrections to ensure that the gradients used are represented as close as possible to re-

ality. Since the calibration procedure was consistent for all the experiments that are shown the misalignment corrections are applicable to all the data. The correction for the flap angle will not be mentioned further in the report as it is constant and the change in between flap angle settings is more important than the absolute value.

4.3.4. Force Measurement Uncertainty

When performing the measurements for the forces and moments small deviations can occur due to the procedure or equipment used, these possible errors introduce uncertainty into the results that are obtained. The uncertainty can be quantified based on the knowledge of the measurements. For the quantification of the uncertainty in the results due to error propagation the approach as suggested by the National Physical Laboratory in Bell (2001) is used. The sources of the uncertainties are shown in table 4.1, all sources have been scaled to standard error. The scaling is done with the use of a divisor, for measurements this divisor is the square root of the amount of samples and for normal distributed uncertainties this is two. The angle of attack and velocity input values are limitations that are introduced by the equipment used, by the stepper motor control software and the wind tunnel velocity read out respectively. The reading of the forces (F) and moments (M) corresponds to the force balance accuracy, the values follow from manufacturer data. The measurement of the forces and moments reflects how closely the measurement represents the desired quantity to be measured, or the standard error of the mean of the measurements.

source	value (\pm)	distribution	divisor	std error (\pm)
α input	0.1°	normal	2	0.05°
u_∞ input	0.01 m/s	normal	2	0.005 m/s
F reading	0.03125 N	normal	2	0.016 N
M reading	0.00189 Nm	normal	2	0.001 Nm
F measurement	7 N ($F_{max} \cdot 0.1$)		$\sqrt{50000}$	0.031 N
M measurement	0.25 Nm ($M_{max} \cdot 0.1$)		$\sqrt{50000}$	0.001 Nm

Table 4.1: Sources of uncertainty for the force measurements

It can be seen that the standard error is expressed in different units. Additionally the main interest of the uncertainty is the uncertainty of the lift coefficient and the angle of attack. For both the lift coefficient and the angle of attack the final uncertainty is dependent on both the uncertainty of the acquired data and the propagation of that uncertainty throughout the corrections that are applied.

For the lift coefficient this implies the following.

$$C_L = C_{L_{measured}} + C_{L_{correction}} \pm C_{L_{uncertainty}} \quad (4.7)$$

Where the uncertainty is built up out of the measurement uncertainty and the correction uncertainty, these are assumed to be uncorrelated. This is shown in eq. (4.8).

$$C_{L_{uncertainty}} = \sqrt{C_{L_{m_u}}^2 + C_{L_{c_u}}^2} \quad (4.8)$$

The lift coefficient is dependent on the lift force and the velocity. Then the uncertainty of the lift coefficient is calculated as shown below in eq. (4.9). Where δ indicates the uncertainty of a parameter.

$$\delta C_L = C_L \cdot \sqrt{\left(\frac{\delta L}{L}\right)^2 + 2\left(\frac{\delta u_\infty}{u_\infty}\right)^2} \quad (4.9)$$

The measurement uncertainty follows from eq. (4.9) and the moment correction does not affect the lift coefficient. The flap misalignment correction corrects the lift coefficient with an offset, this addition of a constant does not affect the lift coefficient uncertainty but the lift coefficient itself does play a role in the calculation of the correction. Therefore, assuming the corrections are correct, the uncertainty of the lift coefficient is calculated as follows. Where the uncertainty of the measurements and corrections are equal for the lift coefficient. This results in substituting eq. (4.9) for both the measurement and correction uncertainty in eq. (4.8).

$$C_{L_{uncertainty}} = \sqrt{2 \left[C_L \cdot \sqrt{\left(\frac{\delta L}{L}\right)^2 + 2\left(\frac{\delta u_\infty}{u_\infty}\right)^2} \right]^2} \quad (4.10)$$

The uncertainty can then be calculated for each angle of attack, flap angle and velocity. With the uncertainties fixed, it can be seen that increasing the values for lift and free stream velocity will lower the relative uncertainty with respect to the measured quantities. Consequently at a velocity of 25 m/s with lift forces of approximately 70 N this results in a relative uncertainty of $2 \cdot 10^{-5}$ for the velocity and $4.4 \cdot 10^{-4}$ for the lift force. The relative uncertainty of the force measurements can be further reduced by increasing the number of samples to reduce the standard error of the mean such as shown in table 4.1. In fig. 4.8 the uncertainty for a single combination of flap angle and free stream velocity is shown.

For the angle of attack a similar approach can be used. Again the final value can be subdivided into the measured value, the correction and the uncertainty. Just as for the lift coefficient the angle of attack uncertainty can be split into a contribution from the measurement and a contribution from the corrections. The contribution from the measurement is equivalent to accuracy of the input and is equal to 0.05° . The contribution from the corrections is dependent on the two corrections used. The misalignment correction does not introduce any uncertainty. The moment correction on the other hand determines the angle of attack correction based on the moment measurement. The equation used for the angle of attack correction in the moment correction is now used for the determination of the angle of attack uncertainty, as shown in eq. (4.11).

$$\delta\alpha = \frac{\delta M}{2} \cdot 1 \quad (4.11)$$

Again it is assumed that the corrections that are applied are correct and uncorrelated. Then eq. (4.11) is only used for moment forces between -2 and 2 Nm, outside of this range the uncertainty introduced by this correction is thus also zero. Within the predefined moment range the uncertainty of the moment is a combination of the moment reading and measurement uncertainty. The total moment uncertainty is equal to 0.0014 Nm.

The total angle of attack uncertainty can then be found as shown by eq. (4.12). The total angle of attack uncertainty is dominated by the ability to set the input angle of attack accurately. This limited accuracy is inherent to the setup used and cannot be reduced further.

$$\alpha_{uncertainty} = \sqrt{0.05^2 + \left(\frac{0.0014}{2}\right)^2} = 0.05^\circ \quad (4.12)$$

The final uncertainty of the lift coefficient and the angle of attack can then be plotted. For clarity only one combination of flap angle and velocity is plotted, shown in fig. 4.8.

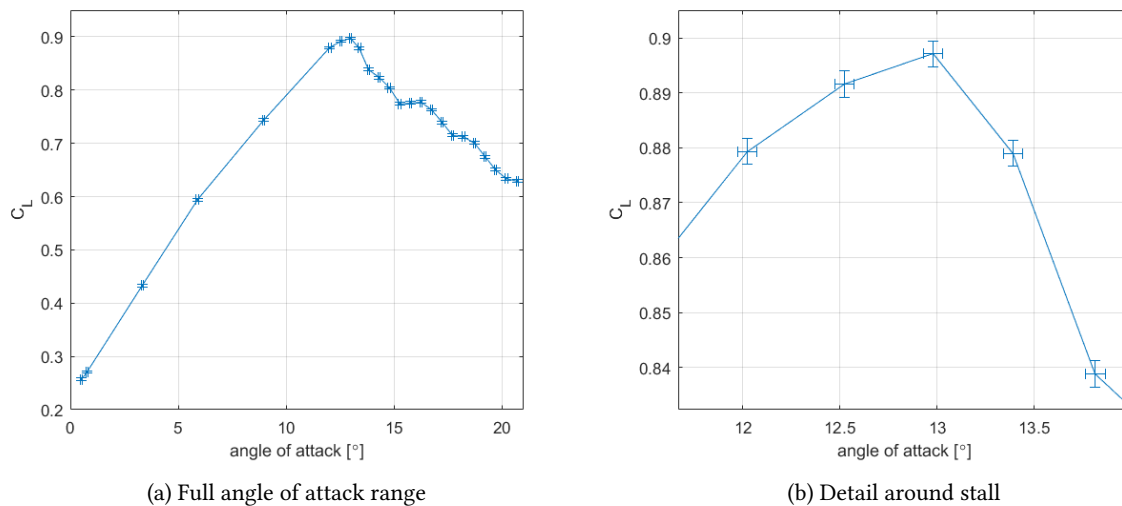


Figure 4.8: Angle of attack and lift coefficient uncertainty for a flap angle of 5° and a freestream velocity of 12.5 m/s

4.4. Tufts

In order to extract data from tufts they can be recorded or photographed. For the reported research it was chosen to record the tuft behaviour for approximately 20 seconds for each flow case. This means that per flow case

several hundred images are recorded. The video clips also help with indicating unsteady or transitional flow behaviour. However to express the findings of the video clips in representative images some data processing is required.

The video clip is first separated in grey scale images, a sample image is shown in fig. 4.9a. Single images do not represent the behaviour that can be observed in the recording and furthermore the contrast is poor which results in tufts that are hardly visible. For the method to process the images it is required to reduce the background as much as possible while maintaining the tufts unsteady behaviour. One of the problems to overcome is the small changes in background illumination over time during a single recording. This is solved by taking a single image and subtracting the next image. In between consecutive images the illumination barely changes, but the tufts do change. The resulting image after subtraction has a much reduced background intensity while maintaining the variations in tuft position. If a tuft would remain in the exact same position in two consecutive images it would also be subtracted and disappear, the subtraction thus shows only variations between images. The images resulting from the subtraction are then in a first stage added to each other in groups of 10 images. The first grouping holds most the flow behaviour that occurs in 10 consecutive images (for recordings at 30 fps this corresponds to approximately 0.33 seconds) at high contrast, as shown in fig. 4.9b. The first grouping of images has to be kept small enough to have a relatively high contrast and a low unsteadiness as the grouping is repeated. The best contrast is achieved between only two consecutive images, but this limits the information contained in the resulting image in terms of unsteadiness over the full duration of the recording. The second round of grouping uses the images such as shown in fig. 4.9b. The amount of images used for the second round of grouping is lower than for the first round, also to keep the contrast high and the unsteadiness relatively low such as shown in fig. 4.9c. When a second group of images is combined with already a high level of unsteady behaviour, the unsteady behaviour will be eliminated by the subtraction of consecutive images. A final round of grouping images results in an image such as shown in fig. 4.9d. The contrast is high and the tuft unsteadiness is clearly visible allowing for more in depth analysis than single images.

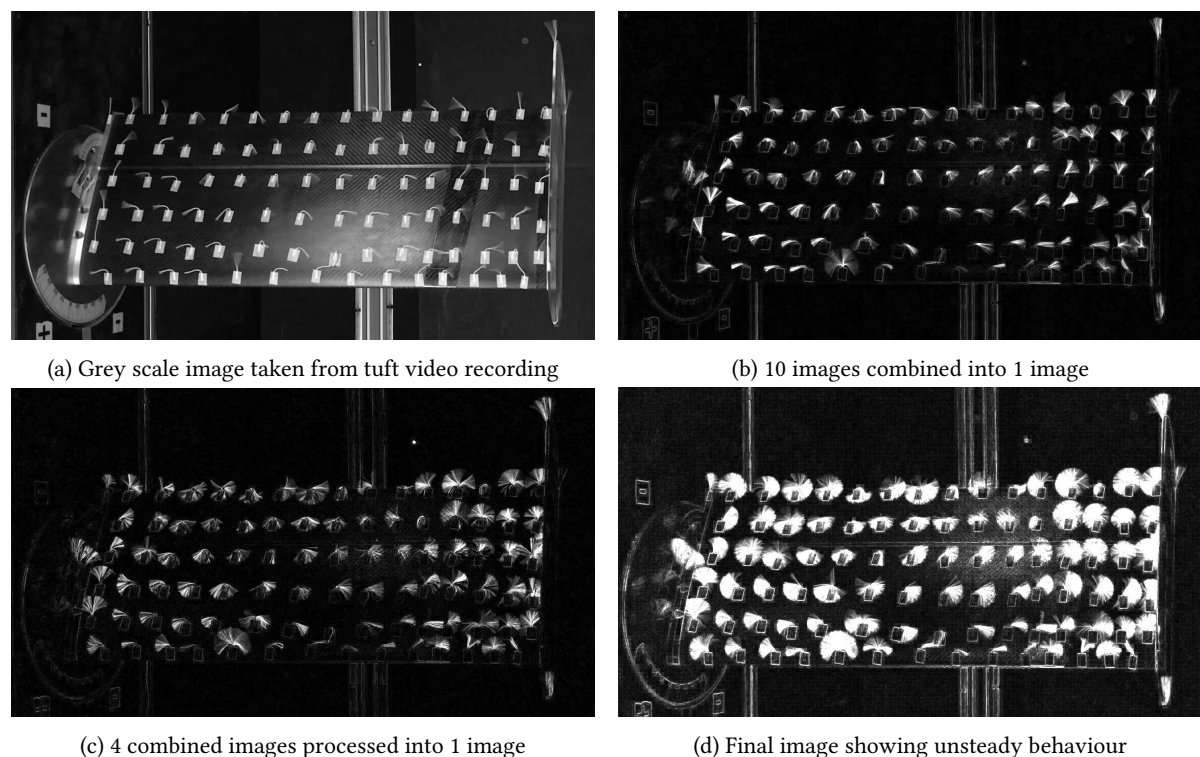


Figure 4.9: Tuft image processing

4.5. Stereoscopic Particle Image Velocimetry

After the processing of the raw PIV images the vector fields are exported for all the instantaneous images. The vector fields can be used to quantify aspects of stall cells. One of the most characteristic features of a stall

cell are the spiral nodes with corresponding stall cell vortices coming from the suction surface and trailing downstream, such as described in section 2.2.2. The location of the SPIV measurements allows to observe these vortices at the trailing edge while they trail downstream perpendicular to the PIV laser sheet. In fig. 4.10 a result is shown of the cross plane SPIV near the trailing edge of the wing. The vertical black line indicates the approximate position of the trailing edge. The two stall cell vortices can be identified by the in plane vectors showing the circulating flow. In order to maximise the information about the stall cell vortices that can be obtained, the analysis has been carried out on the instantaneous images. This allows to judge the unsteady behaviour and determine more information about the average and the relevant standard deviation of specific quantities under investigation.

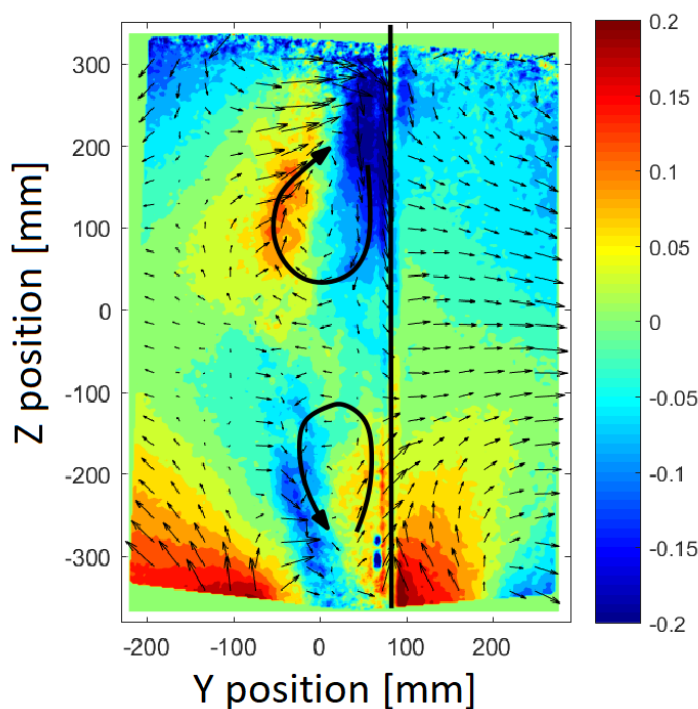


Figure 4.10: Indication of stall cell vortices and the trailing edge (vertical black line) in SPIV result showing the spanwise velocity normalised by the freestream velocity

4.5.1. Conventional Vortex Detection

Several vortex detection methods exist that are based on a 2D velocity field and the derivatives thereof. Some well known methods are: vorticity, swirling strength, Q-criterion, Δ -criterion and λ_2 -criterion. Since the velocity gradient plays an important role in the determination of these vortex identification methods the level of turbulence and measurements noise present in the instantaneous images, such as shown in fig. 4.11a, can pose a problem. In order to apply these vortex identification methods the data has to be smoothed to avoid extreme velocity gradients. The smoothing is done with a moving average of 10 pixels and results in the image such as shown by fig. 4.11b. The value of 10 pixels is selected to not smooth out the stall cell vortices but eliminate most irrelevant turbulent and noisy data. As can be seen, the visual identification of the stall cell vortices becomes easier.

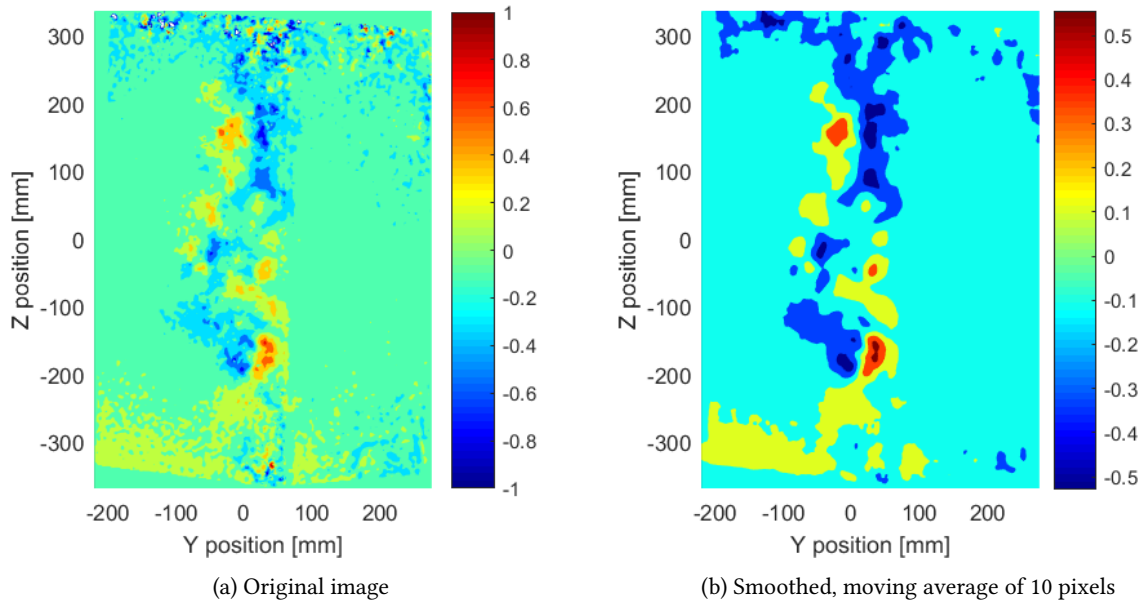


Figure 4.11: Instantaneous image showing the normalised spanwise velocity for $\alpha=14.54^\circ$, $\beta=0^\circ$, $Re=2.1 \cdot 10^5$

First the vorticity of the velocity field is calculated, shown in fig. 4.12. Clearly many vortex cores are found within the wake of the stall cell. One out of the two stall cells is easily identified at a Z coordinate of -175 mm approximately. The other stall cell vortex is more difficult to identify as it is still surrounded by many areas with a similar vorticity. The second method which is evaluated is using the swirling strength, shown in fig. 4.13. It can be seen that there is less noise in the resulting images, however still the identification of the vortex with a negative swirling strength value remains difficult.

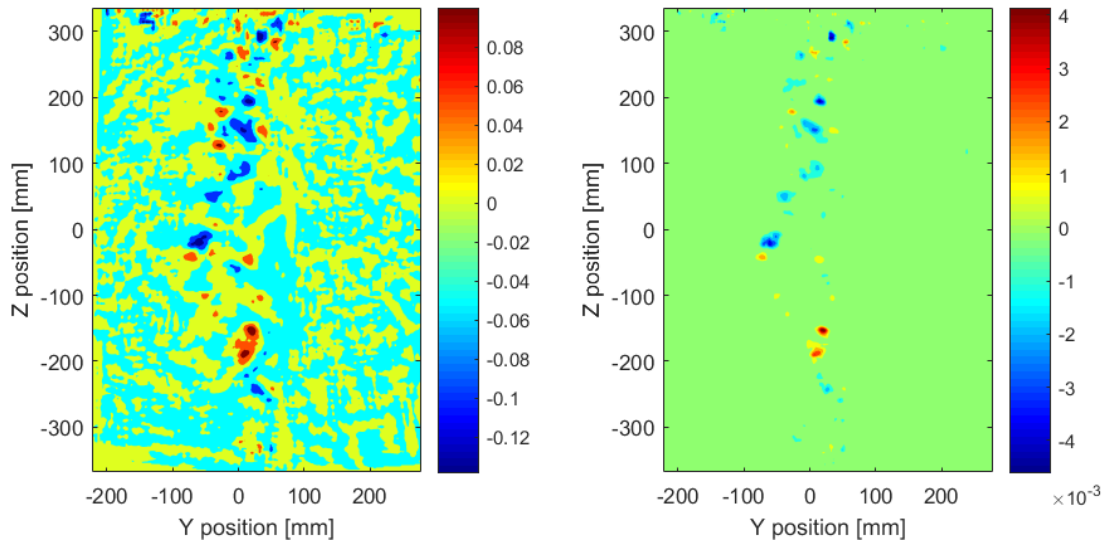


Figure 4.12: Vorticity for instantaneous image for $\alpha=14.54^\circ$, $\beta=0^\circ$, $Re=2.1 \cdot 10^5$

Figure 4.13: Swirling strength for instantaneous image for $\alpha=14.54^\circ$, $\beta=0^\circ$, $Re=2.1 \cdot 10^5$

The next method for vortex identification that is tested is the Q-criterion, shown in fig. 4.14. It can be seen that this produces an image similar to the swirling strength, albeit without the identification of the direction of rotation. The Δ -criterion which is related to the Q-criterion is shown in fig. 4.15. This image appears as a filtered version of the Q-criterion. Only the largest Q-criterion values are still visible and are reduced to a small dot.

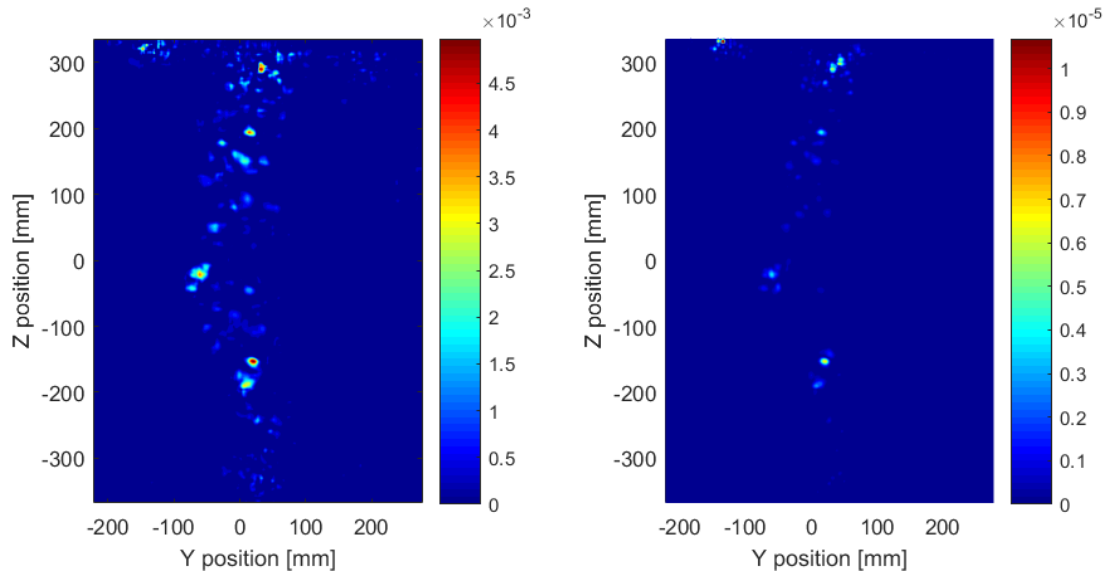


Figure 4.14: Q-criterion for instantaneous image for $\alpha=14.54^\circ$, $\beta=0^\circ$, $Re=2.1 \cdot 10^5$, Figure 4.15: Δ -criterion for instantaneous image for $\alpha=14.54^\circ$, $\beta=0^\circ$, $Re=2.1 \cdot 10^5$

Lastly the λ_2 -criterion is shown in fig. 4.16. It can be seen that the results produced are similar to the Q-criterion results. This shows a reasonable prediction of the vortex cores, but does not conclusively indicate the stall cell vortex cores.

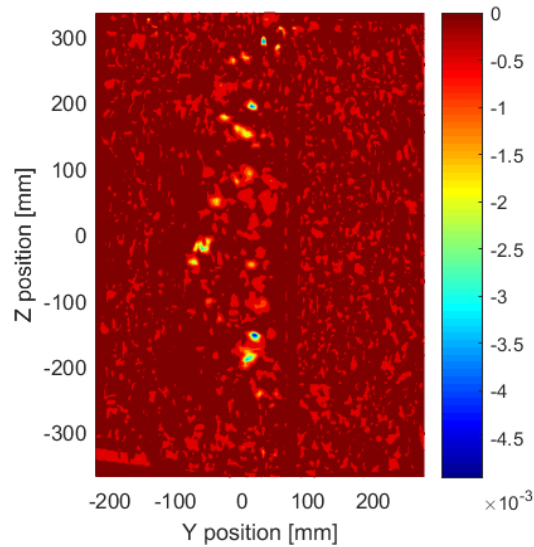


Figure 4.16: λ_2 -criterion for instantaneous image for $\alpha=14.54^\circ$, $\beta=0^\circ$, $Re=2.1 \cdot 10^5$

From this analysis of traditional vortex core identification methods it is concluded that they do not allow for straight forward identification of the stall cell vortices. The vorticity and swirling strength take into account the rotational direction of the vortex which helps with the identification, but both still show multiple irrelevant vortices. The Q-, Δ - and λ_2 -criterion identify vortex cores without displaying the relevant rotational direction. Furthermore these criteria show results that are very similar to the swirling strength. When using any of the vortex core identification methods the swirling strength would be the preferred method. However the main drawback of these methods is that better results can be obtained but require further filtering or manual intervention specific to each case that has been tested separately. However it is desired to have an automatic method that is consistent for all cases that are investigated. For this reason it has been chosen to create a vortex identification algorithm which relies more on the visual identification of large scale vortical structures based

on the spanwise velocity field.

4.5.2. Vortex Identification By Correlation

The spanwise velocity component shows the velocity induced by the vortices. Each vortex will induce a spanwise flow component near the airfoil surface towards the centre of the stall cell. On the opposite side of the vortex core an induced flow going away from the stall cell centre can be observed.

The influence of vortices on the surrounding flow is well known and can be modelled. This allows for a linearisation of the flow field in which the influence of the vortices can be seen as superimposed on a flowfield in which no stall cell is present.

A flowfield is characterised by the three velocity components of the flow at any position. The addition of vortices in a flowfield translates into addition of the induced velocity components of the vortex. Vortices are characterised by an angular velocity and the lack of a radial velocity component. The angular velocity that is induced by the vortex core is a function of the radius between the core and the desired location for vortex induced velocity evaluation.

Multiple models for vortices exist and have been used and documented in literature extensively. The induced velocity of four different models is shown in fig. 4.17. The first model is a mathematical derivation from potential (irrotational) flow in which the angular momentum is constant. The second model is the forced vortex in which all particles have the same angular velocity. Both these vortices do not mimic vortices as have been observed.

This gives rise to the third vortex model called the Rankine vortex. This is a composite model which corresponds to a simplistic representation of a vortex in a viscous fluid. The vortex core is represented by a forced vortex and the outer part is a free vortex.

Finally a more elegant model for a vortex in a viscous fluid has been given by the Lamb-Oseen vortex. It gives similar behaviour as the Rankine vortex but captures this in a single, continuous, equation.

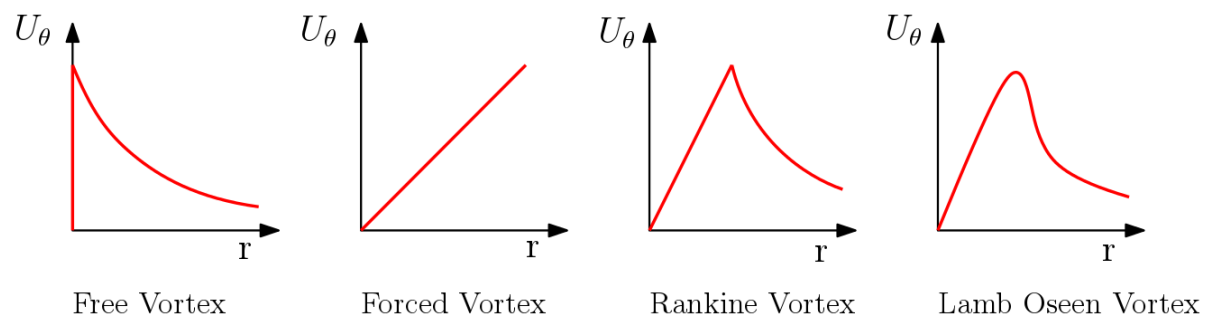


Figure 4.17: Different models for vortices

Although all four models represent vortices, only the Rankine and Lamb-Oseen vortex models represent vortices in viscous fluids. The stall cell vortices that are being observed with the SPIV measurements clearly correspond to vortices in viscous fluids. This can be observed by a induced velocity which is low near the centre of the vortex and increases towards a maximum at a small distance from the vortex centre. Beyond this radius where the induced velocity is maximal, the induced velocity decreases again, this can be observed in fig. 4.10. Both the Rankine vortex and Lamb-Oseen vortex models represent this behaviour well.

As the vortex models correspond well with the results obtained from SPIV it is possible to fit the model to the experimental results. The Rankine vortex model is chosen for its simplicity. The Rankine vortex is determined by the core radius and the circulation. The magnitude of the induced velocity by this vortex is in turn determined by the distance from the vortex core to the point of interest, keeping in mind that the direction of the velocity has to be consistent with the rotational direction of the vortex. The formula for the induced velocity is shown in eq. (4.13), where R represents the core radius, Γ the circulation and r the radial distance from the centre of the vortex. An example of the induced velocity in spanwise direction due to two vortices is shown in fig. 4.18.

This vortex model can then be used to create fictitious flow fields that can be compared to the results from SPIV. From which the parameters of the vortex are determined.

$$u_{\theta}(r) = \begin{cases} \Gamma r / (2\pi R^2) & r \leq R \\ \Gamma / (2\pi r) & r > R \end{cases} \quad (4.13)$$

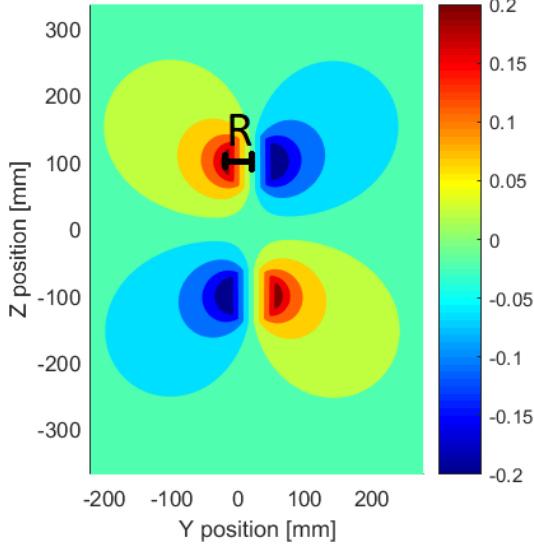


Figure 4.18: Normalised spanwise velocity induced by Rankine vortices

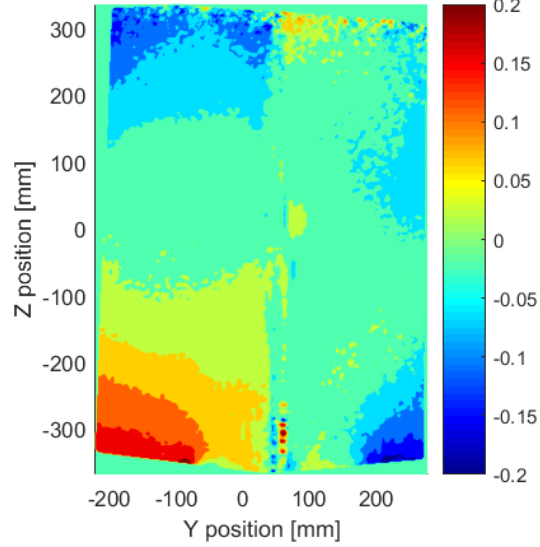


Figure 4.19: Normalised spanwise velocity for $\alpha = 12.68^\circ$, $\beta = 0^\circ$, $Re = 2.1 \cdot 10^5$

The process of matching two flow fields is focused on creating a fictitious flow field by using a flow field without vortices and adding the induced velocity caused by Rankine vortices. The SPIV experiments also covered cases which do not show stall cells, this is predominantly at angles of attack lower than stall. Such a flow field presents a good basis on which the influence of Rankine vortices can be superimposed. The base flow field needs to match the background flow field of the SPIV cases with stall cells as well as possible to keep the influence of the Rankine vortices in the fictitious flow field high for the error that is minimised in the optimisation that will follow. For these reasons the base flow field on which the Rankine vortices are superimposed needs to be at a high lift condition in order to have a base flow field that matches the ones with stall cells well. In order to keep the optimisation method consistent only one base flow field will be used for the analysis of all cases. This implies that one setting for the optimisation is used for all the cases and only the Rankine vortex parameters are allowed to vary. The base case that is used is the average solution of the configuration with flap angle zero degrees, angle of attack 12.68° and Reynolds number $2.1 \cdot 10^5$, shown in fig. 4.19. This cases minimises the overall error that is minimised in the optimisation. It was not possible to subtract the background of the PIV images as it is not known how the stall cells influence the background.

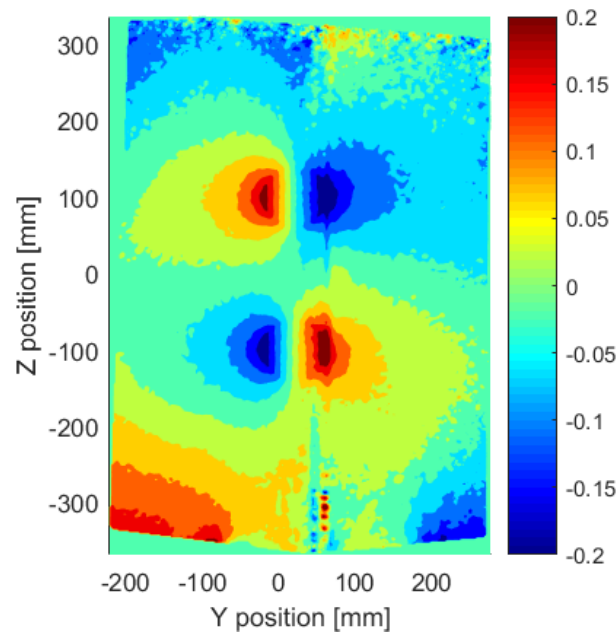


Figure 4.20: Combination of base flow field and vortex induced flow field

With an appropriate base case selected the influence of the Rankine vortices can be added. It is assumed that stall cells have two counter rotating vortices. Furthermore the vortices are assumed to have a orientation such that they cause an upwash near the centre of the stall cell. A summation of the base flow field from fig. 4.19 and the vortex induced flow field from fig. 4.18 is shown in fig. 4.20. In order to have a good match between the fictitious and the SPIV flow field the vortices have certain parameters that can be tuned. For each stall cell vortex the following parameters are used: the core radius, the circulation, the spanwise position and the distance from the airfoil surface. With two vortices this results in eight parameters to be optimised. Due to the "curse of dimensionality" it is not possible to test all possibilities and an optimisation routine is thus required.

For the optimisation the most important aspect is a good definition of the objective function. With the goal of matching two flow fields of which one is given, the objective function needs to create and evaluate a fictitious flow field. It has to be kept in mind that the fictitious flow field and the SPIV result only have good matching streamwise velocity components. The two other velocity components are not comparable since the base case is a situation before stall while the SPIV result to be matched is one with stall cells. When the stall cell vortices are introduced in the base case, they affect the span wise velocity. The other vortices that are characteristic to stall cells (separation line vortex and trailing edge vortex) are ignored, and so is the influence they have on the flow field. Since they are assumed to have no influence on the spanwise component of the flow, the optimisation of the flow field with stall cell vortices is still valid for the spanwise velocity component.

The objective function starts with the input which are the parameters for the vortices and a base flow field without stall cells. In order to not manually influence the results, the base case that is used is such as displayed in fig. 4.19 and maintained for all optimisations. Then the optimisation routine suggests a set of parameters, the objective function then creates the corresponding flow field consisting of the base flow field with the induced velocities caused by the vortices added. In order to compare the SPIV flow field and the fictitious flow field, the two frames need to be lined up. During testing the trailing edge changes position in the FOV of the cameras due to angle of attack and flap angle changes. By lining up the trailing edges of the fictitious flow field and the PIV result they become comparable. A crop of the full frame is used that focuses on the stall cell area. This reduces the influence of the surrounding flow field which is not of interest. The cropped frame that is used for comparison is shifted according to the difference in trailing edge position between the base flow field and the SPIV flow field. Finally in cases with a high flap deflection and high angle of attack, the SPIV results suffer from some reflections that introduce small areas that have higher or lower values than would be true. These outliers are replaced with respectively high or low values within a range that is considered feasible. For the cases with a flap angle of ten degrees this is for example plus or minus 0.6 times the freestream velocity.

Finally the normalised spanwise velocity components from the SPIV results and the fictitious flow field are compared for each data point in the frame. The sum of the squared errors is used as the output of the objective function. The optimisation attempts to minimise this value.

For the optimisation itself "fmincon" from MATLAB is used with the sequential quadratic programming (sqp) method, this is a constraint non linear optimisation algorithm. This function is easy to use as it only requires an initial guess, constraints and an objective function. The objective function has been discussed already, the constraints are based on knowledge of stall cells. As mentioned earlier, the rotation of the vortices and the location can be somewhat estimated. This leads to bounds that allow for any stall cell configuration that would still classify as a stall cell. Within these bounds, a reasonable guess can be made for an initial condition that creates a feasible fictitious stall cell.

The parametric vector that is used for the optimisation is constructed as shown by eq. (4.14). Where the numbers 1 and 2 represent the two different vortices, R represents the core radius, c the circulation strength and y and z the position of the vortices.

$$X = [R1, R2, y1, z1, c1, y2, z2, c2] \quad (4.14)$$

The upper bound (*UB*), lower bound (*LB*) and initial condition (*X0*) are as shown below.

$$\begin{aligned} UB &= [50, 50, 50, 350, 0, 50, 50, 1500] \\ LB &= [10, 10, -125, -50, -1200, -125, -350, 0] \\ X0 &= [40, 40, -50, 200, -500, -50, -200, 600] \end{aligned} \quad (4.15)$$

The radii and locations are in millimetres. The unit of the circulation for the input is $(mm \cdot m)/s$, which results in a velocity in m/s which is compatible with the results from the SPIV. The location is measured relative to the axis centre of the SPIV frame determined by the calibration, this is approximately at the midspan near the trailing edge with angle of attack and flap angle equal to zero. The optimisation runs until the relative changes in the parameter vector are less than a threshold value of 0.01 and the parameter vector is within the constraints. When the optimisation is stopped it outputs the parameter vector which satisfies the optimisation and the final value of the objective function, being the error. The method of matching a vortex model to an observed vortex to obtain parametric data is not new. More detailed approaches of this method can be found in literature and include multiple corrections for high accuracy [41]. Due to the high level of turbulence in the results that will be analysed here the vortices are not always well defined, thereby requiring a robust method. Keeping the vortex matching algorithm simple in terms of limited optimisation parameters allows for an analysis of when the method performs well and when it fails. For this method of vortex identification it has to be kept in mind that the circulation that results from the optimisation is not representative for the circulation in the entire wake. The optimisation ignores all the circulation in the wake and only matches the flow velocity field by creating the Rankine vortices. Due to the high level of turbulence, part of the circulation that is present in the smaller turbulent scales is not captured. Furthermore, this effect is aggravated at higher Reynolds numbers. The circulation that is calculated is representative for the largest scales present in the flow.

4.5.3. Optimisation Validation

The optimisation that is discussed has been verified during the construction and once it is finished. This has been done by plotting a single vortex or two combined, such as has been shown in fig. 4.18 and fig. 4.20. Plotting these elements separately allowed to verify that the created flow fields match the input parameters. For the optimisation to be of practical use, it has to be validated. The validation serves to indicate that the result of the optimisation corresponds accurately to the input that it is intended to match.

Since no results are available of which all the parameters that can be optimised for are known, inputs are created for the validation. These inputs test two important aspects of the optimisation. As the optimisation has only one initial condition, the optimisation should have a low sensitivity to the initial condition. Unfortunately "fmincon" with the sqp method is known to be sensitive to the initial condition. Still this method is chosen to be used as it is a commonly used method that can easily be replicated by others. It is thus important to check if the optimisation can cope with the highly unsteady stall cell vortex positioning and strength in the input. The second aspect that has been tested is the ability to deal with noise in the input. The high level of turbulence

in the wake of the stalled wing which may act to mask the clear contours of induced velocity by the stall cell vortices.

Testing the sensitivity to the initial condition is done by creating an input file with known parameters, that differ substantially from the initial condition. The initial condition has been shown in eq. (4.15), as a first attempt the initial condition values have been halved to create the input. The input values are thus as shown by eq. (4.16). In eq. (4.16) also the output of the optimisation is shown. Deviations from the input values as retrieved by the optimisation are mostly less than 1% of the input value.

$$\begin{aligned} \text{Input} &= [20.00, 20.00, -25.00, 100.00, -250.00, -25.00, -200.00, 300.00] \\ \text{Output} &= [19.66, 19.82, -25.01, 100.12, -247.27, -24.85, -199.76, 300.14] \end{aligned} \quad (4.16)$$

A more extreme input case is constructed by taking alternating upper and lower bound values for the input parameters. The respective input and output values are shown by eq. (4.17). The optimisation does not return results which correspond closely to the input. The two initial parameters are the core radius of the vortices, these are not retrieved well at all, fortunately these are not of great importance. Next it can be seen that the y coordinates determining the distance from the trailing edge in the planar view, are captured well. The z coordinates of the stall cell vortices are an indication of the width of the stall cell and play an important role. The validation shows that the z coordinate is not captured accurately. The input has a z spacing of 700 mm between the stall cells, the output reports a spacing of 504.27 mm. Furthermore, the strength of the stall cells is poorly captured by the optimisation by outputting values that are less than half of what was put in.

$$\begin{aligned} \text{Input} &= [10.00, 50.00, -125.00, 350.00, -1200.00, 50.00, -350.00, 1500.00] \\ \text{Output} &= [50.00, 32.73, -125.00, 196.80, -446.70, 47.94, -307.47, 590.45] \end{aligned} \quad (4.17)$$

This second validation is shown by fig. 4.21. Though the optimisation still results in an output which is similar to the input, the images do not match. The main reason for the optimisation failing in this case is that the input only shows limited parts of the influence of the stall cell vortices. When the stall cell vortices are located on the edge of the frame the optimisation has more difficulty in matching this flow scenario.

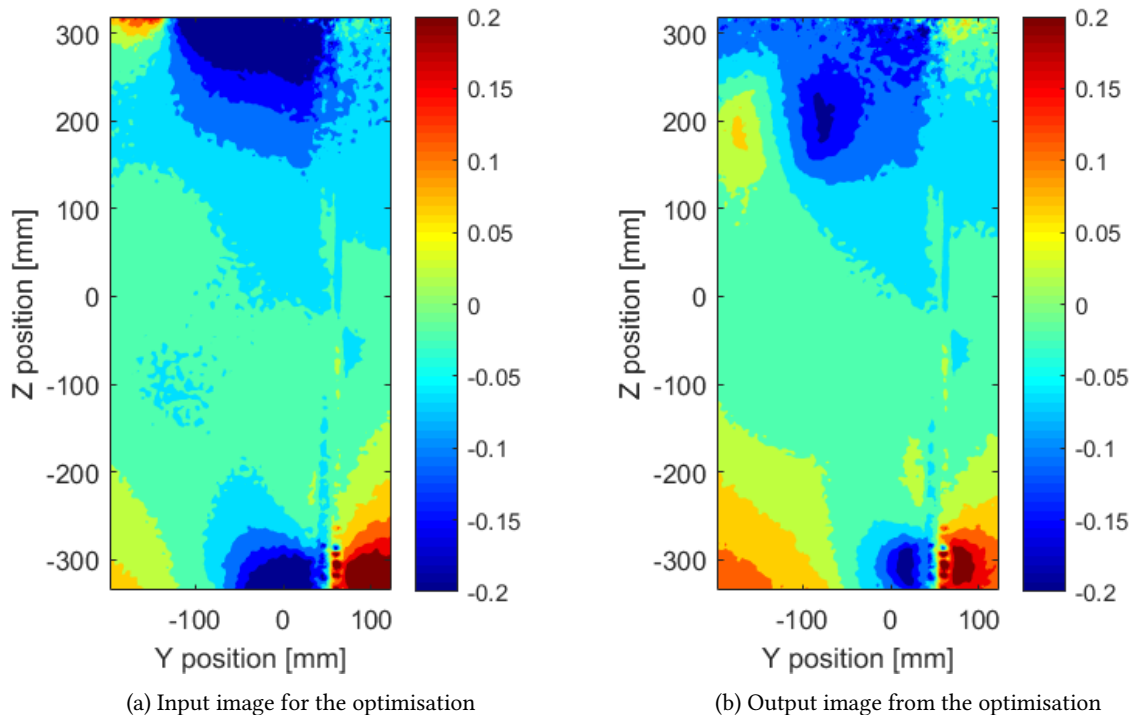


Figure 4.21: Result of the optimisation validation for initial condition sensitivity

After the evaluation of the impact of the initial condition the sensitivity to noise was investigated. Again an input file is created for which the parameters are known, with the goal to have the optimisation retrieve these

parameters. It has been shown that certain aspects such as the initial condition and the positioning of the stall cells has an influence. In order to investigate the influence of the turbulence the input case should not be the same as the initial condition as then the optimisation will not be tested in a representative manner. Therefore it has been decided to use the same input parameters as shown by eq. (4.16). The noise that is added to the image is generated randomly from a normal distribution. The normal distribution has a standard deviation of 0.067, corresponding to one third of the bounds of the normalised spanwise velocity. In fig. 4.22 both the original input image and the input image with added noise are shown. With the addition of the noise the location of the stall cell vortices is still recognisable but by visual inspection no accurate estimate can be made regarding the core radius or strength.

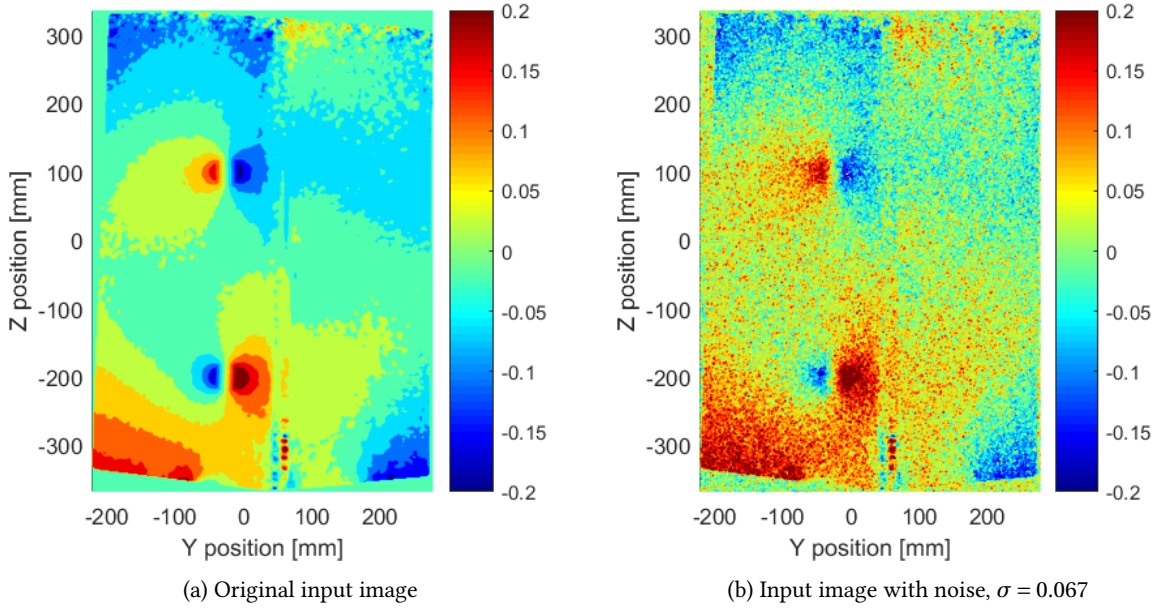


Figure 4.22: Clean input and input with added normal distributed noise for noise sensitivity evaluation

This image with the noise added is inserted in the optimisation routine and the parameters such as shown in eq. (4.18) are the result. It is clear from comparison with the input that this level of noise poses no challenge for the optimisation.

$$\begin{aligned} \text{Input} &= [20.00, 20.00, -25.00, 100.00, -250.00, -25.00, -200.00, 300.00] \\ \text{Output} &= [20.43, 19.74, -24.85, 100.38, -258.49, -24.47, -199.17, 295.31] \end{aligned} \quad (4.18)$$

A more representative noise needs to be of a larger spatial scale than each pixel individually. For this reason a level of Brownian noise is added to the original input image. The noise is intended to mimic the influence of turbulence by having more energy distributed over lower frequencies compared to white noise. Which is equivalent to larger spatial scales of turbulence. The scales of the turbulence have been visually estimated to be in a range which is feasible for experimental results. The Brownian noise used for this is scaled to have a standard deviation of approximately 0.070, the resulting noise is shown in fig. 4.23a. Again the same input parameters are used, described in eq. (4.18) and shown in fig. 4.22a. Combining the noise and the clean input results in fig. 4.23b, which serves as the input for the optimisation. The result of the optimisation is shown by fig. 4.23c. The parameters that are obtained by the optimisation are shown in eq. (4.19). Again it can be observed that the noise mimicking turbulence has little to no influence on the optimisation.

$$\begin{aligned} \text{Input} &= [20.00, 20.00, -25.00, 100.00, -250.00, -25.00, -200.00, 300.00] \\ \text{Output} &= [20.52, 19.73, -25.65, 100.40, -255.41, -25.04, -201.02, 288.88] \end{aligned} \quad (4.19)$$

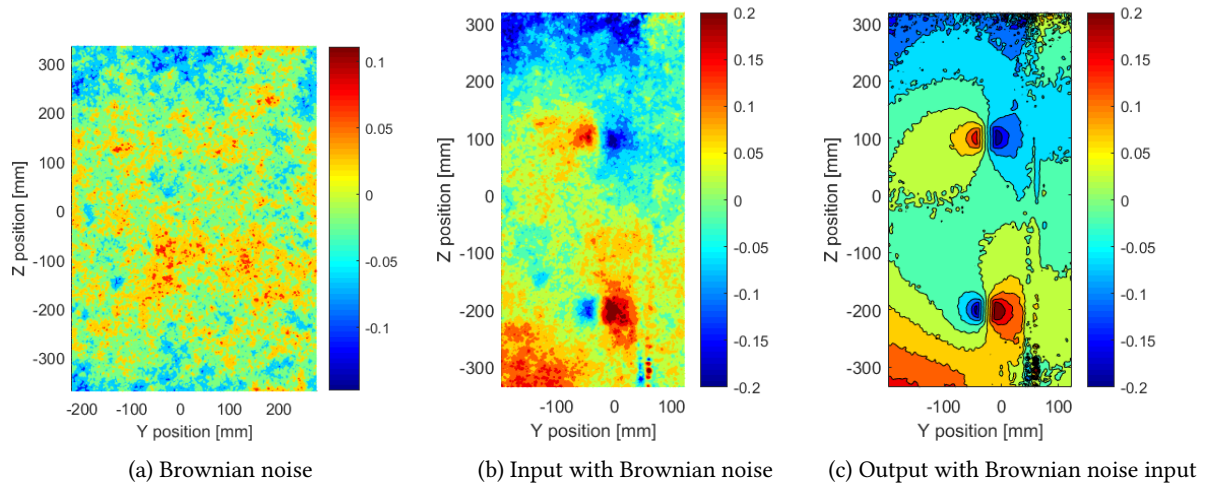


Figure 4.23: Evaluation of the influence of Brownian noise on the input

The validation that has been discussed concerned the initial condition and the level of turbulence and noise sensitivity of the optimisation. It has been shown that changes in initial condition can effect the capability of the optimisation to reach the correct result, the location of the vortex position appears most critical. It also has been shown that the introduction of turbulence and noise has only a very small influence and does not hinder the optimisation in finding the correct parameters. When the stall cell vortices are located very close to the edge of the frame, part of the stall cell vortex influence is not displayed, this causes problems for the optimisation leading to unrepresentative solutions. In future work it would be recommended to resolve this problem by for example identifying if a stall cell vortex is near the edge of the frame. In addition it would be beneficial to have a variable initial condition. Choosing for example a genetic algorithm which is initially based on random parameter evaluation to optimise the initial condition before running the "fmincon" optimisation, can lead to higher accuracy in cases that are further removed from the fixed initial condition that is used now. As a good optimisation for the vortex identification is a whole study field in itself it is chosen to keep things simple and work with the algorithm such as has been validated here. Furthermore it can be mentioned that a bigger problem than the identification of the vortices is detection of the absence of vortices. The instantaneous images that are analysed with the optimisation algorithm do not always show vortices that are indicative of a stall cell. By visual inspection of the instantaneous images it is estimated that approximately 20% of those images do not contain stall cell vortices. This percentage is approximately consistent for multiple flow cases. Due to the consistency of the amount of cases without stall cell vortices and in order to minimise manual influence, these cases are included in the statistical analysis of the results. This introduces an error for the average and the standard deviation of the results from the vortex fitting optimisation, this includes the circulation, radius and location.

5

Results

In this chapter the results of the experiments will be presented with the relevant discussions. First the preliminary airfoil shape experiments will be discussed in section 5.1. Next experimental results based on the preliminary conclusions are discussed in section 5.2.

5.1. Identification of Airfoil Shape Influence on Stall Cell Formation

In order to get familiar with the stall behaviour of the NACA 0012 wing flow visualisation experiments have been conducted. The NACA 0012 wing results are compared to results with a NACA 0015 wing from Dell'Orso and Amitay (2018) and a NTUA camber airfoil wing from Manolesos et al. (2014). The experiments that have been performed included tuft surface flow visualisation and turbulence intensity measurements. The results of these experiments are presented in section 5.1.1 and section 5.1.2, followed by the preliminary conclusions from these results in section 5.1.3.

5.1.1. Full Wing Tufts

The first experiment that has been performed is using tufts to identify the flow behaviour for the stalled NACA 0012 wing with an aspect ratio of 5.2. In order to gain insight in the parameters that influence stall cell behaviour, three parameters are varied. By varying the angle of attack, the Reynolds number and the flap angle independently a total of 90 flow cases have been investigated. Each flow case has been recorded for approximately 20 seconds and processed according to the method described in section 4.4. The angle of attack progresses in steps of 1.4° , this unconventional step size is due to a faulty stepper motor connection at the time of testing and has no further influence on the data. The Reynolds number is calculated with a kinematic viscosity of $1.46 \cdot 10^{-5} \text{ m}^2/\text{s}$, corresponding to an air temperature of approximately 15° , a chord length of 0.3 m and a velocity ranging from 5 to 25 m/s in steps of 5 m/s. The resulting parameter values are shown in table 5.1.

α	$[\circ]$	11.4	12.8	14.2	15.6	17.0	18.5
$\text{Re} \cdot 10^5$	$[-]$	1.0	2.1	3.1	4.1	5.1	
β	$[\circ]$	0	5	10			

Table 5.1: Parameter values for AR 5.2 wing tuft experiment

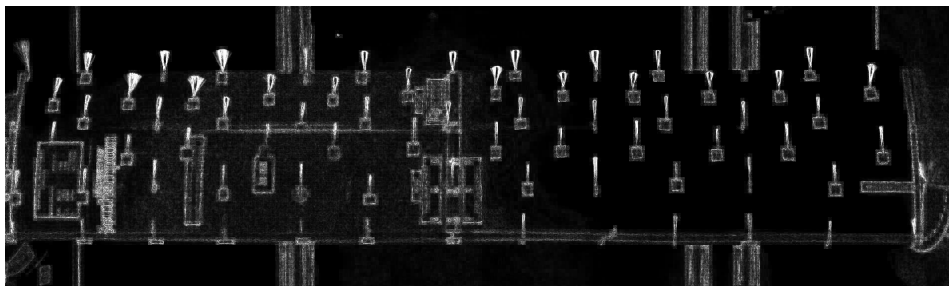
Tufts can only provide qualitative information regarding the flow. In this experiment the tufts are used to distinguish between attached flow, separated flow and stall cells. These three flow categories are illustrated in fig. 5.1, in each of the figures the leading edge is at the bottom of the image and the trailing edge near the top.

In fig. 5.1a the flow is attached to the wing, the tufts are aligned with the flow. The tufts near the leading edge are hardly visible, this is an intentional consequence of the processing to indicate the steady behaviour of these tufts. The tufts closer to the trailing edge exhibit slightly more unsteady behaviour due to the developing turbulence along the chord.

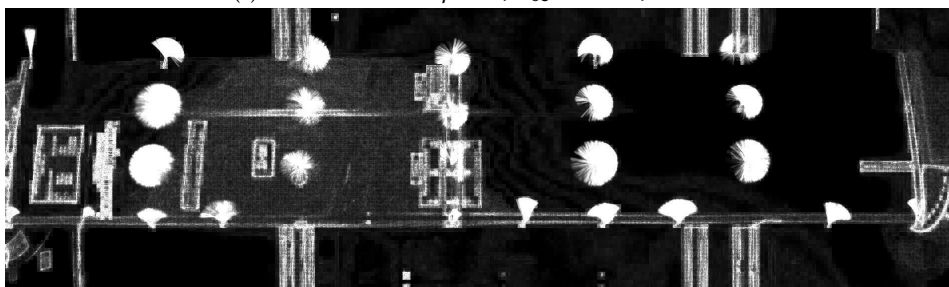
The surface flow visualisation in fig. 5.1b has less tufts but this does not impede the analysis of the observation. The tufts indicate full span separation of the flow, this is recognised by tufts displaying a nearly full circle

over the entire span. The full circle created by the tufts in the image indicates that the tufts have no preferred position and are flapping around randomly. This is characteristic for fully separated flow.

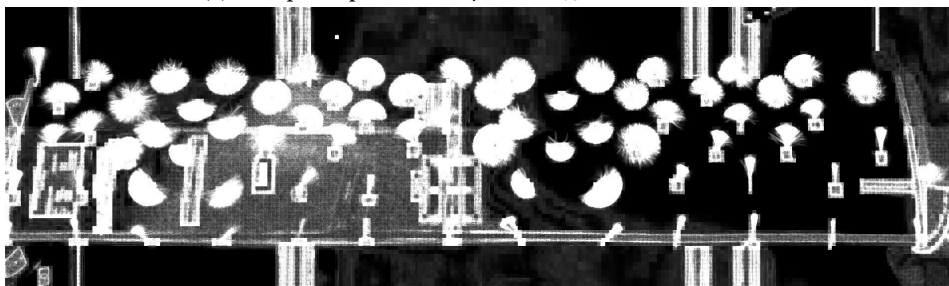
The tufts in fig. 5.1c show a pattern of two stall cells. This pattern can be easily recognised from a number of features. One of the most prominent features is tufts that have a predominantly upstream direction. Tufts pointing upstream indicate the centre of a stall cell while the unsteady tufts on either side of the centre indicate the direction of the flow within the stall cell. Next to and in between the stall cells relatively steady tufts can be observed, indicating a region of attached flow. In fig. 5.1d a diagram of the stall cells and regions of attached flow is shown overlaid on the processed image.



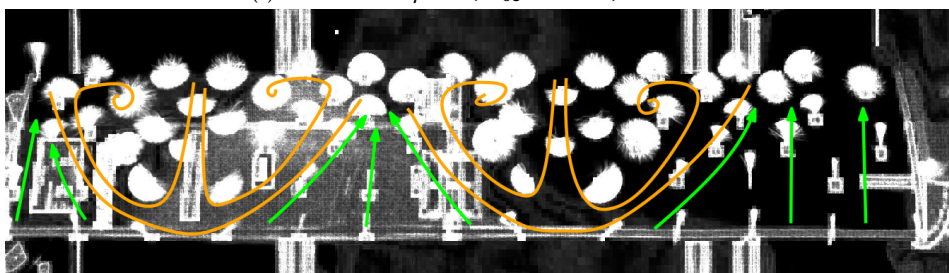
(a) Attached flow for $\beta = 5^\circ$, $U_\infty = 25$ m/s, $\alpha = 5.7^\circ$



(b) Full span separation for $\beta = 0^\circ$, $U_\infty = 5$ m/s, $\alpha = 17.0^\circ$



(c) Stall cells for $\beta = 5^\circ$, $U_\infty = 25$ m/s, $\alpha = 18.5^\circ$



(d) Stall cell diagram for $\beta = 5^\circ$, $U_\infty = 25$ m/s, $\alpha = 18.5^\circ$

Figure 5.1: Possible tuft results for aspect ratio 5.2

The cases such as shown in fig. 5.1 are straight forward and allow for easy identification. However during the process of testing it was already noticed that these flow scenarios are not always clearly present. The stall behaviour of the wing was not binary. In between fully attached flow and stall cells there are transitional stages.

Even when the stall cells start to appear these do not always lock into a single position. The transitional phases and the unsteady behaviour of stall cells complicate the processing of the data. A single image composed of the original recordings can give misleading results if not critically assessed. Two different images are shown in fig. 5.2, each image is constructed from a separate recording of the same parameter case. The images show one half of the wing span. In the left image it can be seen that the flow is almost fully attached over half the span. However the right image shows erratic behaviour at first sight, without more information it could lead to the conclusion that the flow is separated. This is one of the biggest shortcomings of reducing a recording into a single image.

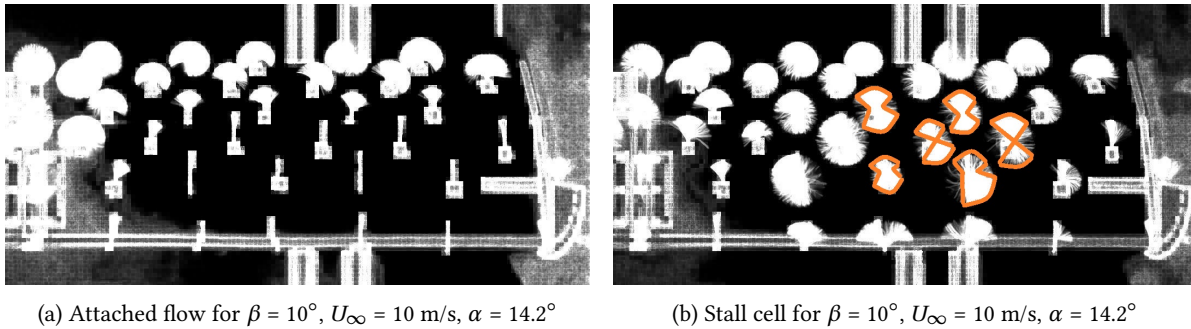


Figure 5.2: Different results for the same parameter case

When the original recording of the right image is considered it can be shown that the resulting image in fig. 5.2b follows from a transitional phase. This transitional phase is characterised by the flow switching between a jostling stall cell and unsteady attached flow. fig. 5.3 shows a series of tuft positions in chronological order for a time frame of approximately two seconds. These images are obtained from the recording which has been processed to create fig. 5.2b and show a similar FOV. With this knowledge in mind, fig. 5.2b can be reexamined to observe certain tufts showing unsteady attached flow and upstream flow at the same location near the centre of the stall cell. This bi-modal behaviour results in tufts that show a bow tie pattern, the clarity of the bow tie pattern depends on both the flow behaviour and the processing method.

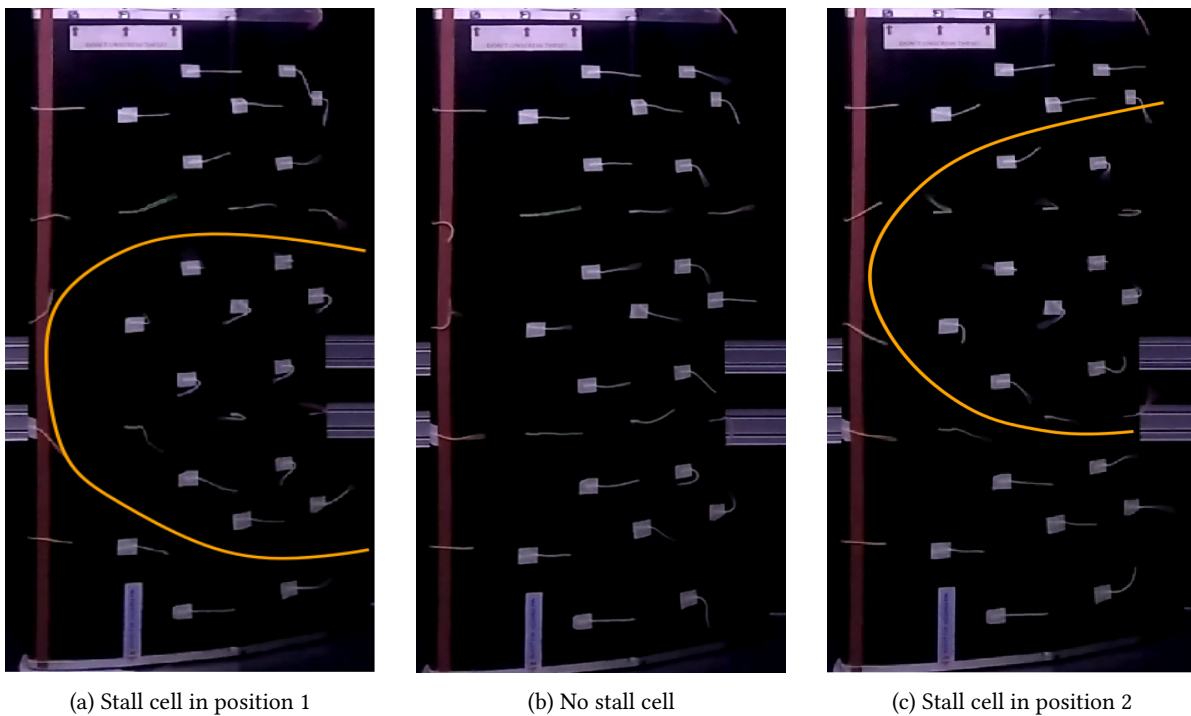


Figure 5.3: Transitional phase and unsteady behaviour shown by tufts in a recording

It is clear that although some information is lost, the method used for the processing of the recordings into images allows for identification of unsteady behaviour. However it is still necessary to review the recordings for cases where the final processed image is inconclusive.

The different flow scenarios that are created are thus not limited to attached flow, full span separation and stall cells. The flow scenarios can also have transitional flow, unsteady attached flow and unsteady stall cells. Furthermore since the wing has an aspect ratio which accommodates up to two stall cells, the location along the wing span also plays a role. The parameterisation of the flow cases allows to observe the progressive changes in flow behaviour. Showing the resulting flow scenarios for all possible combinations of parameters is done by using flow phase diagrams similar to the diagram for a NACA 0015 wing by Dell'Orso and Amitay (2018), shown in fig. 2.8. For each flap angle a different flow phase diagram is created.

Symbol	Meaning																																																																														
/	attached flow	$Re \cdot 10^5$	<table style="width: 100%; border-collapse: collapse;"> <tr> <td style="width: 15%;"></td> <td style="width: 15%;"></td> <td style="width: 15%; text-align: center;">\tilde{t}</td> <td style="width: 15%; text-align: center;">$1 t + \tilde{b}$</td> <td style="width: 15%; text-align: center;">$1 t + \tilde{t} b$</td> <td style="width: 15%;"></td> </tr> <tr> <td style="text-align: center;">1</td> <td style="text-align: center;">1 stall cell</td> <td style="text-align: center;">5.1</td> <td style="text-align: center;">/</td> <td style="text-align: center;">/</td> <td style="text-align: center;">/</td> <td style="text-align: center;">1 t</td> <td style="text-align: center;">1 t + \tilde{b}</td> </tr> <tr> <td style="text-align: center;">2</td> <td style="text-align: center;">2 stall cells</td> <td style="text-align: center;">4.1</td> <td style="text-align: center;">/</td> <td style="text-align: center;">/</td> <td style="text-align: center;">/</td> <td style="text-align: center;">1 t</td> <td style="text-align: center;">1 t + \tilde{b}</td> </tr> <tr> <td style="text-align: center;">s</td> <td style="text-align: center;">separated flow</td> <td style="text-align: center;">3.1</td> <td style="text-align: center;">/</td> <td style="text-align: center;">/</td> <td style="text-align: center;">\tilde{t}</td> <td style="text-align: center;">\tilde{t}</td> <td style="text-align: center;">1 t + \tilde{b}</td> </tr> <tr> <td style="text-align: center;">~</td> <td style="text-align: center;">unsteady/transition</td> <td style="text-align: center;">2.1</td> <td style="text-align: center;">/</td> <td style="text-align: center;">/</td> <td style="text-align: center;">\tilde{t}</td> <td style="text-align: center;">\tilde{t}</td> <td style="text-align: center;">\tilde{t}</td> </tr> <tr> <td style="text-align: center;">t</td> <td style="text-align: center;">top half of the span</td> <td style="text-align: center;">1.0</td> <td style="text-align: center;">/</td> <td style="text-align: center;">/</td> <td style="text-align: center;">\tilde{t}</td> <td style="text-align: center;">\tilde{t}</td> <td style="text-align: center;">\tilde{t}</td> </tr> <tr> <td style="text-align: center;">b</td> <td style="text-align: center;">bottom half of the span</td> <td></td> <td style="text-align: center;">/</td> <td style="text-align: center;">1 m</td> <td style="text-align: center;">\tilde{t}</td> <td style="text-align: center;">f s</td> <td style="text-align: center;">f s</td> </tr> <tr> <td style="text-align: center;">m</td> <td style="text-align: center;">middle of the span</td> <td></td> <td style="text-align: center;">12.8</td> <td style="text-align: center;">14.2</td> <td style="text-align: center;">15.6</td> <td style="text-align: center;">17.0</td> <td style="text-align: center;">18.5</td> <td style="text-align: center;">$\alpha [^\circ]$</td> </tr> <tr> <td style="text-align: center;">f</td> <td style="text-align: center;">full span</td> <td></td> <td colspan="5"></td> <td></td> </tr> </table>							\tilde{t}	$1 t + \tilde{b}$	$1 t + \tilde{t} b$		1	1 stall cell	5.1	/	/	/	1 t	1 t + \tilde{b}	2	2 stall cells	4.1	/	/	/	1 t	1 t + \tilde{b}	s	separated flow	3.1	/	/	\tilde{t}	\tilde{t}	1 t + \tilde{b}	~	unsteady/transition	2.1	/	/	\tilde{t}	\tilde{t}	\tilde{t}	t	top half of the span	1.0	/	/	\tilde{t}	\tilde{t}	\tilde{t}	b	bottom half of the span		/	1 m	\tilde{t}	f s	f s	m	middle of the span		12.8	14.2	15.6	17.0	18.5	$\alpha [^\circ]$	f	full span							
								\tilde{t}	$1 t + \tilde{b}$	$1 t + \tilde{t} b$																																																																					
1	1 stall cell							5.1	/	/	/	1 t	1 t + \tilde{b}																																																																		
2	2 stall cells							4.1	/	/	/	1 t	1 t + \tilde{b}																																																																		
s	separated flow							3.1	/	/	\tilde{t}	\tilde{t}	1 t + \tilde{b}																																																																		
~	unsteady/transition							2.1	/	/	\tilde{t}	\tilde{t}	\tilde{t}																																																																		
t	top half of the span	1.0	/	/	\tilde{t}	\tilde{t}	\tilde{t}																																																																								
b	bottom half of the span		/	1 m	\tilde{t}	f s	f s																																																																								
m	middle of the span		12.8	14.2	15.6	17.0	18.5	$\alpha [^\circ]$																																																																							
f	full span																																																																														

Table 5.2: Legend for flow phase diagram

Table 5.3: Flow phase diagram for full wing with $\beta=0^\circ$

In table 5.3 the flow phase diagram for a flap angle of zero degrees is shown. The legend shown in table 5.2 explains the different flow behaviours that are identified and the possible positions in which they can occur. The tilde serves two purposes, in combination with a stall cell it indicates an unsteady stall cell, in combination with a location it indicates a transitional phase. An unsteady stall cell corresponds to the case such as shown in fig. 5.2b. A transitional phase is defined in this context as a phase in which the flow switches between separation and attached flow without showing characteristics of a stall cell. This transitional phase usually precedes the formation of a, potentially unsteady, stall cell. Summations in the flow diagrams are used to indicate different flow behaviour in different locations. As an example the following description of $\tilde{t} t + \tilde{b}$ should be interpreted as one unsteady stall cell in the top half of the span and a transitional phase at the bottom half of the span.

Stall is known to occur at even very low Reynolds numbers. The lowest Reynolds number that is tested is $1 \cdot 10^5$. For stall in general the expectation is that higher Reynolds numbers will postpone stall to higher angles of attack. With the experiment spanning a Reynolds number range of $4 \cdot 10^5$, this should be visible. However when the possibility of stall cells is introduced things change. Results published by Dell'Orso and Amitay (2018) regarding stall cells are still in line with the consensus for general stall. Results published by Manolesos and Voutsinas (2014) however give an opposite relation where stall cells occur at lower angles of attack for higher Reynolds numbers, such as shown in fig. 3.1. Furthermore the phase diagram can indicate whether stall cells split or merge at higher angles of attack.

These expectations can be compared to the results for a flap angle of zero degrees, shown in table 5.3. It can be seen that for increasing Reynolds numbers the onset of stall, or stall cells in this case, is delayed to higher angles of attack. The diagram also shows how stall cells have a tendency to split at higher angles of attack. This is shown by multiple stall cells being observed at higher angles of attack than single stall cell configurations for a constant Reynolds number. When comparing these results to the phase diagram from Dell'Orso and Amitay (2018) it can be seen that for the NACA 0012 wing under consideration in this experiment the minimum required Reynolds number for stall cells is less, also shown in fig. 5.4. The NACA 0015 wing at 17° angle of attack has a minimum required Reynolds number of approximately $4 \cdot 10^5$ compared to $1.55 \pm 0.55 \cdot 10^5$ for the NACA 0012 wing. It can be noted that the aspect ratio can have an influence such as mentioned by Dell'Orso and Amitay (2018). The aspect ratio used by Dell'Orso and Amitay (2018) is 4, this is smaller than the aspect ratio used for this experiment. The hypothesis formed by Dell'Orso and Amitay (2018) suggests that a smaller aspect ratio requires a higher minimum Reynolds number. Following the preliminary relation that was implied, the aspect ratio influence could cause a NACA 0015 wing with aspect ratio 5.2 to have a minimum

required Reynolds number of approximately $3 \cdot 10^5$. This implies that when the influence of the aspect ratio is taken into account the reduction of 3% airfoil thickness, reduces the minimum required Reynolds number by approximately $1.45 \pm 0.55 \cdot 10^5$. For symmetric NACA 4 digit airfoils this thus implies that the minimum required Reynolds number for stall cells increases with $0.48 \pm 0.18 \cdot 10^5$ per percentage of thickness increase, when assuming a linear relation. In a more general sense, thinner airfoils will likely exhibit stall cells faster. In fig. 5.4 the combination of the angle of attack and Reynolds number at which stall cells have been observed are shown in comparison with the results from Dell'Orso and Amitay (2018) for a NACA 0015 wing. The plot shows the combinations that lead to stall cells but is rather indicative as the uncertainty for the NACA 0012 results is large due to the poor angle of attack and Reynolds number resolution.

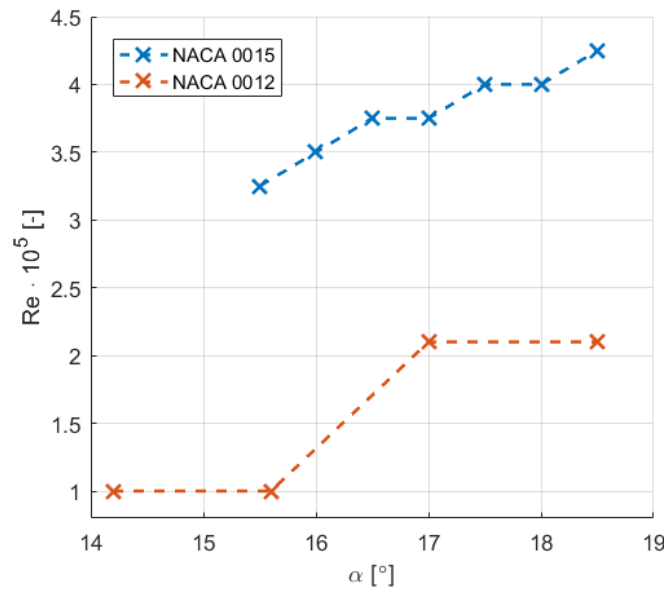


Figure 5.4: Reynolds number at which stall cells appear in the low Reynolds number regime, NACA 0015 data reproduced from Dell'Orso and Amitay (2018)

The data obtained with the tufts for the NACA 0012 unfortunately does not capture the minimum required Reynolds over a wider range of angles of attack. The minimum required Reynolds number is below $1 \cdot 10^5$ for most parameter combinations. This Reynolds number corresponds to a U_∞ of 5 m/s, using even lower freestream velocities was not deemed useful as the tuft inertia would be too large for the low flow momentum.

The data still shows how the minimum required angle of attack changes with a varying Reynolds number. In table 5.3 it can be seen how an increase in Reynolds number requires a larger minimum angle of attack for the formation of stall cells. When considering a combination of angle of attack and Reynolds number there appear to be two regions that can be investigated. As illustrated schematically in fig. 5.5. The yellow lines describe typical behaviour at high Reynolds numbers. These lines signify the minimum required angle of attack for a specific Reynolds number to obtain stall cells. At high Reynolds numbers a small change in angle of attack can determine whether stall cells occur or not. The green lines, on the other hand, are typical for low Reynolds numbers. In the low Reynolds number regime the angle of attack has less of an influence in determining whether stall cells will be present or not compared to the Reynolds number. The different lines in each regime represent how the gradient of the curves in the respective regime can vary. At the time of writing the gradients of these curves have only been observed in literature but have not been investigated. The gradients of these curves in literature have followed from limited data in which the goal of the experiments was not focused on the determination of this gradient. It can thus not be predicted what the bounding curve for stall cell formation should look like with respect to the angle of attack and Reynolds number combination over an extensive Reynolds number range.

The curves shown in fig. 3.1, also appear to follow this logic. These two different regimes have not been identified and distinguished before and have been seen as one and the same. However this distinction appears

to bear importance in assessing the stall cell criteria for a specific experiment. The data presented by Manolesos and Voutsinas (2014) is most likely obtained in the high Reynolds number regime and the data presented by Dell'Orso and Amitay (2018) in the low Reynolds number regime. The respective Reynolds number ranges used in those publications support this assumption.

Since the Reynolds number for the tuft experiments discussed here is relatively low, it would be expected to obtain data that behaves according to the low Reynolds number regime. This would result in data that provides information about the green curves in fig. 5.5. However the resulting data giving information about the minimum requirements for stall cells is predominantly in the high Reynolds number regime (yellow curves). As mentioned earlier, the minimum required Reynolds number in the low Reynolds number regime could not be captured in the tuft experiments due to physical limitations of the setup. Furthermore the steps in Reynolds number are an order of magnitude larger than the sensitivity of the minimum required Reynolds number for stall cells in the low Reynolds number regime.

The data in fig. 5.6 for flap angle zero degrees clearly shows that the curve in the high Reynolds number range has a positive gradient. The only exception is at the maximum tested Reynolds number where stall cells start to appear at smaller angles of attack again, this will be discussed in more detail later in this section. Considering the coarse angle of attack resolution it can be said that the trend which is observed has a strong positive $d\alpha/dRe$ gradient, in the high Reynolds number regime. When the results from Dell'Orso and Amitay (2018) are considered it can be noted that the angle of attack resolution is 0.5° and still no $d\alpha/dRe$ gradient can be observed in the high Re regime. The results published by Dell'Orso and Amitay (2018) show that irregardless of the Reynolds number stall cells will only appear after an angle of attack of 15.5° . Finally the results published by Manolesos and Voutsinas (2014) show that for an increasing Reynolds number the minimum required angle of attack for stall cell formation decreases, resulting in a negative $d\alpha/dRe$. This means that in the diagram in fig. 5.1d, each of the gradients of the yellow lines corresponds to one of the cases discussed.

The airfoil used by Manolesos and Voutsinas (2014) is the thickest airfoil with 18% and has a camber. The airfoil used by Dell'Orso and Amitay (2018) is the symmetric NACA 0015 and the airfoil used with the tufts presented here is the NACA 0012. A crude estimation of the $d\alpha/dRe$ gradients for the high Reynolds number regime results in: $-0.2 \cdot 10^{-5}$ degrees for the thickest airfoil, 0 degrees for the NACA 0015 and $2.5 \cdot 10^{-5}$ degrees for the NACA 0012 presented here. It appears that some relation between the thickness and the $d\alpha/dRe$ gradient in the high Reynolds number range exists. The relationship indicates that thicker airfoils have a more negative gradient in the high Reynolds number regime.

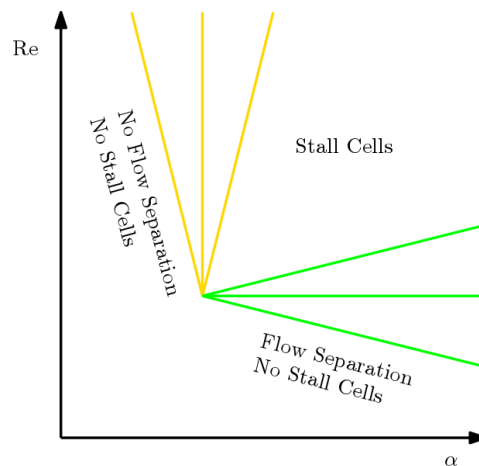


Figure 5.5: Minimum angle of attack and Reynolds number combination for stall cells

$Re \cdot 10^5$						
5.1	/	\tilde{t}	$1 t + \tilde{b}$	2	2	
4.1	/	/	$\tilde{1} m$	1 m	2	
3.1	/	/	\tilde{t}	$1 t + \tilde{b}$	2	
2.1	/	/	$1 t + \tilde{1} b$	2	s t + 1 b	
1.0	$\tilde{1} m$	$\tilde{1} t + s b$	$\tilde{1} t + \tilde{s} b$	$\tilde{1} t + 1 b$	2	
	12.8	14.2	15.6	17.0	18.5	$\alpha [^\circ]$

Table 5.4: Flow phase diagram for full wing with $\beta=5^\circ$

$Re \cdot 10^5$						
5.1	/	\tilde{t}	$1 t + \tilde{b}$	$\tilde{2}$	2	
4.1	/	/	$1 t + \tilde{b}$	$\tilde{2}$	2	
3.1	/	/	$\tilde{1} t$	$\tilde{2}$	2	
2.1	/	$\tilde{1} t + \tilde{1} b$	$\tilde{1} t + 1 b$	2	2	
1.0	$\tilde{2}$	2	$\tilde{1} t + 1 b$	$\tilde{1} t + 1 b$	s t + 1 b	
	12.8	14.2	15.6	17.0	18.5	$\alpha [^\circ]$

Table 5.5: Flow phase diagram for full wing with $\beta=10^\circ$

The experiment with tufts also covered multiple flap angles such as mentioned earlier and shown in table 5.4 and table 5.5. After the discussion on thickness effects by comparing the results shown here with literature, the different flap angles allow for an investigation of the camber effects.

Again the two different regimes can be investigated. The low Reynolds number regime is barely noticeable for the NACA 0012 wing with zero degrees flap. When increasing the flap angle the full span separation that precedes the stall cells is not encountered anymore at all. The increased flap angle causes stall cells to appear at lower Reynolds numbers. It is likely that the curve representing the low Reynolds regime stall cell requirements, shifts to even lower Reynolds numbers. Since the low Reynolds number regime is not captured for the flap angles equal to five and ten degrees, no observations can be made regarding the gradient.

The high Reynolds number regime can still be observed for increasing flap angles. Comparing these results for different flap angles requires using a common reference flow scenario. The flow cases on the limit of the high Reynolds number regime are not the same over a range of parameter combinations ($1m, \tilde{1}t, 1t + \tilde{1}b, \dots$). This is due to the step size being large for both the Reynolds number and angle of attack, possible hysteresis effects and the unsteady nature of stall cells in this experiment. In order to still be able to make a meaningful comparison it is chosen to use a flow scenario which occurs frequently or can be predicted to take place in between two flow scenarios. The chosen scenario is one stall cell at the top (whether or not unsteady) and a transitional or unsteady flow at the bottom. This flow scenario takes place usually after the formation of one stall cell and before the formation of two stall cells in terms of angle of attack. Therefore either the flow scenario has been observed or can be assumed to be in between two observed flow scenarios. When the respective combination of angle of attack and Reynolds number are plotted the result is such as shown in fig. 5.6.

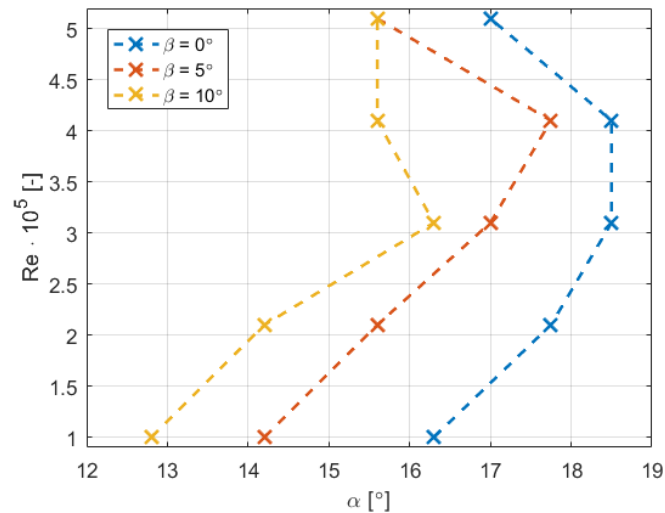


Figure 5.6: Angle of attack requirement in the high Reynolds number regime for the full wing

The curves show a similar gradient. The curves seem to be offset from each other with a constant value over the Reynolds range. This implies that, contrary to the thickness, the camber has a negligible influence on the $d\alpha/dRe$ gradient in the high Reynolds number regime. The effect of the camber displaces the minimum required angle of attack to lower values in the high Reynolds number regime.

Finally some remarks have to be made. First of all, the step size has been consistently high for all parameters. This prohibits the observation of more detailed trends. Certain flow scenarios occur over only a very small angle of attack or Reynolds number range, these have sometimes not been observed due to the large step size. In the discussion above the results for the highest Reynolds number have been neglected. This is for two reasons, first, the tendency of the wing to stall first at the top side of the wing might be related to the turbulence in the wind tunnel, which could be amplified at high velocities. Which then in turn causes the wing to stall sooner than would be expected. The second reason is the lack of corrections applied to this data. The flow scenarios of interest are all in stall, leading to negative pitching moments. The angle of attack in reality is thus smaller than the ones noted in the tables. This effect grows stronger at higher velocities. This means that the high velocity results should shift to slightly smaller angles of attack. As the maximum angle of attack correction was said to be one degree, the correction is smaller than the 1.4 degree step size, even corrected values would have a similar position in the tables, leading to similar qualitative analyses. It would however influence the plot in fig. 5.6. At lower Reynolds numbers a source of uncertainty is the use of the tufts themselves. They introduce a significant disturbance near the surface. The influence of this disturbance is not known. Finally it has to be mentioned that the flap angle adjustment is compared to a change in camber. This is a crude approximation as normally camber is continuously distributed. It is possible that the discontinuity in the camber line of the NACA 0012 airfoil with flap deflection has a considerable influence. It would not be unreasonable to expect the flow to react more strongly to the change from zero flap angle to five degrees, compared to the change from five to ten degrees flap angle. However a straightforward comparison of two airfoils would never be possible by defining an airfoil through a limited amount of parameters. Airfoils have distributed thickness and camber profiles, additionally other parameters such as leading edge radius or trailing edge thickness can play a role too. The goal of the experiment that has been discussed was to vary the flap angle to such a large extent that it overshadows the small influences of the other characteristics of airfoils.

5.1.2. Wind Tunnel Turbulence Intensity

From the tuft experiment performed on the full wing it has become apparent that stall cells emerge first on the top half of the span that is near the ceiling of the wind tunnel. This is unusual as in literature no such bias has been described. This leads to the conclusion that a physical or aerodynamical aspect of the setup could be responsible for this.

Traditionally stall would be linked to an angle of attack which is too large. A bias in angle of attack along the

span implies a twist. It has been verified with a plumb line when the wing is installed that no twist is present in the wing. Furthermore small disturbances on the wing surface promote boundary layer transition and delay stall. However when stall cells can occur, they can be triggered by such disturbances. Thereby inducing stall sooner such as described by Manolesos and Voutsinas (2014). For this reason a strip of roughness was applied to the suction surface, upstream of any other disturbance on the wing surface. Although Dell'Orso et al. (2016) mentions that the use of 2D strip has no stall cell inducing effect, it is hoped that the effect of the trip supersedes the disturbances otherwise caused by stickers downstream. The strip was noticed to reduce some of the bias, but did not eliminate it as shown by the tuft results that were obtained with the strip. Following the reasoning that stall cells are created by 3D disturbances, one of the last possible culprits is the turbulence intensity in the wind tunnel such as mentioned by Manolesos and Voutsinas (2014).

In order to investigate the Turbulence Intensity (TI) of the wind tunnel test section Hot Wire Anemometry (HWA) is used. The setup with the hot wire probe allowed to traverse the probe in a 2D plane perpendicular to the freestream direction. The wind tunnel cross section has been sampled at 20 locations, at 10 kHz for 120 seconds. A summary of the locations and velocities which have been sampled is shown in fig. 5.7. Positions 6 to 15 have been tested twice, where the entire setup has been taken down and replaced for the second round of measurements. The results shown use the average obtained TI from the two experiments for positions 6 to 15.

Type	WT velocity [m/s]	HW position	position	width [mm]	height [mm]
Calibration	0,5,10,15,20,25,30	1	1	401	262
Measurement	10,20,30	2	2	401	523
Measurement	10,20,30	3	3	401	785
Measurement	10,20,30	4	4	401	1047
Calibration	0,5,10,15,20,25,30,35	5	5	401	1308
Calibration	0,5,10,15,20,25,30,35	6	6	802	262
Measurement	10,20,30	7	7	802	523
Measurement	10,20,30	8	8	802	785
Measurement	10,20,30	9	9	802	1047
Calibration	0,5,10,15,20,25,30,35	10	10	802	1308
Calibration	0,5,10,15,20,25,30,35	11	11	1203	262
Measurement	10,20,30	12	12	1203	523
Measurement	10,20,30	13	13	1203	785
Measurement	10,20,30	14	14	1203	1047
Calibration	0,5,10,15,20,25,30,35	15	15	1203	1308
Calibration	0,5,10,15,20,25,30,35	16	16	1604	262
Measurement	10,20,30	17	17	1604	523
Measurement	10,20,30	18	18	1604	785
Measurement	10,20,30	19	19	1604	1047
Calibration	0,5,10,15,20,25,30,35	20	20	1604	1308

Figure 5.7: Test matrix for the turbulence intensity measurements with HWA

Due to practical limitations of the test setup it was not possible to cover the entire test section with the HWA measurements. In fig. 5.8 the area which has been covered by the HWA measurements is shown in green, and the test section in grey. The drawing is made to scale (excluding chamfers) to give an indication of the relative area for which the TI is mapped. For the experiments with the wing installed the sides of the test section are of less importance. The top and bottom area which have not been covered with the HWA measurements do still bear importance. The results that are shown only cover the green area from fig. 5.8, interpolation is used between the known measurement points.

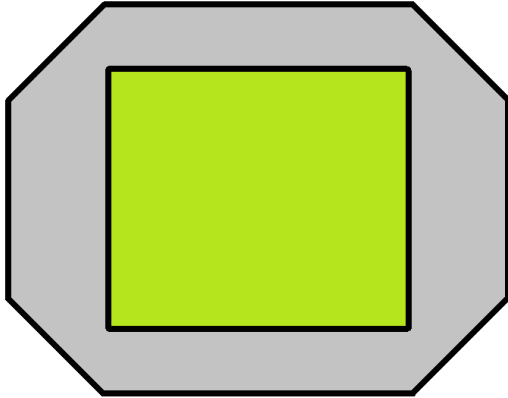


Figure 5.8: Interpolated area of TI measurements

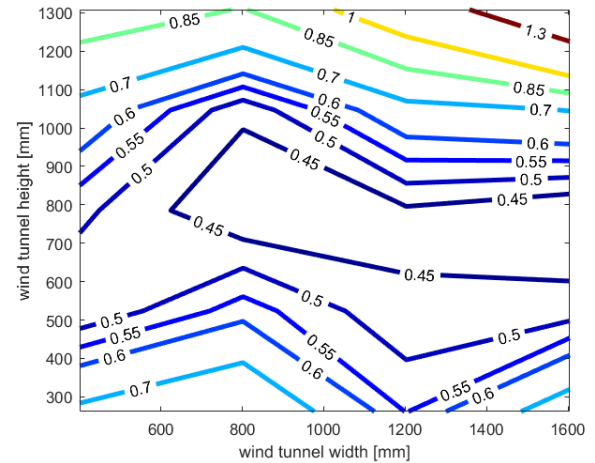
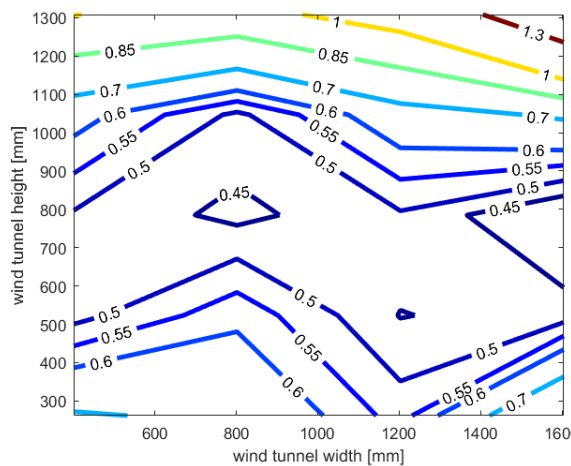
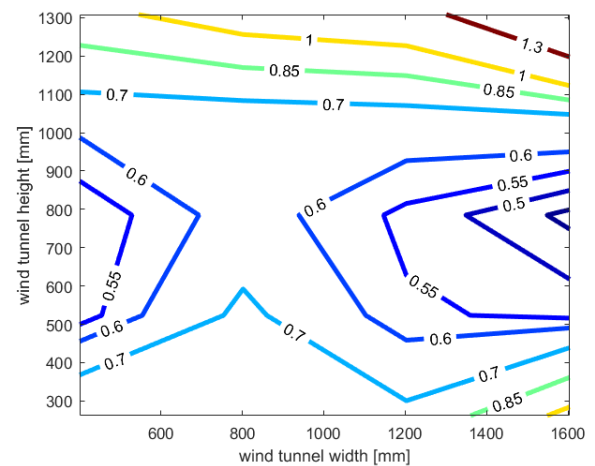
Figure 5.9: TI [%] for $U_{\infty} = 10$ m/s

fig. 5.9 shows the resulting TI in percentage for a free stream velocity of 10 m/s. For all the plots of the TI the convention is that the flow is coming out of the page, this means that the left hand side of the image corresponds to the suction side of the wing in the other experiments that are discussed. It can easily be observed that the lowest turbulence intensity is found near the middle of the height of the test section. A large area near the middle of the height has a TI of less than 0.5%. Previous experimental stall cell investigations have reported TI values ranging from 0.15 to 1% approximately. Near the top and bottom of the TI increases due to the physical disturbances at the walls. Specifically the top side of the test section experiences relatively strong turbulence levels. This might be due to the presence of multiple rails and small ceiling panels located upstream. The side walls of the wind tunnel introduce less turbulence, no significant effect from the sidewalls can be observed.

Figure 5.10: TI [%] for $U_{\infty} = 20$ m/sFigure 5.11: TI [%] for $U_{\infty} = 30$ m/s

From fig. 5.10 and fig. 5.11 it can be seen that increasing the freestream velocity increases the TI near the centre of the test section. The TI remains almost constant near the top wall for all three freestream velocities. The bottom wall is affected more by the freestream velocity.

The higher TI near the top of the test section could be a factor in the mechanisms that drive stall cells to occur near the top rather than the bottom initially. Earlier it was also discussed how at high Reynolds numbers the wing starts to show stall cells that occur earlier. It was assumed that this is uncharacteristic stall cell behaviour and deemed a consequence of unknown factors. It is possible that the relatively large increase of turbulence intensity when going from 20 m/s to 30 m/s plays a role. This assumption follows from the reasoning that the high turbulence level at the top can trigger stall cells to occur.

5.1.3. Preliminary Conclusions

The first set of experiments considered both tufts on a NACA 0012 wing and the measurement of the turbulence intensity of the wind tunnel test section. The use of tufts is a quick way to gain insight in the flow scenarios that can occur near the wing surface. Different flow scenarios have been induced by varying the angle of attack, flap angle and Reynolds number.

Identifying flow scenarios is a crucial practice in the investigation of stall cell requirements. In literature multiple examples of flow visualisation to investigate the requirements for stall cell formation can be found. The results obtained with tufts that have been presented here have been compared to results from both Dell'Orso and Amitay (2018) and Manolesos and Voutsinas (2014). Investigating the requirements for stall cells has been focused on finding the required combination of angle of attack and Reynolds number. This has led to contradicting results in literature. Due to controlled and similar test environments in literature with varying results, it is reasoned that the different results for the stall cell requirements are a consequence of different airfoil profiles.

In finding the required angle of attack and Reynolds number combination for stall cell formation the results can be represented as a curve. This curve can be misleading as the formation of stall cells occurs beyond a certain angle of attack and Reynolds number, which in the flow phase diagrams represents an area. This area can be approximated to be bound by two curves. One curve identifies the required angle of attack and Reynolds number for a high Reynolds number regime and the other for a low Reynolds number regime.

The investigation into the stall characteristics of the NACA 0012 wing used in this report uses a similar angle of attack and Reynolds number range as reported by Dell'Orso and Amitay. The wing used by Dell'Orso and Amitay has a NACA 0015 airfoil, this airfoil shape only has a minor increase in thickness compared to the NACA 0012 profile. Still the results show convincingly different characteristics. It has been observed that the thin airfoil shape experiences stall cells at much lower Reynolds numbers. Due to the physical limitations of the experiment it was not possible to determine whether the curve in the low Reynolds number regime translates or rotates under influence of profile thickness. In the high Reynolds number regime the gradient of the bounding curve was found to be larger than for the NACA 0015 wing. This trend in the high Reynolds number regime also continued when observing the negative gradient for the 18% thickness airfoil used by Manolesos and Voutsinas. The effects of the airfoil thickness on the stall cell requirements are illustrated in a diagram shown in fig. 5.12. It is shown how thinner airfoils have a higher $d\alpha/dRe$ gradient for stall cell formation in the high Reynolds number regime. It is also shown that in the low Reynolds number regime the thin airfoils experience stall at lower Reynolds numbers, however it can not be said whether this is caused by a gradient change or translation.

The NACA 0012 wing used for the experiments also has a movable plain flap of 0.33 times the chord length. Flap deflections in this report are assumed to simulate the effect of adding camber to an airfoil. Again the effects of adding camber can be investigated in the two Reynolds number regimes. First in the low Reynolds number regime it was found that an increase in flap angle causes stall cells to occur at lower Reynolds numbers. In the high Reynolds number regime it was found that the camber of the airfoil influences the lateral position of the curve that determines the requirements for stall cell formation. The curve was found to retain the gradient over a range of flap angle settings, but shifts to lower angle of attack values for higher flap angles. These effects on the high and low Reynolds number regime due to the camber are also shown in fig. 5.12.

The influence of the airfoil profile on stall cell formation can be summarised as follows. Thick airfoils will experience stall cells sooner (low angle of attack) in the high Reynolds number regime, but later (relatively high Reynolds number) in the low Reynolds number regime. Thin airfoils exhibit opposite behaviour. The effect of increasing the camber will promote the formation of stall cells to lower angles of attack and lower Reynolds numbers.

Two remarks can be made regarding the airfoil profile influence such as has been described. First, the thickness has a peculiar influence in the low Reynolds number regime. If thin airfoils exhibit stall cells sooner, there has to be a limit to this behaviour. Reducing the thickness of the airfoil beyond a certain value will result in a wing which does not exhibit trailing edge stall anymore, thereby loosing one of the key requirements for stall cells.

The second remark is regarding the influence of camber. Comparing cambered with symmetric airfoils implies that symmetric airfoils also represent a limit value regarding camber. However when considering negative

camber it is possible that it has an opposite effect of what has been discussed here as the influence of camber. This gives rise to the hypothesis that identification of stall cell requirements for airfoils can not be generically captured by means of geometrical (thickness, camber, ...) parameters, but requires aerodynamic parameters (lift coefficient, circulation, ...).

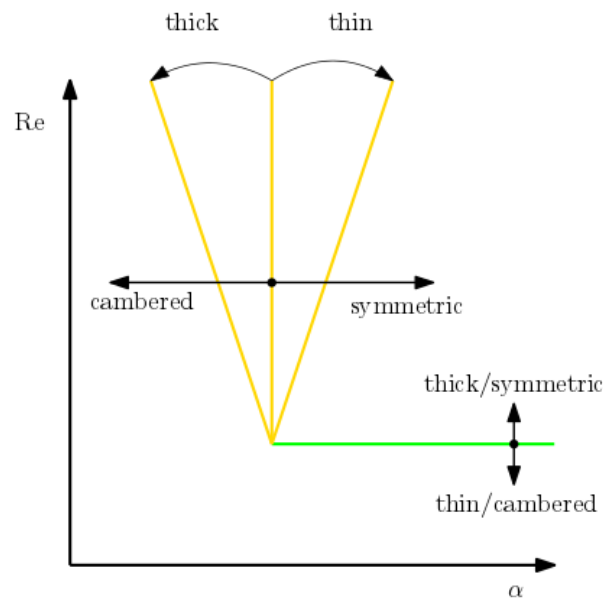


Figure 5.12: The influence of thickness and camber on the high and low Reynolds regime criteria for stall cell formation; straight arrows indicate translation, curved indicate arrows a gradient change

In the results of the tuft experiment it was also shown that stall cells at higher Reynolds numbers start to appear at lower angles of attack again. As this is unexpected and not observed in literature it is seen as caused by an uncontrolled parameter in the experimental setup and not an aerodynamic feature of the stalling NACA 0012 wing. Turbulence intensity has been mentioned in literature to be a possible cause for unsteady stall cell behaviour, furthermore very small 3D disturbances are proven triggers for stall cells. Since the triggering of stall cells by a disturbance on the wing causes stall cells to appear at a lower angle of attack over the whole range of Reynolds numbers, it can not be the cause for the observed behaviour. It has been reasoned that therefore the turbulence intensity can be a cause of the early stall cells at $Re = 5.1 \cdot 10^5$ by providing the necessary 3D disturbance.

The results of the turbulence intensity measurements consistently indicate that the turbulence intensity is higher near the top of the wind tunnel. This correlates with the observation for the tufts that stall occurs first at the top half of the wing. Furthermore at a Reynolds number of $6 \cdot 10^5$ it can be seen that the turbulence intensity at the location of the wing has increased by roughly 30% compared to $Re = 4 \cdot 10^5$. These observations do not prove that turbulence intensity is the cause, but add to the plausibility of the influence of the turbulence intensity on the formation of stall cells.

5.2. Single Stall Cell Investigation

After the investigation of stall cell characteristics on the full span wing it has been decided to limit the amount of flow phases that can occur by using only half of the wing span. This limits the AR to 2.6 and allows for only one stall cell to form on the wing. Additionally measurements of the lift and SPIV of the wake provide information about the wing performance and the stall cell characteristics. Initially the wing tuft experiment with increased angle of attack and Reynolds number resolution is discussed in section 5.2.1. Next the lift measurements are discussed in section 5.2.2. Finally the results from SPIV of the wake are presented in section 5.2.3.

5.2.1. Single Stall Cell Tufts

The reduction of the aspect ratio of the wing gives the flow less freedom and results in less flow scenarios that occur. The observations made with tufts for the full span wing indicated that the step size that was used for

both the angle of attack and Reynolds number was too big. For the investigation of the half wing with aspect ratio 2.6 the step size for the angle of attack has been reduced to 0.5° and $0.5 \cdot 10^5$ for the Reynolds number. The resulting parameter values that have been tested are shown in table 5.6. The angle of attack set for the experiments is not equal to the angle of attack of the wing, and this has been corrected as described in chapter 4. For reference, the table in fig. A.1 documents both the original and the corrected angle of attack. The Reynolds number is calculated similarly as for the full wing tuft experiment and the same flap angles are used.

α	$[\circ]$	11	11.5	12	12.5	13	13.5	14	14.5	15	15.5
		16	16.5	17	17.5	18	18.5	19	19.5	20	20.5
$\text{Re} \cdot 10^5$	$[-]$	1.0	1.5	2.1	2.6	3.1	3.6	4.1	4.6	5.1	
β	$[\circ]$	0	5	10							

Table 5.6: Parameter values for AR 2.6 wing tuft experiment

The flow scenarios that have been observed on the wing with aspect ratio 2.6 are shown in fig. 5.13. Attached flow is not shown as it is similar to the case shown in fig. 5.1a for the full wing. In fig. 5.13a the transitional phase between attached flow and separated flow is shown. The flow in this case still is predominantly attached in both a spatial and temporal aspect but shows short moments of locally separated flow. This flow scenario precedes separated flow such as shown in fig. 5.13b. The flow still shows a tendency to separate first near the top of the wind tunnel (left hand side in the images of fig. 5.13). For the separated flow the majority of the tufts show no preferential direction. Further increasing the angle of attack results in the appearance of unsteady stall cells. These stall cells were characterised by a bow tie pattern in the processed images for the full wing. For the half wing the unsteady stall cells do not exhibit the behaviour of appearing and disappearing randomly as much. The unsteady stall cells are observed to mostly jostle in spanwise direction. This jostling behaviour results in tufts next to the stall cell that resemble separated flow such as shown in fig. 5.13c. Finally further increasing the angle of attack results in more steady stall cells similar to the full wing tuft experiment. These steady stall cells can be hard to distinguish from the unsteady stall cells but will display better defined preferred tuft orientations such as shown in fig. 5.13d. The steady stall cells allow for a clear definition of the flow directions based on the tuft orientation such as shown in fig. 5.14.

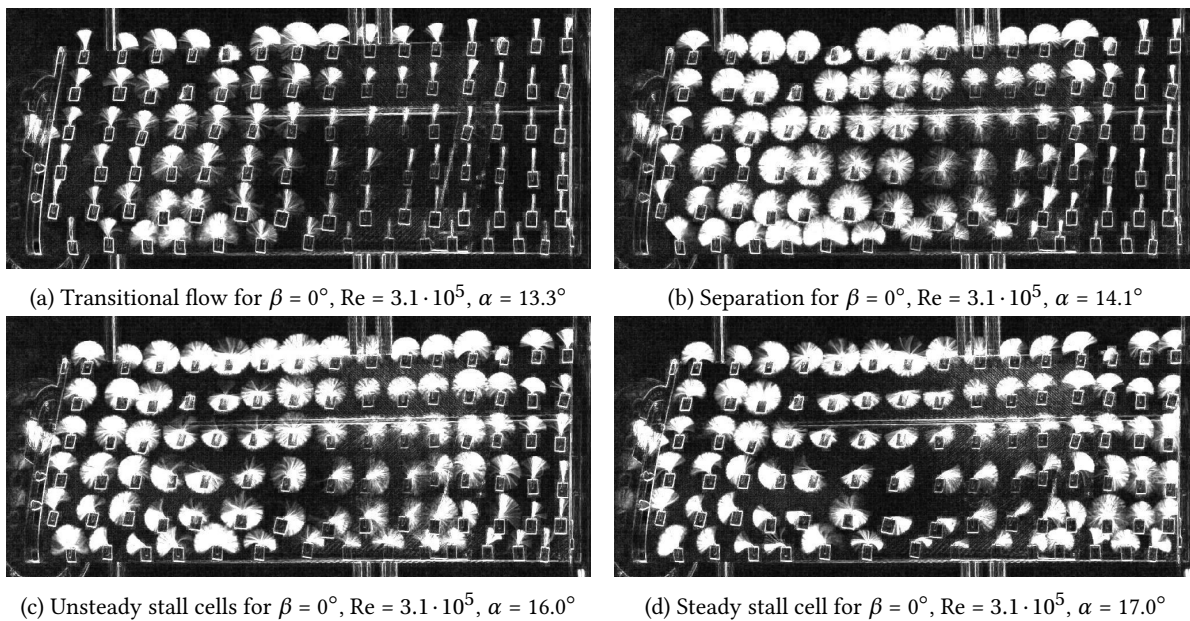


Figure 5.13: Possible tuft results for aspect ratio 2.6

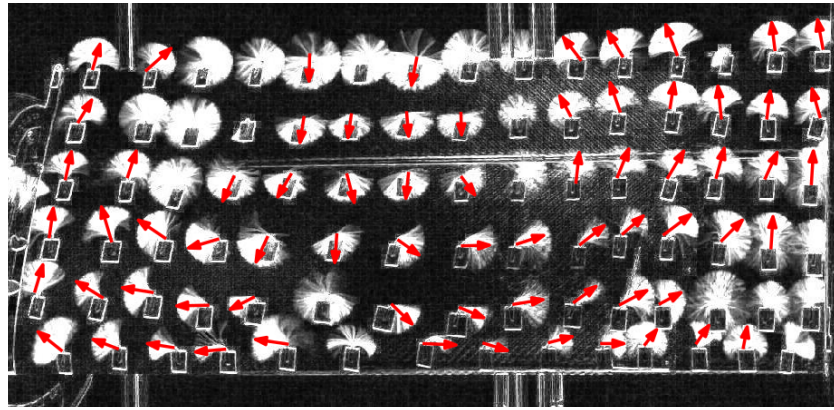


Figure 5.14: Flow direction indicated by tufts for $\beta = 0^\circ$, $Re = 3.1 \cdot 10^5$, $\alpha = 17.0^\circ$

The flow scenarios such as described above can be summarised and represented by a symbol to create a legend for a flow phase diagram such as in fig. 5.15. The processed tuft images can then be used to create flow phase diagrams for each of the flap angles tested. These flow phase diagrams are shown in fig. 5.16, fig. 5.17 and fig. 5.18. The black dotted line in the flow phase diagrams shows the location of maximum lift as obtained by the force balance. It can be seen that the maximum lift coefficient line does not cross the tuft angle of attack positions. This is because the lift coefficient is corrected for hysteresis effects, and the tufts are not because flow phases are not numerical.

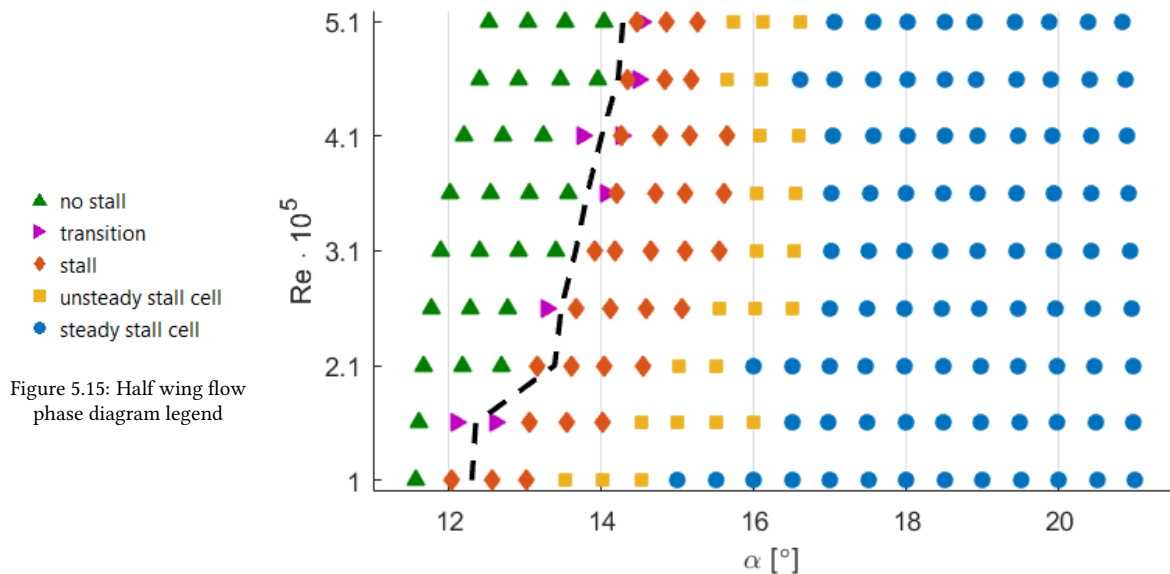


Figure 5.15: Half wing flow phase diagram legend

Figure 5.16: Flow phase diagram for half wing with $\beta = 0^\circ$

The first flow phase diagram represents the flow scenarios for the wing without flap deflection, shown by fig. 5.16. It can be seen that there is a region of stall in between attached flow and unsteady stall cell formation. This was not observed earlier for the full wing, but has been mentioned in literature before by Yon and Katz (1998). Next it can be seen that at even the lowest Reynolds number stall cells are present. The minimum Reynolds number in the low Reynolds number regime can thus not be captured. These observations are in this respect closer to the results published by Elimelech et al. (2012), considering a NACA 0009 wing, than the results from Dell'Orso and Amitay (2018). Furthermore it has been suggested by Dell'Orso and Amitay that a smaller AR will require a higher minimum Reynolds number for stall cell formation in the low Reynolds number regime, but this is not observable in comparison to the full wing tuft tests. The focus for these results is on the high Reynolds number regime. Just as for the full wing it can be seen that the curve of the α - Re requirement

for stall cells has a mostly positive $d\alpha/dRe$ gradient.

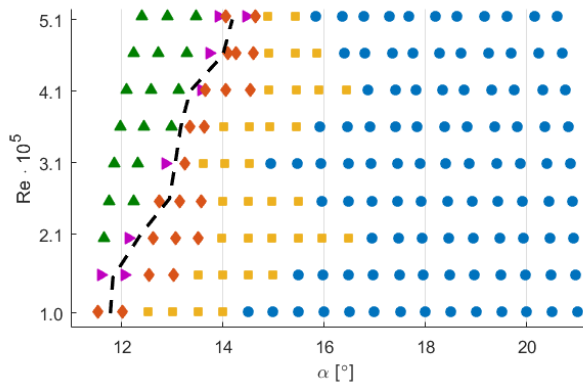


Figure 5.17: Flow phase diagram for half wing with $\beta = 5^\circ$

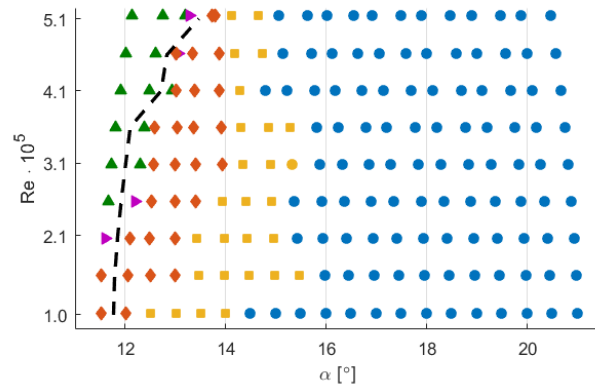


Figure 5.18: Flow phase diagram for half wing with $\beta = 10^\circ$

Similar flow phase diagrams have been created for flap deflections of 5° and 10° , as shown in fig. 5.17 and fig. 5.18 respectively. The flow phase diagram for flap angle 5° shows how stall occurs at lower angles of attack for larger flap angles. This trend continues when comparing the flow phase diagram for flap angle 5° with the flow phase diagram for a flap angle of 10° . Again stall cells are preceded by a small angle of attack range in which only separation occurs, this angle of attack range does not appear to change much under influence of the flap deflection. Increasing the angle of attack beyond the initial range in which separation occurs will cause unsteady stall cells to occur. Increasing the angle of attack further will stabilise the stall cells.

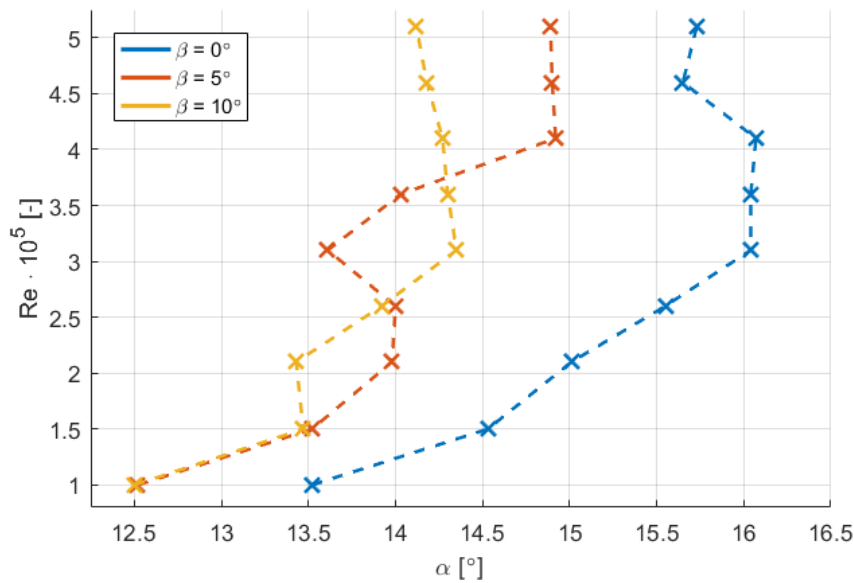


Figure 5.19: Angle of attack requirement in the high Reynolds number regime for the half wing

The main element of interest from this data is the curve which indicates the minimum required Reynolds number and angle of attack for stall cell formation in the high Reynolds number regime. For the full wing these curves were shown in fig. 5.6, for each of the flap angle configurations. For the half wing tuft experiment discussed here these curves are also constructed. The raw data is created with the data points that indicate the initial formation of unsteady stall cells. The data points used and resulting curves are shown in fig. 5.19. The curve for a flap angle of zero degrees indicates a progressively increasing minimum required angle of attack for increasing Reynolds number till a Reynolds number of $4 \cdot 10^5$ approximately. Beyond this Reynolds number the stall cells start to appear at lower angles of attack again, this is in agreement with the tuft observations on

the full wing.

For a flap angle of five degrees still the positive trend is visible. The region with a Reynolds number of $2.5 \cdot 10^5$ shows how stall cells occur sooner than would be expected according to the previous results shown in fig. 5.6. It is possible but rather unlikely that this is characteristic flow behaviour for stall cells. As has been discussed before, the aerodynamic phenomena leading to stall cell formation are still not well understood, thereby making it difficult to predict the cause of this behaviour.

The stall cell requirements for a flap angle of 10 degrees closely corresponds to the stall cell requirements for a flap angle of zero degrees, but shifted to lower angles of attack. This observation is in line with the suggested influence of camber on the stall cell requirements discussed in section 5.1.

For the half wing with zero flap deflection the formation of stall cells is at the highest angles of attack compared to the wing with flap deflections of five or ten degrees. This is in line with the observations made for the full wing. The full wing observations indicated an almost constant angle of attack offset caused by the flap deflection. For the full wing this offset can be estimated to be approximately two degrees of angle of attack between the flap angle zero and flap angle five degrees case. The difference between the case of flap five and ten degrees showed a similar constant angle of attack offset with a smaller value of approximately 1.5° . The offset observed for the half wing in between a flap angle of zero and five degrees is not constant and varies anywhere between 0.5 and 1.5° approximately. The offset between the minimum stall cell requirement curves for the flap angle of five and ten degrees is extremely small. It was to be expected to have a smaller offset between flap angle five and ten degrees compared to between zero and five degrees. However the offset in this case has nearly fully disappeared, indicating that a limit has been reached for the influence of camber due to the aspect ratio reduction. This indicates that the influence of the aspect ratio on stall cell formation criteria is larger than previously has been assumed or described in literature.

5.2.2. Force Measurements

The wing assembly is equipped with a force balance that allows to measure the forces that the wing experiences. These forces can then be converted into corresponding force coefficients, which allow for a comparison between different setups and experiments. Gregory and O'Reilly (1970) were among the first to observe stall cells. Their experiments also used a NACA 0012 wing and also the lift coefficient was obtained and published. Gregory and O'Reilly (1970) focused on Reynolds numbers much larger than used in the experiments discussed in this report. The lift coefficient plot from Gregory and O'Reilly (1970), shown in fig. 5.20, also has minimal data at a Reynolds number of $4.8 \cdot 10^5$. Results of force measurements with the NACA 0012 wing used in the experiments discussed in this report are added to the plot for a comparison. The Reynolds number for the obtained lift coefficient data is $4.1 \cdot 10^5$, this is only a small difference and is therefore not expected to influence the qualitative comparison much. The lift coefficient for the full wing is plotted in green. The full wing extends from the ceiling of the wind tunnel to the floor, giving a 2D flow scenario. This results in a lift polar with a gradient which is very close to 2π . The results for the full wing are in line with the results from Gregory and O'Reilly (1970). The lift polar shown in blue represents the lift coefficient obtained with the half wing ($AR = 2.6$), without an endplate. The tip vortex reduces the effective angle of attack locally and thus reduces the resulting lift coefficient. Finally the red lift polar represents the configuration that is used for the stall cell configuration, that is the half wing with an endplate. The gradient of the red lift polar sits somewhere around the middle in between the full wing and the half wing without endplate. This indicates that the endplate which is used reduces the tip vortex, but does not completely eliminate the effects of having a finite wing setup.

The resulting lift coefficient plot from Gregory and O'Reilly (1970) also shows the evolution of the lift coefficient with changing Reynolds number and constant setup. Increasing the Reynolds number implies that the inertial forces of the flow increase relative to the viscous forces. As has been mentioned in section 2.2.1, the viscous forces determine the boundary layer behaviour. With a high Reynolds number the boundary layer is thinner, thereby reducing the displacement thickness, resulting in an wing which performs closer to the potential flow solution of the same setup. Furthermore the reduced effect of the viscous forces causes the boundary layer to slow down less. Therefore boundary layer separation is delayed to higher angles of attack. For the wing this thus results in a higher stall angle of attack.

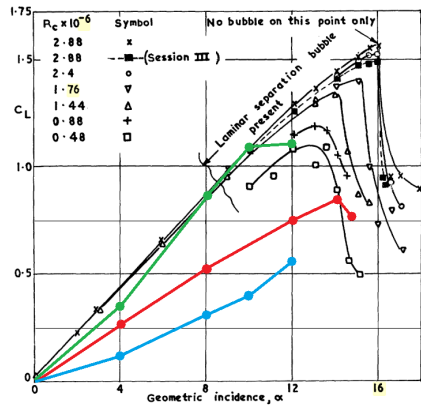


Figure 5.20: NACA 0012 C_L ; green: full wing, red: half wing with endplate, blue: half wing without endplate; $Re = 4.1 \cdot 10^5$ [14]

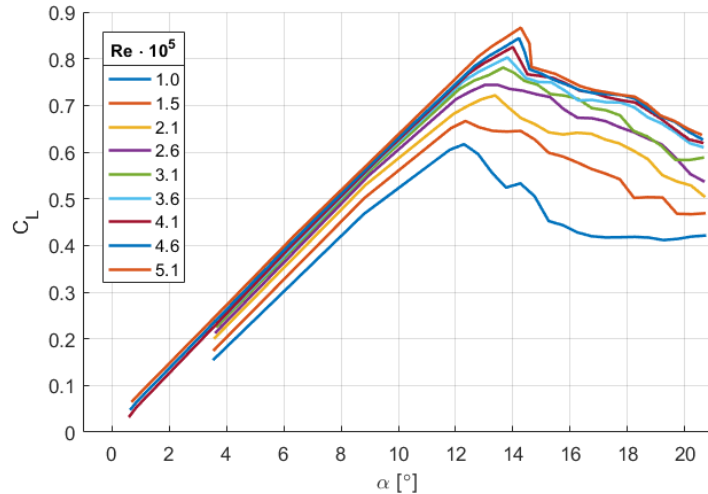


Figure 5.21: Lift coefficient for flap angle 0°

The lift coefficient for the NACA 0012 wing with AR 2.6 and endplate is shown in fig. 5.21. It can be seen that for increasing Reynolds numbers the slope of the lift polar slightly increases and the stall angle increases. The higher stall angle thus also results in a higher maximum lift coefficient. These observations are in line with literature. It can also be seen that at the lowest Reynolds numbers, lower than $2.6 \cdot 10^5$, there appears to be a small offset between the lift polars. The influence of the tufts with respect to the Reynolds number has not been investigated. Still the tufts are possible contributors to the low Reynolds number offset between different lift coefficient curves.

The Reynolds number effect for stall can be observed by two aspects. The first is that it postpones stall to larger angles of attack and therefore also higher lift coefficients. For a Reynolds number range of $1 - 5 \cdot 10^5$ the stall angle of the NACA 0012 wing without flap deflection varies between 12.3° and 14.3° , resulting in a maximum lift coefficient which varies between 0.62 and 0.87 respectively. The second aspect is the stall behaviour. At low Reynolds numbers stall happens very gradually and the $dC_L/d\alpha$ gradient after stall is similar for a range of Reynolds number up till $3.6 \cdot 10^5$ approximately. At Reynolds numbers higher than this value the stall behaviour changes. At the higher Reynolds numbers stall occurs more suddenly. Maximum lift is quickly followed by a sudden decline in lift coefficient. The $dC_L/d\alpha$ gradient after this initial steep drop appears to still be close to the gradient for the lower Reynolds stall.

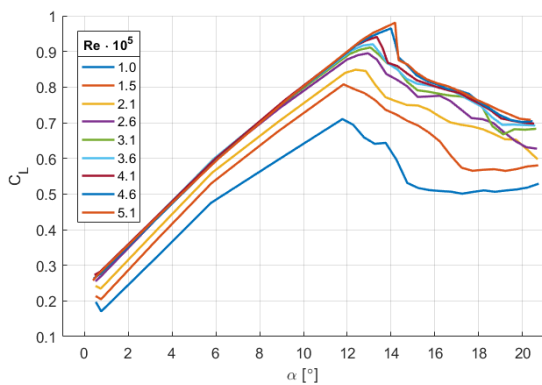


Figure 5.22: Lift coefficient for flap angle 5°

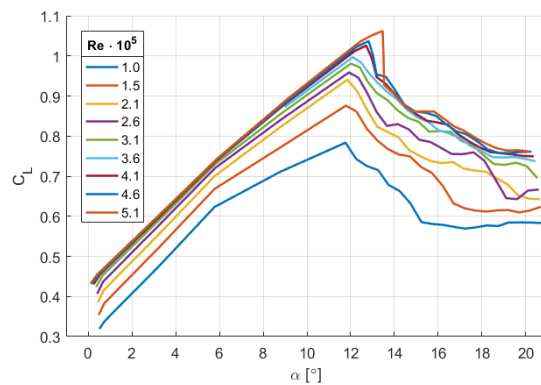


Figure 5.23: Lift coefficient for flap angle 10°

In fig. 5.22 and fig. 5.23 the lift coefficient plots are shown for flap angles of five and ten degrees respectively. They are very similar to the lift coefficient data as discussed for a flap angle of zero degrees. As expected the increase in flap angle causes the lift coefficient for a specific angle of attack and Reynolds number to be higher. Furthermore the stall angle is reduced by increasing the flap angle.

In order to link these lift coefficient measurements to the stall cell observations the tuft data is used. The main interest remains the requirements for stall cell formation. For this reason the initial formation of stall cells is obtained from the tuft observations. From the tufts the angle of attack and Reynolds number is known for a specific flap angle to obtain stall cells. With this information known, the respective lift coefficient can be obtained for when stall cells first start to appear for each flap angle and Reynolds number combination. The result is a dot on the lift polar which indicates the initial formation for stall cells. This is shown in fig. 5.24 for a flap angle of zero degrees.

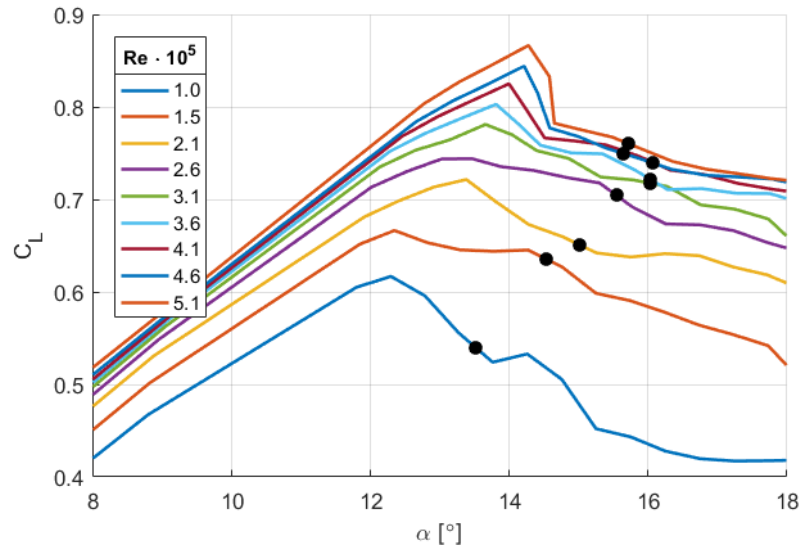


Figure 5.24: Initial stall cell formation for flap angle 0°

As can be expected the dots indicating stall cell formation shift to higher angles of attack as the Reynolds number increases initially, similarly as shown in fig. 5.19. At Reynolds numbers higher than $3.6 \cdot 10^5$ the dots start to shift towards lower angles of attack again, such as discussed earlier in the tuft results. This observation can now be linked to the lift coefficient behaviour around stall as influenced by the Reynolds number. Beyond a Reynolds number of $3.6 \cdot 10^5$ the lift coefficient around stall starts to show a steep drop. It is likely that these two events are related. The stall cell formation is also indicated for flap angle five degrees in fig. 5.25 and for flap angle ten degrees in fig. 5.26.

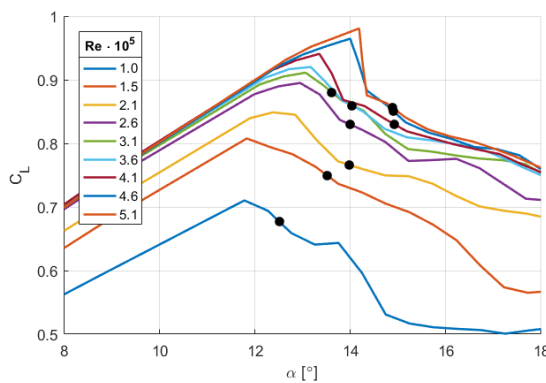


Figure 5.25: Initial stall cell formation for flap angle 5°

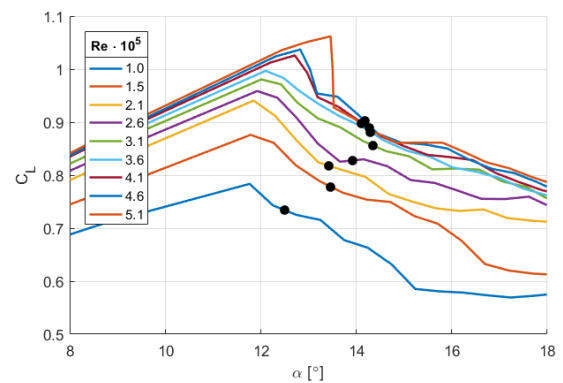


Figure 5.26: Initial stall cell formation for flap angle 10°

Based on the premise that the lift coefficient stall behaviour and the formation of stall cells are related, it appears that a difference in maximum lift coefficient and stall cell lift coefficient plays a role. In order to gain more insight in this lift coefficient range it is plotted for each of the cases tested, shown in fig. 5.27.

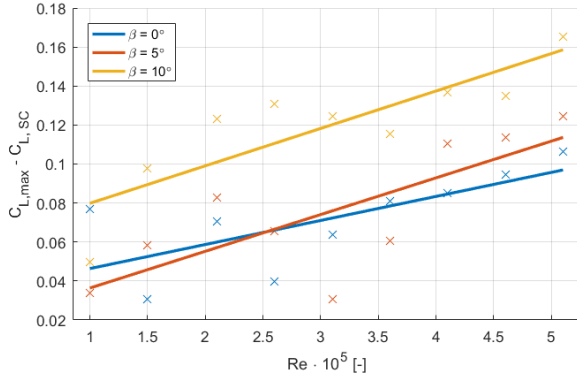


Figure 5.27: Difference between maximum C_L and C_L at which a stall cell appears

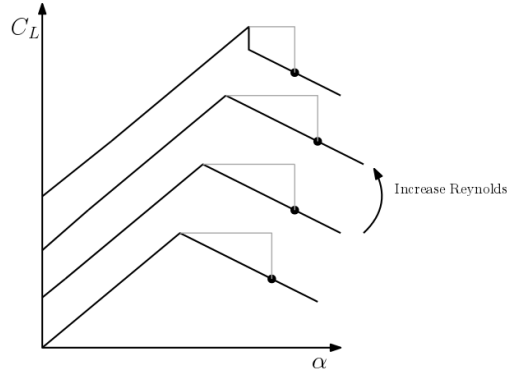


Figure 5.28: Constant $C_{L,max} - C_{L,SC}$ diagram

From fig. 5.27 it can be seen that the difference in C_L between the maximum value and the initial appearance of a stall cell is small. The accuracy of the ΔC_L values is relatively low as again the hysteresis effect plays a role due to the introduction of the tuft data for stall cell identification. Trend lines are shown that indicate that ΔC_L increases with Reynolds number. If the trend is neglected and the ΔC_L is assumed constant it becomes easier to understand how the lift coefficient and the stall cells are connected. In fig. 5.28 this hypothetical scenario is displayed. It can be interpreted as follows. A constant ΔC_L is required between maximum C_L and the initial stall cell C_L . As the lift polars have a similar gradient after stall, the ΔC_L is reached at a constant $\Delta\alpha$ after maximum lift. This is the case for lower Reynolds numbers with gradual stall. As the stall angle increases, also the stall cell angle of attack increases. When the Reynolds number increases and stall is no longer gradual this changes. The required ΔC_L for stall cell formation is now reached at lower angles of attack due to the steep C_L drop after maximum C_L .

With this understanding in mind it is possible to formulate an expression to capture this. In eq. (5.1) α_{SC} represents the angle of attack at which stall cells occur, $\alpha_{C_{L,max}}$ represents the angle of attack at which the maximum lift coefficient occurs, $\left(\frac{d\alpha}{dC_L}\right)_{PS}$ represents the inverse lift gradient Post Stall (PS) and ΔC_L represents the constant lift coefficient difference between maximum lift and the appearance of stall cells.

$$\alpha_{SC} = \alpha_{C_{L,max}} + \left(\frac{d\alpha}{dC_L}\right)_{PS} \cdot \Delta C_L \quad (5.1)$$

This equation allows to estimate the angle of attack at which stall cells will occur, based on the lift polar and an estimated value for ΔC_L . The ΔC_L value can be obtained from fig. 5.27. At this stage the equation does not allow for predictions without any information regarding stall cell formation, however it can still indicate the importance of taking the lift coefficient into account when considering stall cell formation.

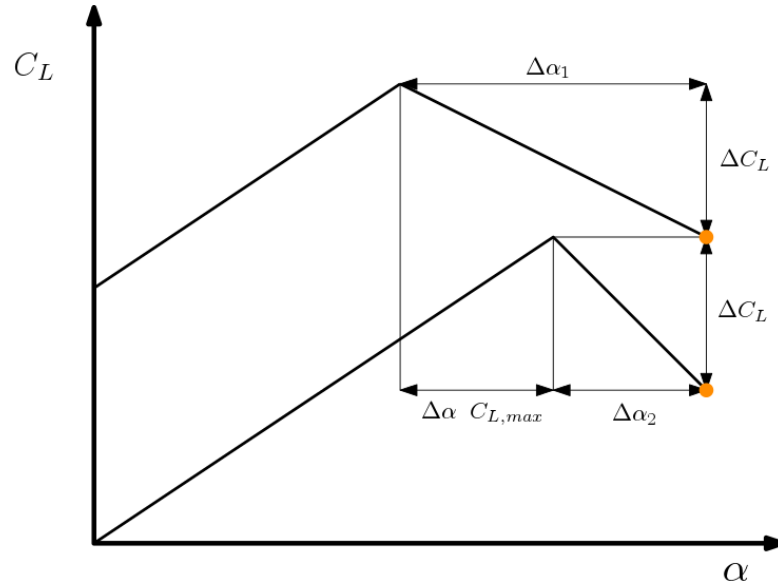


Figure 5.29: Lift coefficient based stall cell prediction diagram

With the trend that has been observed in fig. 5.27 it becomes possible to predict the stall cell formation angle of attack over a range of Reynolds numbers. For these predictions the lift polars are required, an initial guess for the ΔC_L and the trend of ΔC_L versus Reynolds number from the plot. In order to demonstrate the capability of this method the case for a flap angle of zero degrees will be compared with the case of flap angle five degrees. As has been established before, the change in camber has an influence on the requirements for stall cells. This difference caused by the geometrical parameter (camber) can now be captured by an aerodynamical parameter (lift coefficient). For this comparison eq. (5.1) is applied to both flap angle cases and subtracted to obtain the difference in stall cell angle of attack. A diagram to illustrate the principle of the calculation is shown in fig. 5.29. In fig. 5.29 two different lift polars are shown with different maximum lift angles of attack and different post stall lift curve gradients. Both cases obey the assumption that stall cells occur for the same ΔC_L after maximum lift. The angle of attack at which stall cells occur then follows from the angle of attack at maximum lift, and added to that, the required angle of attack range ($\Delta\alpha_{1/2}$ in fig. 5.29) after stall to reach the prescribed ΔC_L drop. The post stall gradient is calculated for each point of the lift polar, such that the calculated angle of attack for stall cell formation is on the point where the average post stall lift polar gradient is calculated. The equation used for the comparison is given by eq. (5.2), where subscripts 0 and 5 indicate the respective flap angles.

$$\alpha_{SC,0} - \alpha_{SC,5} = (\alpha_{C_L,max,0} - \alpha_{C_L,max,5}) + \left(\left. \frac{d\alpha}{dC_L} \right|_{PS,0} - \left. \frac{d\alpha}{dC_L} \right|_{PS,5} \right) \cdot \Delta C_L \quad (5.2)$$

From the equation it can be seen that when the gradients of the post stall lift polars are equal they cancel each other out, leading to a difference in stall cell angle dominated by solely the maximum lift angle of attack shift. In order to simulate this easily in the calculation ΔC_L has been set to zero. The resulting predicted angle of attack difference for stall cell formation for the two flap settings is shown in fig. 5.30. The plot shows the predicted angle of attack difference for varying Reynolds numbers. A reference line is shown in black, this line is obtained by using the results from the tufts. The tuft indicated angles of attack for stall cell formation are first subtracted and subsequently fitted with a second order polynomial. The predicted angle of attack difference calculated with the lift polars also uses a second order polynomial fit. Data points are not shown for clarity purposes. Two more curves are shown in fig. 5.30. As discussed earlier the required ΔC_L for stall cell formation can be assumed to be approximately constant, in that case the average value over a Reynolds number range is used (obtained from fig. 5.27) resulting in the yellow curve. When ΔC_L is assumed to be linear over a range of Reynolds numbers the resulting angle of attack difference is given by the purple curve. Both results obtained with either a constant average ΔC_L or a linearly varying ΔC_L correspond reasonably to the results obtained with the tufts. In the comparison of flap angle zero and five degrees the ΔC_L value used for both flap angles is the same, from fig. 5.27 it can be seen that this is a reasonable approximation.

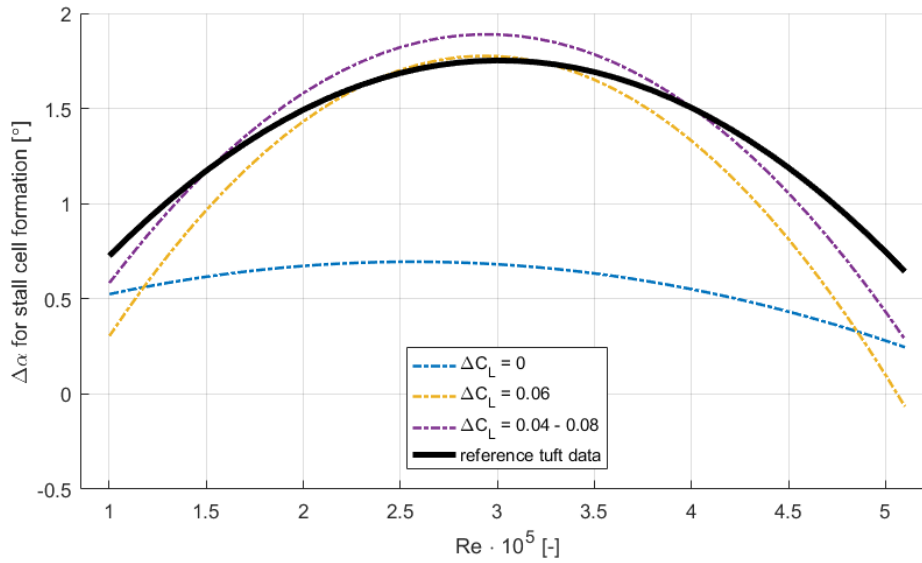


Figure 5.30: Predicted angle of attack difference for stall cell formation between flap angle zero and five degrees

When flap angle ten degrees is considered the ΔC_L is still linearly varying over a Reynolds range with a similar gradient but also has a offset compared to flap angle five or zero degrees, shown in fig. 5.27. When the lift coefficient method is used for predicting stall cells, this offset has to be taken into account. In fig. 5.31 the predicted difference in stall cell angle of attack for the flap angle of five and ten degrees is shown. In this comparison the difference between the two flap angles is better captured by a first order polynomial to visually illustrate the similarity, compared to the second order polynomial used before. In order to obtain the resulting prediction such as shown by fig. 5.31, two different linearly varying ΔC_L equations have been used. For the flap angle of five degrees the ΔC_L varies linearly between 0.04 and 0.11, for the flap angle of ten degrees the ΔC_L varies linearly between 0.08 and 0.16 for Reynolds numbers from $1 \cdot 10^5$ till $5.1 \cdot 10^5$. These linearly varying ΔC_L equations correspond to the linear fit applied to the ΔC_L obtained from the tuft data, shown in fig. 5.27.

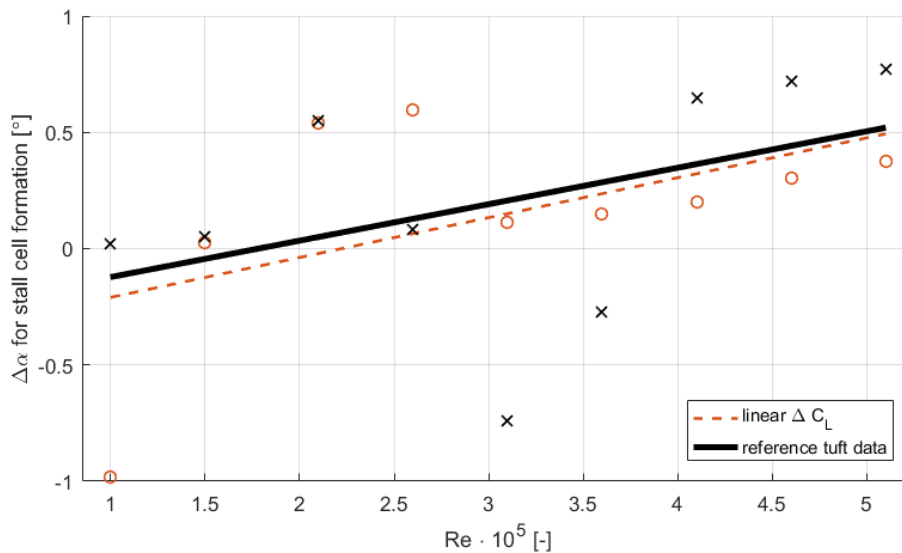


Figure 5.31: Predicted angle of attack difference for stall cell formation between flap angle five and ten degrees; data points and linear fit lines

Both fig. 5.30 and fig. 5.31 substantiate the hypothesis that the lift coefficient plays a important role in determining the inception of stall cells. The lift coefficient itself takes into account the Reynolds number, angle of

attack and airfoil shape. The promising results that have been presented indicate that there is potential to reduce the amount of factors in determining the stall cell formation criteria. This has been achieved by using the maximum lift coefficient as a reference point, setting a ΔC_L that is required after maximum lift for stall cells to occur and taking into account the post stall lift curve slope. The use of the lift coefficient to determine stall cell characteristics is not unprecedented, a paper by Gross et al. (2015) presents a model for spanwise spacing of stall cells by using lifting-line theory. In this model the spanwise spacing is determined with exclusively the post stall lift curve gradient as an input parameter. It has to be mentioned that the lift coefficient provides only a part of the data that actually is contained in the pressure coefficient. It is possible that by predicting stall cell formation based on the lift coefficient aspects of the flow behaviour that are crucial to stall cell formation are not noticed as they are averaged out. However as it is very difficult to obtain a full span distributed pressure coefficient experimentally, the selected focus has been to remain on working with the lift coefficient to allow a model to be of practical use. The data that has been used here to formulate the basis of the model is subjected to hysteresis effects. For this reason statistical analysis is used to identify relevant trends in the data. Further investigation to confirm the trends and obtain validation of the model is still required.

A short uncertainty quantification study can be applied to the model. The components of eq. (5.2) need to have their uncertainties defined, the sources of uncertainty are shown in table 5.7. Where P_1 represents the gradient of the linear fit of ΔC_L as shown in fig. 5.27, and P_2 the constant offset.

source	std uncertainty (\pm)
α	0.05°
C_L	0.0025
P_1	0.0055° · 10 ⁻⁵
P_2	0.018° · 10 ⁻⁵

Table 5.7: Sources of uncertainties for stall cell prediction model

With the sources of uncertainty identified, the uncertainty can be calculated according to eq. (5.2). Uncertainties relating to the different flap angles are assumed equal for the different flap angles. This assumption is based on the quantities having a similar order of magnitude and are calculated with the same procedure, leading to similar uncertainties. First the equation can be divided in a summation of uncertainties.

$$\delta(\alpha_{SC,0} - \alpha_{SC,5}) = \sqrt{\delta(\alpha_{C_L,max0} - \alpha_{C_L,max5})^2 + \delta\left[\left(\frac{d\alpha}{dC_L}\right)_{PS,0} - \frac{d\alpha}{dC_L}\right]_{PS,5} \cdot \Delta C_L}^2 \quad (5.3)$$

Straight forward solving of the first part of the summation.

$$\delta(\alpha_{C_L,max0} - \alpha_{C_L,max5})^2 = \sqrt{\delta\alpha_{C_L,max0}^2 + \delta\alpha_{C_L,max5}^2} = \sqrt{0.05^2 + 0.05^2} = 0.005 \quad (5.4)$$

Identifying the uncertainties in the second part of the summation

$$\delta\left[\left(\frac{d\alpha}{dC_L}\right)_{PS,0} - \frac{d\alpha}{dC_L}\right]_{PS,5} \cdot \Delta C_L = \left[\left(\frac{d\alpha}{dC_L}\right)_{PS,0} - \frac{d\alpha}{dC_L}\right]_{PS,5} \cdot \Delta C_L \sqrt{\left(\frac{\delta\left(\frac{d\alpha}{dC_L} - \frac{d\alpha}{dC_L}\right)}{\frac{d\alpha}{dC_L}\big|_0 - \frac{d\alpha}{dC_L}\big|_5}\right)^2 + \left(\frac{\delta\Delta C_L}{\Delta C_L}\right)^2}^2 \quad (5.5)$$

Assuming that both post stall gradients for flap angle zero and five degrees have equal uncertainties.

$$\delta\left(\frac{d\alpha}{dC_L} - \frac{d\alpha}{dC_L}\right) = \sqrt{\delta\left(\frac{d\alpha}{dC_L}\right)^2 + \delta\left(\frac{d\alpha}{dC_L}\right)^2} = \sqrt{2} \delta \frac{d\alpha}{dC_L} \quad (5.6)$$

Calculation of the post stall gradient uncertainty between maximum lift and stall cell inception for the case of flap zero and a Reynolds number of $3 \cdot 10^5$.

$$\delta \frac{d\alpha}{dC_L} = \frac{d\alpha}{dC_L} \sqrt{\left(\frac{\delta d\alpha}{d\alpha}\right)^2 + \left(\frac{\delta dC_L}{dC_L}\right)^2} = \frac{2.3}{0.06} \sqrt{\left(\frac{0.1}{2.3}\right)^2 + \left(\frac{0.005}{0.06}\right)^2} = 3.6 \quad (5.7)$$

Calculation of the ΔC_L uncertainty based on the fit applied to the data obtained from tufts and force measurements shown in fig. 5.27.

$$\delta \Delta C_L = \sqrt{(Re \cdot \delta P_1)^2 + \delta P_2^2} = \sqrt{(3 \cdot 0.0055)^2 + 0.016^2} = 0.023 \quad (5.8)$$

Different flap angles have different gradients post stall between maximum lift and stall cell inception, but both adhere to the same ΔC_L .

$$\left(\left. \frac{d\alpha}{dC_L} \right|_{PS,0} - \left. \frac{d\alpha}{dC_L} \right|_{PS,5} \right) \cdot \Delta C_L = 20 \cdot 0.07 = 1.4 \quad (5.9)$$

Final substitution of all the partial uncertainties.

$$\delta(\alpha_{SC,0} - \alpha_{SC,5}) = \sqrt{0.005 + \left[1.4 \cdot \sqrt{\left(\frac{\sqrt{2} \cdot 3.6}{20} \right)^2 + \left(\frac{0.023}{0.07} \right)^2} \right]^2} = 0.58^\circ \quad (5.10)$$

The uncertainty is found to be 0.58° approximately, for the case of flap angle zero and five degrees at a Reynolds number of $3 \cdot 10^5$. The difference in stall cell inception angle between these two flap angles was reported earlier to be approximately 1.75° by the tufts such as shown in fig. 5.30.

5.2.3. Stereoscopic Particle Image Velocimetry

The experimental results that have been discussed thus far have mostly focused on the identification of the requirements for stall cell formation. Tufts were used to differentiate between several flow scenarios that can occur. The force measurements provided quantitative data related to the different flow scenarios. In this section the results from Stereoscopic Particle Image Velocimetry (SPIV) are discussed. This method allows to obtain quantitative velocity information about the flow field within a stall cell. With the FOV perpendicular to the flow and near the trailing edge of the wing, the stall cell vortices are captured when trailing downstream. These vortices contain more information about the stall cell behaviour as will be discussed in the following section.

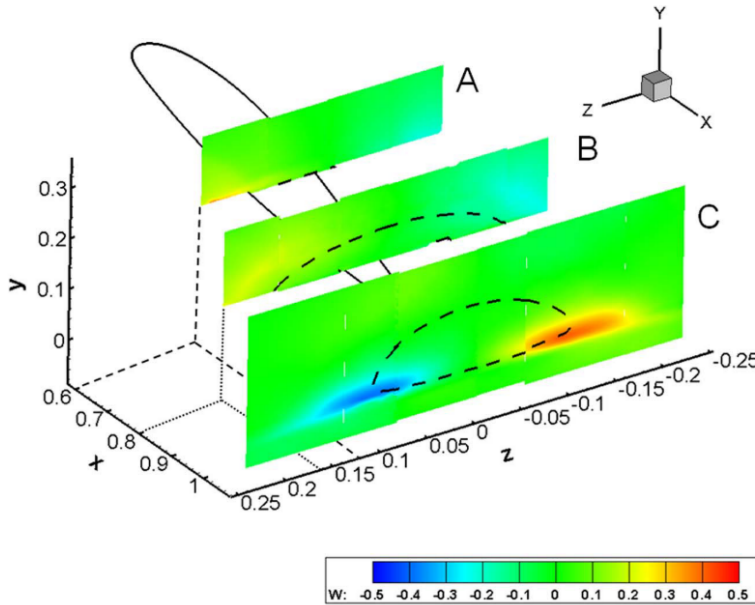


Figure 5.32: Normalised spanwise velocity at $X = 0.6$ (plane A), $X = 0.8$ (plane B), and $X = 1.06$ (plane C) [27]

Manolesos and Voutsinas (2014) used SPIV to observe the flow on many locations of a wing with stall cells. In fig. 5.32 results from Manolesos and Voutsinas (2014) are shown that present the spanwise velocity in a similar location (plane C) as investigated here. The C plane shown is at a location of $1.06 x/c$ and some characteristic flow of the stall cell is still visible. The results of the measurements that are presented in this section are obtained at locations between approximately $1.02 x/c$ and $1.06 x/c$ this is due to the angle of attack and flap

deflection moving the trailing edge position away relative to the laser sheet position. It is assumed that this change in distance from the trailing edge has a negligible influence on the measurements.

The SPIV measurements covered a range of cases with varying angles of attack, flap angles and Reynolds numbers. Due to time constraints not all the cases that have been covered with tufts could also be measured with SPIV. In order to investigate a wide range of cases it was chosen to limit the amount of captured image pairs per case to 100. The cases that will be discussed are shown in table 5.8. All angles of attack are tested at a Reynolds number of $2.0 \cdot 10^5$, while angle of attack 14° is also tested at Reynolds numbers of $1.0 \cdot 10^5$ and $4.1 \cdot 10^5$. Each of these measurements is further repeated to cover all three of the flap angles. Mind that the values for the angle of attack displayed in table 5.8 refer to the input angle of attack values. For the results presented in this section the angles of attack will be corrected as discussed in chapter 4.

α	[$^\circ$]	10	12	14	16	18
$\text{Re} \cdot 10^5$	[-]	1.0	2.1	4.1		
β	[$^\circ$]	0	5	10		

Table 5.8: Parameter values for AR 2.6 wing SPIV measurements

The focus for the analysis of the SPIV results is the identification of stall cell vortices. These vortices occur near the trailing edge and near the edges of the stall cells. They rise up from the wing surface and trail downstream. In this analysis they are used as a measure for the width of the stall cell. It has been mentioned before that the stall cell vortices bend inwards towards the centre of the stall cell before trailing downstream. This behaviour was not captured in the experiment that has been performed and is therefore assumed to be similar for all cases of stall cells. The stall cell vortices are related to the upstream flow inside the stall cell and the attached flow outside the stall cell. By quantifying the size of the stall cell vortex core and the strength, this can be interpreted as a measure for the strength of the stall cell. In fig. 5.33 to fig. 5.36 the normalised spanwise velocity as obtained from 100 averaged image pairs is shown, for increasing angle of attack with constant Reynolds number and flap angle.

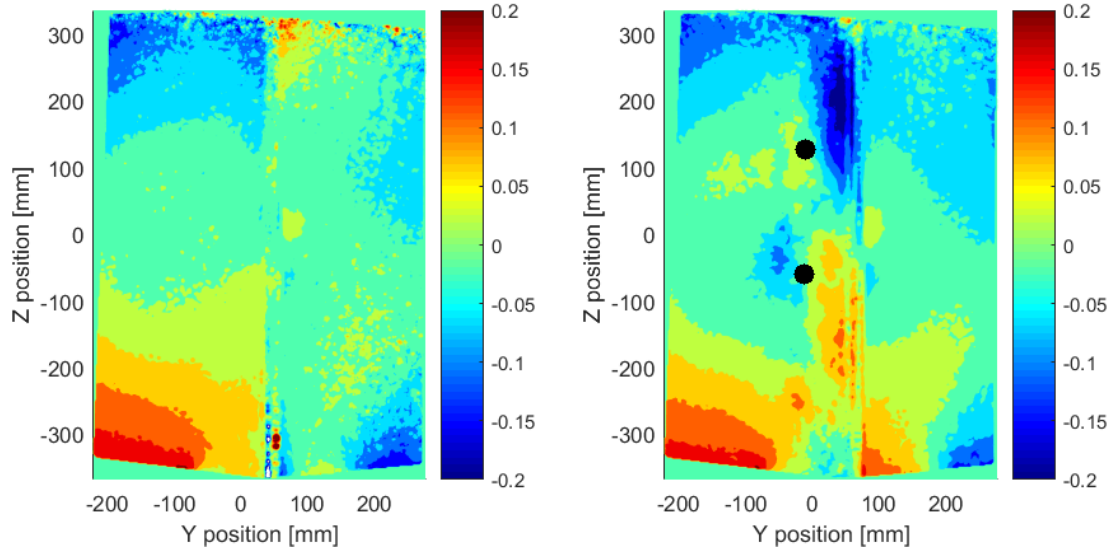


Figure 5.33: Normalised spanwise velocity for $\alpha = 10.5^\circ$, $\beta = 0^\circ$, $\text{Re} = 2.1 \cdot 10^5$ Figure 5.34: Normalised spanwise velocity for $\alpha = 14.54^\circ$, $\beta = 0^\circ$, $\text{Re} = 2.1 \cdot 10^5$; dots indicate approximate SC vortex centres

The angle of attack is an approximation as no force measurements have been conducted for this case. The spanwise velocity is normalised with the freestream velocity. The figure has a similar coordinate frame as fig. 5.32 with the z coordinate indicating the spanwise direction and the y coordinate indicating the distance from the wing surface. The zero position for the spanwise coordinate corresponds to a point 40mm offset from the actual midspan position. The zero position in the figures is closer to the wind tunnel ceiling (wing root)

than the end plate (wing tip). With the wing span 0.78 m this results in a FOV for the SPIV which captures the wing span from the root to approximately 3 cm from the tip.

For the case shown by fig. 5.33, which is near maximum lift, no stall cell is present. A further increase in angle of attack and the resulting spanwise velocity is shown in fig. 5.34, where a stall cell can be observed by the two dipole areas of spanwise velocity near the trailing edge. The centre of the stall cell vortices can be estimated to be around $[0, -50]$ and $[0, 125]$ for the $[y, z]$ coordinates. As a consequence of the end plate not fully mitigating the tip vortex, the stall cell centre is displaced more towards the wing root. In fig. 5.35 and fig. 5.36 the spanwise velocity is shown for further increasing angles of attack. It can easily be seen that the magnitude of the spanwise velocity induced by the stall cell vortices grows larger for increasing angles of attack. Additionally it can be seen that the area covered by the induced spanwise velocity also increases. These initial observations from the average results of a 100 image pairs indicate that the angle of attack has an influence on the stall cell.

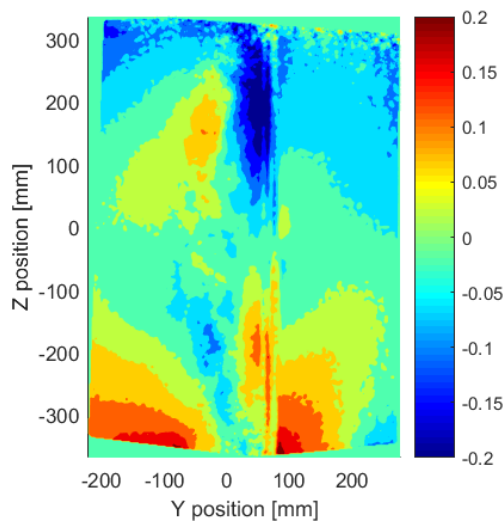


Figure 5.35: Normalised spanwise velocity for $\alpha = 16.5^\circ$, $\beta = 0^\circ$, $Re = 2.1 \cdot 10^5$

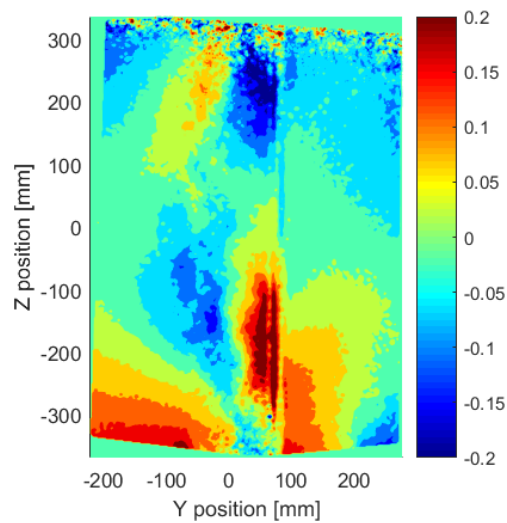


Figure 5.36: Normalised spanwise velocity for $\alpha = 18.48^\circ$, $\beta = 0^\circ$, $Re = 2.1 \cdot 10^5$

The spanwise velocity images discussed above consider the average result from a 100 instantaneous recordings. The stretched shape of the induced spanwise velocity from the stall cell vortices is a consequence of the averaging. Each instantaneous result consists of mostly turbulent flow with two recognisable spanwise velocity dipoles, where the dipole is the result of the spanwise component visualisation of the angular induced velocity by the stall cells. As explained in chapter 4 the instantaneous images can be used to identify the position and size of the stall cell vortices. An example of an instantaneous image is shown in fig. 5.37a. The stall cell vortices can be seen at spanwise locations of approximately 175 mm and -175 mm. In fig. 5.37b the result is shown from the optimisation which attempts to find the stall cell vortex characteristics. These characteristics include the position, size and strength. For each of the cases under observation the optimisation has been used to identify the stall cell vortex characteristics of each instantaneous result. These instantaneous results for each flow case then can be averaged to provide representative characteristics for a flow case. These averaged characteristics are used to analyse the stall cell behaviour for the different flow cases.

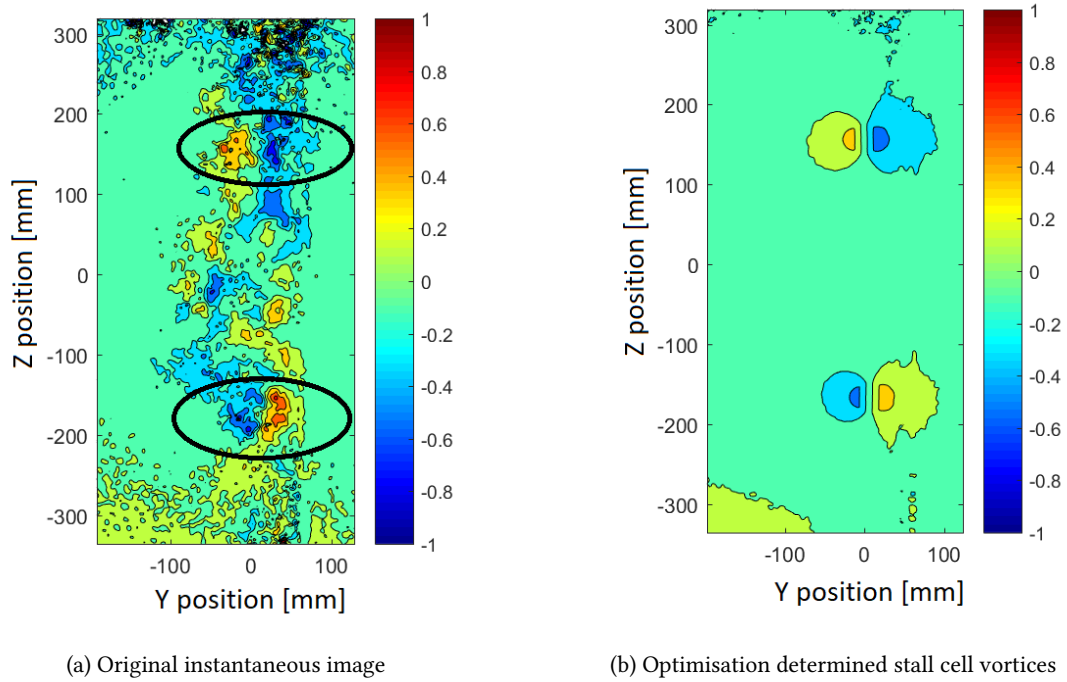


Figure 5.37: Stall cell vortex identification by means of spanwise velocity of instantaneous results

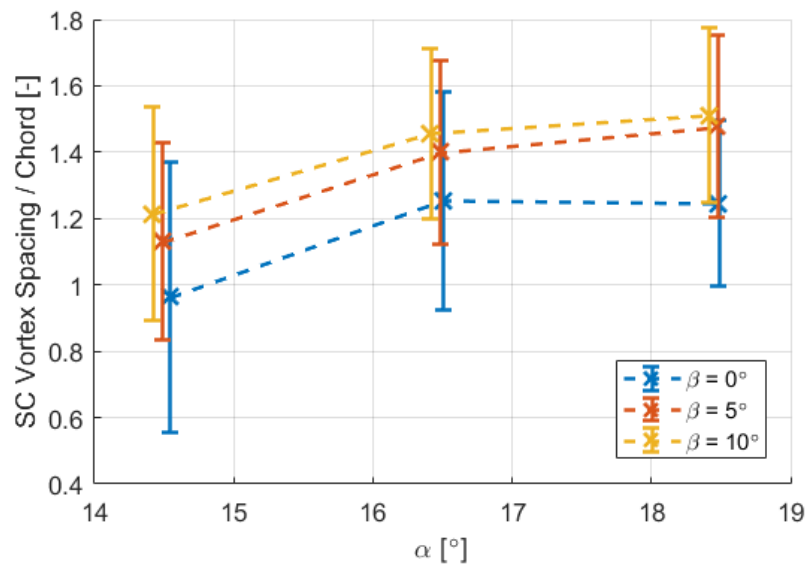


Figure 5.38: Average stall cell vortex spacing for $Re = 2.1 \cdot 10^5$

In fig. 5.38 the average spacing of the two stall cell vortices is shown for varying angles of attack and flap angles. The error bars in fig. 5.38 show plus/minus one standard deviation. The standard deviation in this case serves to show the unsteadiness of the stall cells. The large unsteadiness can be expected in a turbulent wake. It can also be observed that the unsteadiness of the stall cells is nearly constant over a range of angles of attack and flap angles.

For each flap angle it can be seen how an increase in angle of attack increases the width of the stall cell, as determined by the stall cell vortex spacing. The initial angle of attack change from approximately 14 to 16 degrees has the largest effect. Increasing the angle of attack beyond 16° only increases the stall cell width

marginally. It appears as if the stall cells converge to a specific size by increasing the angle of attack. This effect is not because the span of the wing is too short, as for higher flap angles stall cells grow wider. The increase in flap angle from zero to five degrees causes the stall cells to become wider, but the angle of attack trend is maintained for a specific flap angle deflection. Increasing the flap angle further again increases the stall cell width, but with a reduced rate. This reduced rate of growth in the width of the stall cell is most likely due to the discontinuity in the camber line playing a substantial role.

The stall cell width is also described by Gross et al. (2015). In the model presented by Gross et al. (2015) the stall cell spacing is equivalent to the stall cell width. The model predicts a larger spacing for a more negative post stall lift polar gradient. This implies that for increasing flap angles the post stall lift curve slope for initial stall cell formation should be more negative. This is in line with the observation made with the tufts and the force measurements. The post stall gradient for different flap angles and Reynolds numbers is shown in fig. 5.39. For the Reynolds number of $2.1 \cdot 10^5$ it can be seen that the post stall gradient is more negative for the higher flap angles.

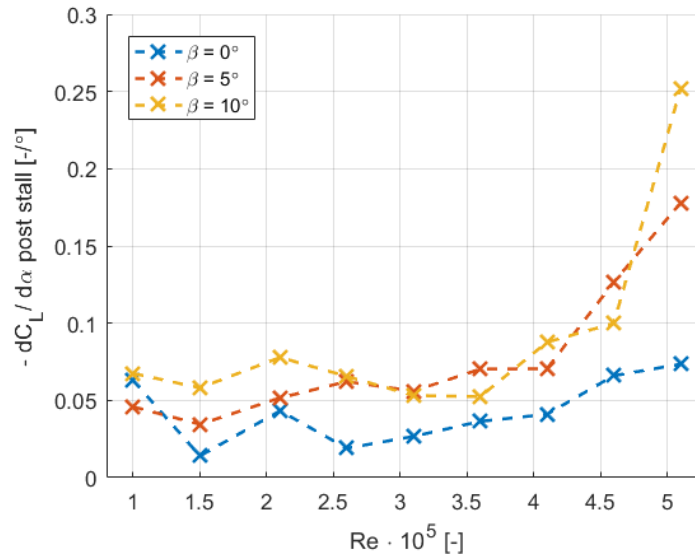


Figure 5.39: Post stall gradient between $C_{L,max}$ and $C_{L,SC}$

The next aspect that has been investigated is the circulation of the stall cell vortices. The results, as a function of the angle of attack and flap angle, are shown in fig. 5.40. The error bars show plus/minus one standard deviation. The circulation is non dimensionalised with the free stream velocity and the flat plate turbulent boundary layer thickness (δ) at a chord of 0.3m. The respective values for the boundary layer thickness are shown in table 5.9. In fig. 5.40 it can be seen that for the initial angle of attack of approximately 14.5° that a increase in flap angle results in stall cell vortices with a higher circulation. However when increasing the angle of attack further this no longer holds. It appears that the flap angle has no consistent influence on the circulation of the stall cell vortices when observing the mean values. Furthermore it can be seen that increasing the angle of attack also has a random influence on the stall cell circulation. A possible cause for this is that the optimisation algorithm for the stall cell vortex identification fails to properly recognise a stall cell. Leading to false identification of stall cell vortices and thus introducing a random error into the average result of the circulation that overshadows the actual result.

$Re \cdot 10^5$	u_∞	δ
1.0	5 m/s	0.0110 m
2.1	10 m/s	0.0096 m
4.1	20 m/s	0.0084 m

Table 5.9: Flat plate turbulent boundary layer thickness for a chord of 0.3 m

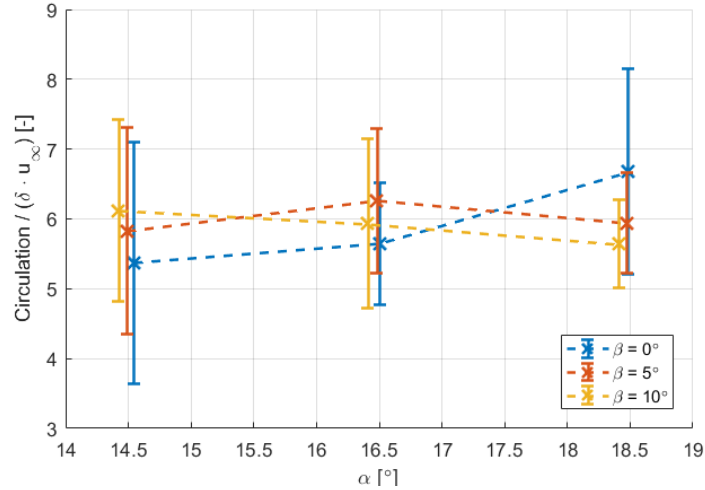


Figure 5.40: Average stall cell vortex strength for varying angle of attack and flap angles; $Re = 2.1 \cdot 10^5$

After the influence of the angle of attack and the flap angle, the influence of the Reynolds number is considered. The stall cell vortex spacing for different flap angles and Reynolds numbers is shown in fig. 5.41. The input angle of attack of 14° has been tested for three different Reynolds numbers, this results in a varying true angle of attack in view of the corrections. The angle of attack varies between 14.27° and 14.78° with an average of 14.51° . This small variation in angle of attack is assumed to have a negligible influence in comparison to the large Reynolds number change. From fig. 5.41 again it can be seen that a larger flap angle results in a wider stall cell vortex spacing, such as described above. This can be seen to be persistent over a range of Reynolds numbers. The influence of the Reynolds number itself is thus consistent over a range of flap angles. An increase in Reynolds number results in stall cell vortices to be closer together. The result of decreasing width of the stall cell implies that increasing the flow momentum does not command a compensating influence of the stall cells. Stall cells can be seen as having a preferred width, which is dominated by the airfoil profile (flap angle). Increasing the flow momentum changes the width of the stall cell, but has a similar influence regardless of the initial preferred width. For the cases under observation here it does appear that the Reynolds number has a universal applicable influence on the stall cell vortex spacing. This universal influence corresponds to a decrease in stall cell vortex spacing of approximately $0.3 x/c$ for the low Reynolds numbers ($1 \cdot 10^5 < Re < 2.1 \cdot 10^5$) and then converge towards a new preferred stall cell vortex spacing that is maintained over the rest of Reynolds number range ($Re > 2.1 \cdot 10^5$). Looking back at the model proposed by Gross et al. (2015), no specific Reynolds number effect is addressed. If the Reynolds number is not included in the prediction, a distinction has to be made between a converged stall cell width or not in terms of Reynolds number influence. The Reynolds number however is also captured by the lift polar. It has been shown that an increase in Reynolds number results in a more negative post stall lift curve gradient. According to Gross et al. (2015) this results in wider stall cells. This is contradicting the results that are shown here. It is thus crucial to take the Reynolds number effect into account when considering the stall cell spacing.

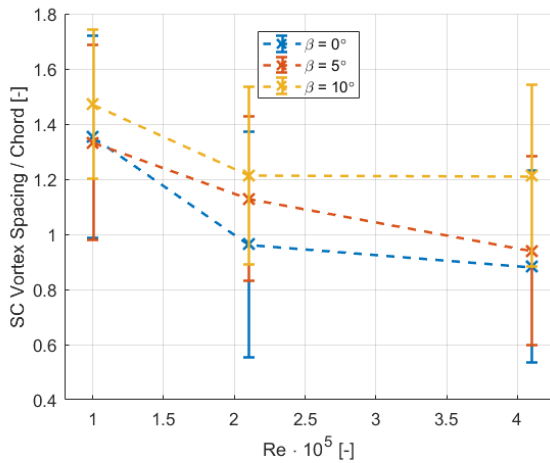


Figure 5.41: Average stall cell vortex spacing for varying Reynolds number and flap angles; $\alpha \approx 14.5^\circ$

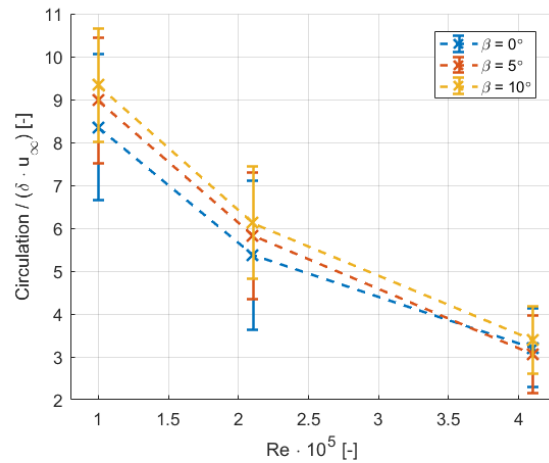
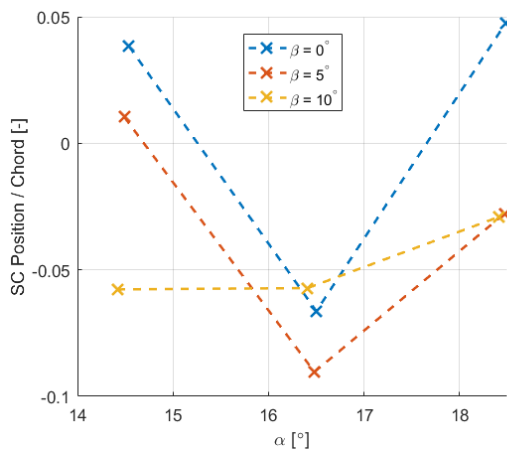


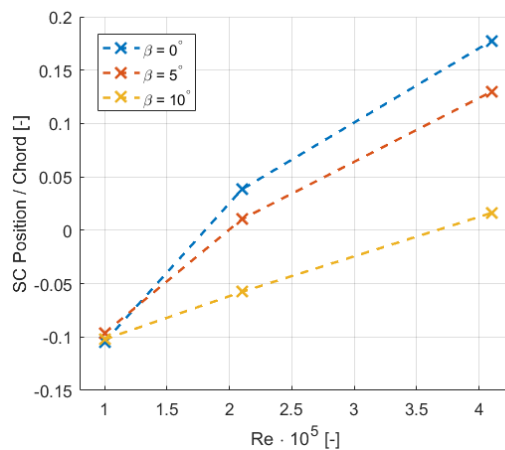
Figure 5.42: Average stall cell vortex strength for varying Reynolds number and flap angles; $\alpha \approx 14.5^\circ$

The Reynolds number effect on the circulation is shown in fig. 5.42. The non dimensional circulation appears to be nearly the same. The difference in value for a specific Reynolds number and varying flap angles is much smaller than the difference caused by a changing Reynolds number. It can be seen that for increasing Reynolds numbers the non dimensional circulation decreases. More specifically it can be observed that the relationship is nearly inversely proportional. Doubling the Reynolds number implies that the normalised velocity potential is approximately halved. More generally this implies that increasing the Reynolds number decreases the influence of the stall cell vortices when they trail downstream.

Lastly the spanwise position of the stall cell is considered, which is determined by taking the average position of both stall cell vortices. In fig. 5.43 the position is shown for varying angle of attack, flap angle and Reynolds number. When considering the angle of attack, no significant trend can be observed for varying angle of attack. Furthermore the flap angle also does not show a convincing influence. The influence of the Reynolds number on the stall cell position is more clear. In fig. 5.43b it can be seen that an increase in Reynolds number mostly pushes the stall cell towards the ceiling, away from the tip with the end plate. However increasing the flap angle results in a stall cell which is positioned closer to the wing tip. This is unexpected as it appears that they have contradicting effects when observing this in terms of lift coefficient.



(a) Influence of the angle of attack, $Re = 2.1 \cdot 10^5$

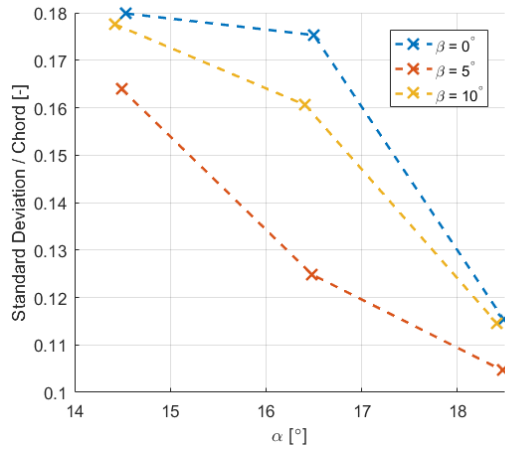


(b) Influence of the Reynolds number, $\alpha \approx 14.5^\circ$

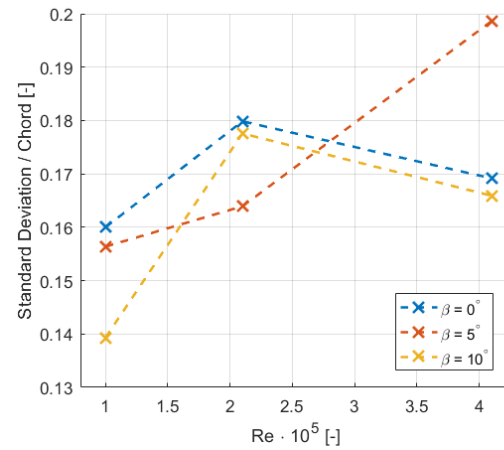
Figure 5.43: Average stall cell position

Another important aspect of the position is the fluctuation. The spanwise fluctuations represent the unsteadiness of the stall cell which has been described as jostling. In the flow phase diagrams for the half wing it was already mentioned that stall cells tend to stabilise after the initial angles of attack where the stall cell appears.

Additionally Manolesos and Voutsinas (2014) mentions how the experiments with both low Reynolds numbers and turbulence intensity result in a low unsteadiness based on Broeren and Bragg, Elimelech et al., Manolesos and Voutsinas (2001, 2012, 2014). The turbulence intensity cannot be controlled but has been investigated and showed some increase with increasing Reynolds number, but already started out with a relatively high turbulence intensity at low Reynolds numbers. In fig. 5.44 the influence of the angle of attack and the Reynolds number on the standard deviation of the position is shown. It can be seen that for an increase in angle of attack, the unsteadiness decreases. The flap angle seems to have no influence. Furthermore it is also shown that an increase in Reynolds number tends to increase the unsteadiness. Both results thus are inline with earlier observations regarding the angle of attack and Reynolds number influence on the unsteadiness.



(a) Influence of the angle of attack, $Re = 2.1 \cdot 10^5$



(b) Influence of the Reynolds number, $\alpha \approx 14.5^\circ$

Figure 5.44: Stall cell position standard deviation

6

Conclusions and Recommendations

6.1. Conclusions

The design of wings for a moderate Reynolds number range between 10^5 and 10^6 often results in the use of airfoil shapes with a moderate to large thickness. These airfoils allow for a large stall angle and thus a wide operational range. Additionally these airfoils have desirable gradual stalling characteristics. The gradual stall behaviour is a consequence of trailing edge stall for which separation of the flow occurs progressively. In previously published literature it has been shown that this Reynolds number range in combination with trailing edge stall leads to the formation of stall cells. Stall cells are localised areas of separated flow, bound by a curved separation line that is terminated by two spiral nodes. The spiral nodes indicate vortices that are inherent to stall cells. Current investigations into stall cells attempt to find the criteria for stall cell formation in terms of angle of attack and Reynolds number. One of the biggest shortcomings of these separate investigations is that they are not compatible for comparison. Different results that have been published can most likely be attributed to different airfoils that have been used. For this reason the effect of the airfoil shapes on the stall cell formation criteria has been investigated in this report.

The changes in airfoil shape are addressed by using a NACA 0012 wing with movable plain flap. The NACA 0012 wing has been compared to published research with a NACA 0015 wing to evaluate the effect of airfoil thickness. The effect of camber has been simulated by changing the flap angle of the wing. In order to investigate stall cell formation, stall cells have to be identified. It has been chosen to use tufts for the identification. Tufts allowed for quick visual identification in both steady and unsteady scenarios, which in turn allowed for a large scale parametric inventory. The angle of attack, Reynolds number and flap angle have been varied to create multiple flow phase diagrams based on the tuft data. Initial experiments on the NACA 0012 wing with AR 5.2 provided strong indications that in assessing stall cell formation criteria two different Reynolds number regimes need to be considered. In the low Reynolds number regime the Reynolds number dominates the requirements for stall cell formation. In the high Reynolds number regime the angle of attack dominates the requirements for stall cell formation. These regimes are dependent on the airfoil shape. The same initial experiments also provided a first estimate of the influence of both the airfoil thickness and camber on the angle of attack and Reynolds number requirements for stall cell formation. This first estimate indicated that thicker airfoils exhibit stall cells at lower angles of attack in the high Reynolds number regime, but at higher Reynolds numbers in the low Reynolds number regime, compared to thin airfoils. The effect of adding camber to the airfoil indicated to promote stall cell formation to lower angles of attack and Reynolds numbers.

The same NACA 0012 wing has been used for a second set of experiments, but with only half the aspect ratio, namely 2.6. These experiments focused on a different hiatus in experimental data regarding stall cells which is the quantitative aspect. Tuft tests such as for the AR 5.2 wing have been repeated with increased angle of attack and Reynolds number resolution. The tuft results were found to be in line with the earlier observations. Force measurements were obtained concurrently with the tuft recordings. This allowed to couple lift coefficient data to flow phases that have been visually registered. The peculiar behaviour which had been observed earlier, where stall cells start to appear at lower angles of attack for higher Reynolds numbers, has been linked to the steep drop in lift coefficient at stall for these Reynolds numbers. A linear model has been constructed based

on the available data from the experiments. The model attempts to predict stall cell formation criteria, but still requires experimental data for the input regarding stall cells. However, the model clearly demonstrates how the lift coefficient plays a considerable role in the formation of stall cells. This illustrates how aerodynamic parameters are potentially more important parameters for stall cell criteria than geometrical parameters such as the angle of attack and the flap angle.

Finally the stall cell vortices have been investigated by means of stereoscopic particle image velocimetry. The area of interest for the stall cell vortex investigation was deemed to be right at the trailing edge, where the vortices trail downstream. Identification of the stall cell vortices in the turbulent wake proved difficult with traditional methods. A vortex identification method based on matching Rankine vortices to the results has been used to determine the positions of the vortices. Additionally the method varies the circulation of the Rankine vortex, thereby capturing the circulation in the largest turbulent scales. The spacing of the vortices has been assumed equivalent to the width of the stall cell. From this assumption the width of the stall cells could be investigated. For increasing flap angles and increasing angle of attack the width of the stall cells was found to increase. The unsteadiness of the width of the stall cells has been shown to be nearly consistent though. The Reynolds number was found to have an opposite effect, for increasing Reynolds numbers the width of the stall cell decreases. The middle of the two stall cell vortices can be regarded as the position of the stall cell. The main interest is the unsteadiness of this position, for which in literature there is still only speculation about which parameters lead to unsteady stall cells. The investigation that has been presented revealed that an increase in angle of attack decreases the unsteadiness of the stall cell position. The Reynolds number on the other hand was found to have an opposite influence, an increase in Reynolds number increases the unsteadiness of the stall cell.

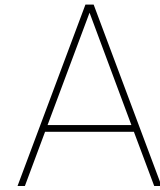
6.2. Recommendations

With the research that has been discussed in this report several question regarding stall cells have been answered. However as can be expected also new questions arise.

One of the discoveries discussed in this report is the distinction between a high and a low Reynolds number regime for stall cells. The high Reynolds number regime has been observed in multiple results, but the low Reynolds number regime was not captured in detail such as done by Dell'Orso and Amitay (2018). Additionally the high Reynolds number regime was also only captured up to a certain Reynolds number, just beyond the point where stall cells appear again at lower angles of attack. From these observations it is clear that investigating a wider Reynolds number range can provide much needed information to help understand stall cell characteristics. In the low Reynolds number regime it would be desirable to gain insight in the influence of the airfoil shape on stall cell requirements. With the presented research it was not possible to judge the influence of the camber. In the high Reynolds number regime it has been shown that there is a relation between the lift coefficient and the stall cell requirements. An investigation at higher Reynolds numbers would be required to confirm the validity of the empirical model over an extensive Reynolds number range. The model based on the lift coefficient mostly serves a practical use to indicate where stall cells start to appear and indicates the importance of aerodynamic parameters in stall cell investigations.

In order to obtain a deeper physical understanding of stall cells it would be beneficial to obtain a pressure distribution on the wing. This is experimentally difficult to obtain traditionally. However with a set of pressure taps the most important information can be obtained by shifting a stall cell over the pressure taps. This can be achieved with a set of fins on the wing and a disturbance to trigger a stable stall cell. Repetition of the stall cell surface pressure mapping for different parameters such as angle of attack, flap angle and Reynolds number can provide information that explains behaviour that has been observed with SPIV in this report.

Finally it is also logical to use different airfoil shapes to conduct similar investigations as have been discussed in this report. The discussion of the results mentioned that thinner airfoils promote stall cells to lower Reynolds numbers, which potentially has a limit value due to loosing the trailing edge stall characteristics. Similarly the negative camber has been mentioned. Investigating different shapes that can also create stall cells can give insight in this specific stall behaviour and can potentially provide information that leads to understanding the creation mechanisms for stall cells.



Conversion Tables

In table A.1 the geometric effects caused by the flap deflection are shown. When the flap deflects the chord shortens and the angle of attack changes. These effects play a role when comparing different airfoils. In the analysis presented in the report the different flap angles are only compared to each other.

flap angle	chord based angle of attack	chord
0°	+0°	0.3000 m
5°	+1.7°	0.2996 m
10°	+3.3°	0.2985 m

Table A.1: Angle of attack based on the LE-TE chord angle of incidence

In fig. A.1 the conversion is shown between the original input values for the angle of attack and the final used value after corrections.

flap	velocity	Original angle of attack																							
		0.0	0.5	5.0	5.5	11.0	11.5	12.0	12.5	13.0	13.5	14.0	14.5	15.0	15.5	16.0	16.5	17.0	17.5	18.0	18.5	19.0	19.5	20.0	20.5
0	5.0	NaN	1.02	NaN	6.03	11.56	12.04	12.55	13.02	13.52	14.01	14.52	15.00	15.51	16.00	16.51	17.00	17.51	18.00	18.51	19.00	19.51	20.00	20.51	21.01
0	7.5	NaN	1.02	NaN	6.05	11.60	12.10	12.60	13.04	13.55	14.02	14.53	15.00	15.51	16.00	16.50	16.99	17.49	17.99	18.49	18.98	19.49	19.99	20.49	20.99
0	10.0	NaN	1.03	NaN	6.08	11.67	12.17	12.68	13.16	13.61	14.03	14.54	15.01	15.51	16.00	16.50	16.99	17.47	17.98	18.48	18.97	19.47	19.97	20.47	20.97
0	12.5	NaN	1.05	NaN	6.14	11.76	12.27	12.77	13.28	13.66	14.12	14.59	15.06	15.55	16.01	16.51	17.00	17.48	17.97	18.46	18.95	19.46	19.96	20.45	20.95
0	15.0	NaN	1.06	NaN	6.21	11.88	12.39	12.90	13.41	13.91	14.17	14.64	15.09	15.55	16.04	16.52	17.01	17.50	17.98	18.45	18.94	19.44	19.93	20.43	20.94
0	17.5	NaN	1.09	NaN	6.29	12.02	12.54	13.05	13.56	14.06	14.20	14.70	15.10	15.60	16.04	16.54	17.02	17.52	18.00	18.49	18.95	19.44	19.93	20.43	20.92
0	20.0	0.58	1.12	5.86	6.39	12.20	12.71	13.25	13.74	14.26	14.25	14.78	15.15	15.64	16.07	16.58	17.03	17.56	18.03	18.50	18.93	19.46	19.91	20.42	20.91
0	22.5	0.62	1.15	5.98	6.50	12.41	12.91	13.46	13.95	14.48	14.35	14.83	15.18	15.65	16.09	16.61	17.05	17.57	18.02	18.50	18.92	19.44	19.90	20.41	20.89
0	25.0	0.67	1.20	6.11	6.63	12.53	13.03	13.53	14.03	14.53	14.46	14.85	15.25	15.73	16.11	16.61	17.06	17.56	18.01	18.50	18.89	19.43	19.87	20.39	20.84
5	5.0	0.51	1.01	5.53	6.03	11.54	12.03	12.52	13.01	13.51	14.00	14.50	14.99	15.50	15.99	16.50	16.99	17.50	17.99	18.50	19.00	19.51	20.00	20.51	21.00
5	7.5	0.51	0.99	5.55	6.03	11.59	12.07	12.55	13.03	13.52	13.99	14.50	14.98	15.49	15.97	16.49	16.97	17.48	17.97	18.49	18.97	19.49	19.97	20.49	20.97
5	10.0	0.50	0.98	5.57	6.05	11.66	12.13	12.63	13.07	13.52	13.98	14.49	14.97	15.49	15.96	16.48	16.94	17.47	17.94	18.47	18.94	19.47	19.94	20.47	20.93
5	12.5	0.49	0.99	5.61	6.10	11.75	12.23	12.75	13.15	13.57	14.00	14.51	14.96	15.49	15.97	16.48	16.94	17.45	17.92	18.44	18.92	19.44	19.91	20.43	20.91
5	15.0	0.49	0.97	5.65	6.14	11.85	12.33	12.87	13.26	13.61	14.05	14.53	14.95	15.48	15.95	16.47	16.93	17.45	17.89	18.40	18.86	19.41	19.87	20.41	20.87
5	17.5	0.47	0.96	5.70	6.19	11.97	12.44	13.00	13.35	13.63	14.03	14.52	14.92	15.46	15.92	16.46	16.91	17.41	17.84	18.38	18.82	19.36	19.82	20.36	20.82
5	20.0	0.45	0.94	5.74	6.24	12.10	12.58	13.14	13.57	13.65	14.05	14.55	14.92	15.46	15.90	16.44	16.87	17.41	17.81	18.34	18.76	19.31	19.76	20.31	20.77
5	22.5	0.41	0.92	5.79	6.30	12.24	12.73	13.30	13.74	14.26	14.09	14.61	14.90	15.43	15.86	16.41	16.80	17.36	17.75	18.29	18.70	19.25	19.70	20.24	20.69
5	25.0	0.38	0.91	5.84	6.38	12.41	12.90	13.47	13.92	14.46	14.06	14.64	14.89	15.42	15.84	16.37	16.79	17.29	17.68	18.20	18.63	19.16	19.61	20.16	20.61
10	5.0	0.50	1.00	5.52	6.02	11.52	12.02	12.50	13.01	13.49	14.00	14.49	14.99	15.49	15.99	16.49	16.99	17.49	18.00	18.49	19.00	19.49	20.00	20.49	21.00
10	7.5	0.47	0.99	5.51	6.03	11.53	12.04	12.50	12.99	13.47	13.98	14.46	14.97	15.46	15.97	16.45	16.96	17.45	17.97	18.45	18.97	19.45	19.97	20.45	20.97
10	10.0	0.44	0.97	5.51	6.05	11.60	12.10	12.49	12.99	13.43	13.96	14.42	14.94	15.41	15.94	16.41	16.94	17.41	17.94	18.41	18.94	19.40	19.93	20.40	20.93
10	12.5	0.40	0.95	5.52	6.07	11.66	12.19	12.51	12.99	13.40	13.92	14.39	14.92	15.37	15.91	16.36	16.90	17.35	17.89	18.35	18.89	19.36	19.89	20.34	20.89
10	15.0	0.36	0.92	5.53	6.10	11.73	12.29	12.55	12.99	13.40	13.93	14.35	14.90	15.32	15.87	16.32	16.84	17.29	17.84	18.28	18.83	19.28	19.84	20.27	20.82
10	17.5	NaN	0.89	NaN	6.13	11.82	12.38	12.57	13.03	13.37	13.91	14.30	14.85	15.28	15.82	16.23	16.80	17.20	17.77	18.21	18.76	19.20	19.76	20.19	20.74
10	20.0	0.24	0.84	5.55	6.16	11.91	12.49	12.94	13.01	13.35	13.87	14.27	14.79	15.22	15.77	16.17	16.72	17.13	17.69	18.11	18.69	19.10	19.67	20.10	20.67
10	22.5	0.17	0.78	5.56	6.18	12.02	12.61	13.05	13.01	13.35	13.87	14.18	14.72	15.15	15.72	16.11	16.63	17.05	17.59	18.00	18.58	19.01	19.57	19.99	20.57
10	25.0	0.09	0.72	5.57	6.22	12.14	12.74	13.19	13.74	13.28	13.78	14.12	14.65	15.06	15.62	16.02	16.54	16.92	17.49	17.88	18.46	18.89	19.46	19.88	20.47

Figure A.1: Original to corrected angle of attack conversion table

B

Surface Oil Flow Visualisation

After the experiments that have been discussed in chapter 5 also a short SOFV experiment has been performed. The oil that was used had a low viscosity and additionally the wind tunnel speed was limited due to the wing setup. These factors combined with the vertical wing setup has lead to poor results that are of little to no use for the stall cell analysis.

Manolesos and Voutsinas (2014) and Ragni and Ferreira (2016) both also used a vertical wing setup. The results from Ragni and Ferreira (2016) show well defined stall cell with still a visible influence of gravity. These tests have been performed at a velocity of 60 m/s, this is much faster than what was possible for the SOFV performed on the NACA 0012 wing. Manolesos and Voutsinas (2014) however also used a velocity which corresponds to approximately 20 m/s based on the reported Reynolds number and chord. It is thus reasoned that similar results should be obtainable. The result such as presented by Manolesos and Voutsinas (2014) is shown in fig. B.1.

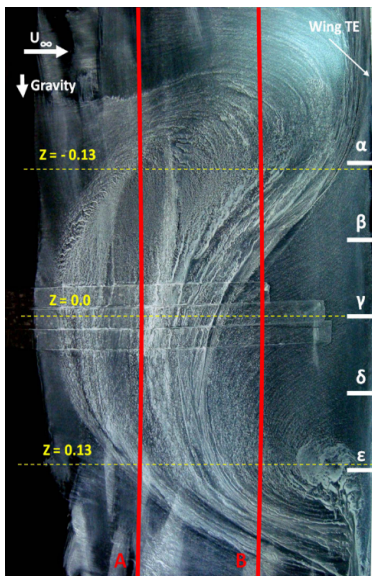


Figure B.1: Stall cell SOFV results by Manolesos and Voutsinas (2014) [27]

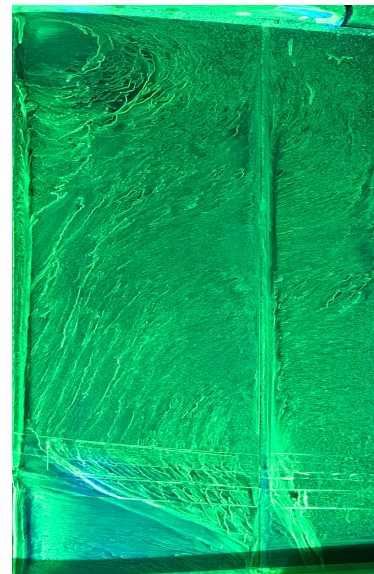


Figure B.2: NACA 0012 SOFV result for $\alpha = 14.78^\circ$, $\beta = 0^\circ$ and $Re = 4.1 \cdot 10^5$

In fig. B.2 a result is shown from the SOFV experiment with the NACA 0012 wing. Both results shown in fig. B.1 and fig. B.2 are obtained at a velocity of 20 m/s. Still a substantial difference in the quality of the results can be observed. This is most likely due to the low viscosity of the oil that has been used. Therefore the gravity has too much of an influence. It can be seen that such as fig. B.2 do not provide convincing information regarding the stall cell. Whereas the tufts and SPIV have been shown to provide useful information for further analysis. It has been chosen to exclude the SOFV results from the analysis in this report. For future work it is recommended to investigate possibilities for more viscous oils that can be applied to the wing for SOFV.

Bibliography

- [1] J. B. Barlow, W. H. Rae, and A. Pope. *Low-Speed Wind Tunnel Testing*. John Wiley & Sons, third edition, 1999. ISBN 978-0-471-55774-6.
- [2] Jan Bartl, Kristian F. Sagmo, Tania Bracchi, and Lars Sætran. Performance of the NREL S826 airfoil at low to moderate Reynolds numbers - A reference experiment for CFD models. *European Journal of Mechanics / B Fluids*, 2018. URL <https://doi.org/10.1016/j.euromechflu.2018.10.002>.
- [3] S. Bell. Measurement good practice guide no. 11. *National Physics Laboratory*, 2001. ISSN 1368-6550. URL https://www.npl.co.uk/special-pages/guides/gpg11_uncertainty.
- [4] F. Bertagnolio, N. N. Sørensen, and F. Rasmussen. New Insight Into the Flow Around a Wind Turbine Airfoil Section. *Journal of Solar Energy Engineering*, 127 (2):214–222, 2005.
- [5] Andy P. Broeren and Michael B. Bragg. Spanwise variation in the unsteady stalling flowfields of two-dimensional airfoil models. *AIAA Journal*, 39 (9):1641–1651, 2001. ISSN 0001-1452. doi: 10.2514/3.14912.
- [6] H. H. Bruun. *Hot-wire Anemometry: Principles and Signal Analysis*. Oxford University Press, 1995. ISBN 978-0-198-56342-6.
- [7] S.C. Crow. Stability theory for a pair of trailing vortices. *AIAA Journal*, 8 (12):2172–2179, 1970.
- [8] Haley Dell’Orso and Michael Amitay. Parametric Investigation of Stall Cell Formation on a NACA 0015 Airfoil. *AIAA Journal*, 56 (8):3216–3228, 2018.
- [9] Haley Dell’Orso, Burak A. Tuna, and Michael Amitay. Measurement of Three-Dimensional Stall Cells on a Two-Dimensional NACA0015 Airfoil. *AIAA Journal*, 54 (12):3872–3883, 2016. ISSN 0001-1452. doi: 10.2514/1.J054848.
- [10] Y. Elimelech, R. Arieli, and G. Iosilevskii. The three-dimensional transition stages over the NACA-0009 airfoil at Reynolds numbers of several ten thousand. *Physics of Fluids*, 24 (2), 2012. ISSN 10706631. doi: 10.1063/1.3682377.
- [11] Ata Esfahani, Nathan Webb, and Mo Samimy. Stall cell formation over a post-stall airfoil: effects of active perturbations using plasma actuators. *Experiments in Fluids*, 59 (9):132, 2018. ISSN 07234864. doi: 10.1007/s00348-018-2588-y.
- [12] G. A. Flynn, J. F. Morrison, and D. G. Mabey. Buffet Alleviation on Swept and Unswept Wings at High Incidence. *Journal of Aircraft*, 38 (2):368–378, 2001.
- [13] A. Gopalarathnam, B.A. Broughton, B.D. McGranahan, and M.S. Selig. Design of Low Reynolds Number Airfoils with Trips. *Journal of Aircraft*, 40 (4):768–775, 2003.
- [14] N. Gregory and C.L. O’Reilly. Low-Speed Aerodynamic Characteristics of NACA 0012 Aerofoil Section, including the Effects of Upper-Surface Roughness Simulating Hoar Frost. *Aeronautical Research Council: Reports and Memoranda*, (3726), 1970.
- [15] N. Gregory, V.G. Quincey, C.L. O’Reilly, and D.J. Hall. Progress Report on Observations of Three-Dimensional Flow Patterns obtained during Stall Development on Aerofoils, and on the Problem of Measuring Two-Dimensional Characteristics. *Aeronautical Research Council: Current Papers*, (1146), 1971.
- [16] A. Gross and H.F. Fasel. High-Order WENO schemes based on the Roe approximate Riemann solver. *AIAA Fluid Dynamics Conference and Exhibit*, 32, 2002.
- [17] A. Gross and H.F. Fasel. High-Order-Accurate Numerical Method for Complex Flows. *AIAA Journal*, 46 (1):204–214, 2008.

- [18] A. Gross, H. F. Fasel, and M. Gaster. Criterion for Spanwise Spacing of Stall Cells. *AIAA Journal*, 53 (1): 272–275, 2015.
- [19] Andreas Gross and Hermann F. Fasel. Numerical Investigation of Passive Separation Control for an Airfoil at Low-Reynolds-Number Conditions. *AIAA Journal*, 51 (7):1553–1565, 2013. ISSN 0001-1452. doi: 10.2514/1.J051553.
- [20] E.L. Houghton, P.W. Carpenter, Steven H. Collicott, and Daniel T. Valentine. Synthesis of subsonic airplane design. *Butterworth-Heinemann*, page 501, 2013.
- [21] Dmitry S. Kamenetskiy, John E. Bussoletti, Craig L. Hilmes, Venkat Venkatakrisnan, Laurence B. Wigton, and Forrester T. Johnson. Numerical Evidence of Multiple Solutions for the Reynolds-Averaged Navier–Stokes Equations. *AIAA Journal*, 52 (8):1686–1698, 2014. ISSN 0001-1452. doi: 10.2514/1.J052676.
- [22] Kurt Kaufmann, Christoph B. Merz, and Anthony D. Gardner. Dynamic Stall Simulations on a Pitching Finite Wing. *Journal of Aircraft*, 54 (4):1303–1316, 2017.
- [23] X. Li, K. Yang, and J. Bai. Experimental study of Reynolds number effects on performance of thick airfoils. *Journal of Renewable Sustainable Energy*, 9 (6), 2017.
- [24] Dajun Liu and Takafumi Nishino. Numerical analysis on the oscillation of stall cells over a NACA 0012 aerofoil. *Computers and Fluids*, 175:246–259, 2018. ISSN 00457930. doi: 10.1016/j.compfluid.2018.08.016.
- [25] Luca Manni, Takafumi Nishino, and Pierre Luc Delafin. Numerical study of airfoil stall cells using a very wide computational domain. *Computers and Fluids*, 140:260–269, 2016. ISSN 00457930. doi: 10.1016/j.compfluid.2016.09.023.
- [26] Marinos Manolesos and Spyros G. Voutsinas. Geometrical characterization of stall cells on rectangular wings. *Wind Energy*, 17 (9):1301–1314, 2014.
- [27] Marinos Manolesos and Spyros G. Voutsinas. Study of a stall cell using stereo particle image velocimetry. *Physics of Fluids*, 26 (4), 2014. ISSN 10897666. doi: 10.1063/1.4869726.
- [28] Marinos Manolesos, G. Papadakis, and Spyros G. Voutsinas. An experimental and numerical investigation on the formation of stall-cells on airfoils. *Journal of Physics: Conference Series*, 555 (1), 2014. ISSN 17426596. doi: 10.1088/1742-6596/555/1/012068.
- [29] Marinos Manolesos, G. Papadakis, and Spyros G. Voutsinas. Experimental and computational analysis of stall cells on rectangular wings. *Wind Energy*, 17 (6):939–955, 2014.
- [30] G.B. McCullough and D.E. Gault. Examples of three representative types of airfoil-section stall at low speed. *NACA Technical Note*, (2502), 1951.
- [31] F.R. Menter. Two-equation eddy-viscosity turbulence models for engineering applications. *AIAA Journal*, 32 (8), 1994.
- [32] G.F. Moss and P.M. Murdin. Two-Dimensional Low-Speed Tunnel Tests on the NACA 0012 Section Including Measurements Made During Pitching Oscillations at the Stall. *Aeronautical Research Council: Current Papers*, (1145), 1968.
- [33] K. Pettersson and A. Rizzi. Aerodynamic scaling to free flight conditions: past and present. *Progress in Aerospace Sciences*, 44 (4):295–313, 2008.
- [34] A.K. Prasad. Stereoscopic particle image velocimetry. *Experiments in Fluids*, 29 (2):103–116, 2000.
- [35] E.R. Prytz, Ø. Huuse, B. Müller, J. Bartl, and L.R. Sætran. Numerical simulation of flow around the NREL S826 airfoil at moderate Reynolds number using delayed detached Eddy simulation (DDES). *AIP Conference Proceedings*, 1863, 2017.
- [36] Daniele Ragni and Carlos Ferreira. Effect of 3D stall-cells on the pressure distribution of a laminar NACA64-418 wing. *Experiments in Fluids*, 57 (8):127, 2016. ISSN 07234864. doi: 10.1007/s00348-016-2215-8.

- [37] Daniel Rodríguez and Vassilis Theofilis. Structural changes of laminar separation bubbles induced by global linear instability. *Journal of Fluid Mechanics*, 655:280–305, 2010. ISSN 00221120. doi: 10.1017/S0022112010000856.
- [38] Daniel Rodríguez and Vassilis Theofilis. On the birth of stall cells on airfoils. *Theoretical and Computational Fluid Dynamics*, 25 (1-4):105–117, 2011.
- [39] Hamid Sarlak, Ariane Frère, Robert Mikkelsen, and Jens N. Sørensen. Experimental investigation of static stall hysteresis and 3-Dimensional flow structures for an nrel S826 wing section of finite span. *Energies*, 11 (6):1418, 2018. ISSN 19961073. doi: 10.3390/en11061418.
- [40] G. Schewe. Reynolds-number effects in flow around more-or-less bluff bodies. *Journal of Wind Engineering and Industrial Aerodynamics*, 89 (14-15):1267–1289, 2001.
- [41] C.E. Simpson, H. Babinsky, J.K. Harvey, and S. Corkey. Detecting vortices within unsteady flows when using single-shot PIV. *Experiments in Fluids*, 59 (125), 2018.
- [42] P. Spalart and S. Allmaras. A one-equation turbulence model for aerodynamic flows. *Aerospace Sciences Meeting and Exhibit*, 30, 1992.
- [43] E. Torenbeek. Synthesis of subsonic airplane design. *Delft University Press*, page 230, 1982.
- [44] D. Weihs and Joseph Katz. Cellular patterns in poststall flow over unswept wings. *AIAA Journal*, 21 (12): 1757–1759, 1983. ISSN 0001-1452. doi: 10.2514/3.8321.
- [45] Allen E. Winkelman and Jewell B. Barlow. Flowfield Model for a Rectangular Planform Wing beyond Stall. *AIAA Journal*, 18 (8):1006–1008, 1980.
- [46] S. A. Yon and J. Katz. Study of the Unsteady Flow Features on a Stalled Wing. *AIAA Journal*, 36 (3): 305–312, 1998.
- [47] T. Zarutskaya and R. Arieli. On Vortical Flow Structures at Wing Stall and Beyond. *AIAA Fluid Dynamics Conference and Exhibit*, 35, 2005.